

Spectroscopy-aided prompt gamma-ray imaging for real-time range verification in proton therapy

Mei Xiao

Doctor of Philosophy

University of York
Physics

December 2020

Abstract

In vivo range verification is desirable to understand the range uncertainties, minimising beam delivery errors during proton therapy. This thesis discusses the development and in-beam tests of a novel prompt gamma-ray imaging prototype system that combines multiple detectors for the absolute and relative range verification of proton therapy, which can be used in clinical tests. The detection system consists of different types of scintillator detectors. First, a high-resolution CLLB ($\text{Cs}_2\text{LiLaBr}_6:\text{Ce}$) detector was used to study the prompt gamma-ray spectroscopy from various target materials. A water phantom with a removable calcium hydroxide cell, simulating bone tissue, was employed to evaluate the sensitivity of the detector for the heterogeneity of the target. In the meantime, eight array type of LYSO ($\text{Lu}_{1.8}\text{Y}_2\text{SiO}_5:\text{Ce}$) detectors placed behind the multi-slit collimator was used to obtain the prompt gamma-ray intensity profile. Furthermore, the energy deposition of protons was studied using a microprobe made by scintillating fibre that was inserted into the phantom and the timing of protons was studied using a time-of-flight relative to a plastic start counter. The combined measurements from both LYSO and fibre detectors are used for the determination of the relationship between 'Bragg peak' and prompt gamma peak.

Results from in-beam measurements at University of Birmingham (Birmingham, UK) and the KVI-CART facility (Groningen, the Netherlands) are presented. It is found that the CLLB detector is sensitive to evaluate the emission of prominent gamma rays from different target compositions and a new method for distinguishing between different tissues is proposed based on ratios of course regions in the energy spectra. The absolute prompt gamma ranges retrieved by the LYSO detectors show acceptable uncertainties for the 66.5 and 150 MeV proton beam. The results are in good agreement with the energy deposition of incident protons measured in the fibre probe. The scintillating fibre probe is water-equivalent and has good sensitivity for the range measurements in proton therapy and it also has the potential to be used for relative range verification with the proton timing measurements. The measurements are compared with Geant4 simulations of the setup and overall good agreement is found with the experimental data.

I would like to dedicate this thesis to my loving parents.

Declaration

I hereby declare that except where specific reference is made to the work of others, the contents of this dissertation are original and have not been submitted in whole or in part for consideration for any other degree or qualification in this, or any other university. This dissertation is my own work and contains nothing which is the outcome of work done in collaboration with others, except as specified in the text and Acknowledgements.

Mei Xiao
December 2020

Acknowledgements

First of all, I would like to express my gratitude to my supervisor Dr. Stefanos Paschalis for his kind guidance and support during my 4-year PhD study. He is not only a patient advisor but also a helpful coworker, who is easily approachable and works with. I would like to thank his dedication for correcting this thesis as well.

I also would like to thank Dr. Pankaj Joshi, Dr. Rubena Yusoff, Dr. Jamie Brown and Prof. David Jenkins for their help and guidance in nuclear physics application laboratory. Especially, Rubena helped me to develop one of the charged particle detectors based on scintillator fibre and Jamie dedicated his time to improve the language of this thesis.

My thanks also go to Prof. Dan Watts, Dr. Sebastian Heil, Dr Ian Syndikus, Sonia Escribano Rodriguez and Harry Kiewiet for their assistance in the KVI experiment in the Netherlands. Moreover, thank Dr. Tony Price and Dr. Ben Phoenix offering great help during the experiment at the University of Birmingham.

I thank the machine shop in the department of physics, Jason Flatt, Adam Stroughair, John Emery and Bob Hide for their continuous support in electronics and mechanics when building our detection system. Besides, I appreciate Simon Hart and Matt Pickin who offered me IT service.

Last but not least, I would like to thank my fellow officemates, Antonio, David, Irene, Matt, Chris, Ryan and Faten. for their company and encouragement during my PhD. It is a special journey to work with them and those days we spent together will be memorable.

Table of contents

List of figures	xv
List of tables	xxvii
Nomenclature	xxix
1 Introduction	1
1.1 Proton therapy: Overview	2
1.1.1 Proton therapy and X-ray therapy	2
1.1.2 Spot scanning and IMPT	3
1.1.3 Range uncertainties in proton therapy	3
1.2 Range verification methods: review	5
1.2.1 Positron emission tomography	5
1.2.2 Prompt gamma-ray prototype: Imaging system	7
1.2.3 Prompt gamma-ray prototype: Non-Imaging system	8
1.3 Motivation	10
1.3.1 Challenges	10
1.3.2 Aim and objectives	11
2 Theory	13
2.1 Particle interaction with matter	13
2.1.1 Charged-particle interactions in matter	14
2.1.2 Uncharged-particle interactions in matter	20
2.2 Absorbed dose and relative biological effectiveness	22
2.3 Gamma-ray detection with scintillator detectors	24
2.3.1 Scintillating material	24
2.3.2 Photosensors for scintillator detectors	26
2.4 Summary	29

3	The configuration of a new Prompt Gamma-ray Imaging detection system	31
3.1	Experimental setup	31
3.1.1	Targets	32
3.1.2	Single-slit collimated CLLB detection system	33
3.1.3	Multi-slit collimated LYSO detection system	34
3.1.4	Fibre probe and plastic counter	38
3.2	Electronics readout system, data acquisition and pulse processing	40
3.2.1	Analog signal processing	40
3.2.2	Digital signal processing	41
3.2.3	ASICs for multi-channel readout	44
3.3	Characterisation of scintillating detectors	46
3.3.1	Energy resolution of CLLB and LYSO detection systems	46
3.3.2	The coincidence timing resolution between the CLLB and LYSO detector	51
3.3.3	Energy measurements of fibre and plastic counter	53
3.4	Summary	56
4	Monte Carlo Geant4 simulation	59
4.1	Secondaries produced in a proton-irradiated phantom	59
4.1.1	Methods	59
4.1.2	Range and secondary radiation	60
4.1.3	Properties of secondary radiation	63
4.2	The statistics of prompt gamma-rays	66
4.2.1	Statistics of specific gamma lines in the PGS	67
4.2.2	The retrieved PG intensity profile	69
4.2.3	PGS and PGT in various media	69
4.3	Range errors using PG methods	72
4.3.1	PGI	72
4.3.2	PGS	75
4.3.3	PGT	77
4.4	Detector response for PGs	78
4.4.1	CLLB detector response	78
4.4.2	LYSO detector response	79
4.4.3	Fibre probe response	82
4.5	Summary	83

5	In-beam experiment with the Birmingham MC40 cyclotron	87
5.1	Methods	87
5.2	PGS in the CLLB	90
5.3	PGS in the LFS array	95
5.4	Fibre response to proton beams	99
5.5	Summary	103
6	In-beam experiment at the KVI centre	105
6.1	Methods	105
6.2	PGS and PGI in the CLLB	108
6.2.1	PGS in CLLB (1.5 inch) with proton beams at 66.5 MeV	108
6.2.2	PGS in CLLB (1.5 inch) with proton beams at 150 MeV	113
6.2.3	PGI in the CLLB (1 inch) with proton beams at 150 MeV	115
6.3	The PGI in the LYSO arrays	118
6.3.1	The PGI for proton beams at 66.5 MeV	118
6.3.2	PGI for proton beams at 150 MeV	123
6.4	In-beam measurements with the fibre probe	127
6.4.1	Fibre response for proton beam at 66.5 MeV	127
6.4.2	Fibre response for proton beams at 150 MeV	131
6.5	Summary	135
7	Discussion and conclusions	137
	References	143
	Appendix A Data sheet of Scintillating materials	151
	Appendix B Functional description of electronics readout systems	153
B.1	Digital pulse processing in DT5730	153
B.2	System diagram of ASIC evaluation kit	153

List of figures

1.1	Depth-dose profiles for a mono-energetic proton and photon beam [1]. The proton beam deposits increased energy with depth, resulting in a Bragg peak at the end. The photon beam delivers decreased energy with depth and there is a dose buildup region to the entrance.	2
1.2	The total SOBP dose distribution (black line) and the individual BP components (coloured lines) [2].	4
1.3	Active beam scanning technique from IBA accelerator [3]. The beam nozzle includes a pair of quadrupoles, two scanning magnets and a vacuum chamber to ensure the precision of beam delivery during the irradiation.	4
2.1	Schematic view of proton interaction mechanisms (Figure taken from [4]). .	14
2.2	The relative fraction of the fluence in a broad beam of protons remaining as a function of depth z in water [5].	16
2.3	Cross section of 4.44, 6.13, 6.92 and 7.12 MeV gamma-ray emission from proton - ^{16}O nuclear reactions [6].	18
2.4	Bragg peak curves of 160 MeV proton beam in water when the nuclear interaction is considered (solid line) and excluded (dashed line).	19
2.5	The photon interaction mechanisms [7].	21
2.6	Energy band structure of activated crystalline scintillators [7].	24
2.7	Energy levels of an organic molecule with pi-electron structure [7].	25
2.8	The SiPM photon-current as a function of incident power on a log-scale [8].	28
3.1	A photograph of targets used in this project. There are two water phantoms with different volumes and three solid targets made from graphite, PMMA and calcium hydroxide respectively.	32
3.2	Schematic drawing (top view) of a CLLB detector collimated by two lead blocks.	34
3.3	Schematic drawing of a LYSO detector array with 16 crystals.	35

3.4	A photograph of the multi-slit collimator with eight LYSO detector arrays arranged behind its slits, leaving one every five slits without being seen by the detectors.	36
3.5	A schematic drawing (top view) of the LYSO detector arrays that aligned behind the multi-slit tungsten collimator and with a view of the phantom through the collimator's slits.	37
3.6	A schematic drawing of the configuration of the fiber probe.	39
3.7	A Schematic drawing of the plastic counter.	39
3.8	A schematic drawing of the electronics readout chain in radiation measurements [7].	40
3.9	A schematic drawing of the signal processing chain with a digitiser [9]. . .	41
3.10	The pulse shape discrimination of a neutron (blue solid line) and a gamma-ray (red dash line) signal [9].	42
3.11	The functional block diagram of DPP-PSD in DT5730 [9].	43
3.12	The ASICs setup connected with the SiPMs of two small LYSO detectors for coincidence measurements.	45
3.13	A schematic drawing of the ASICs tool kit for radiation detection.	45
3.14	The experimental setup for the energy spectroscopy of two gamma-ray sources (^{137}Cs and ^{152}Eu) detected by the CLLB detector.	46
3.15	The uncalibrated energy spectrum of ^{137}Cs and ^{152}Eu in the CLLB detector. The energy peak at 662 keV was fitted with a Gaussian function.	47
3.16	The fitted linear function of channel energy for the calibration of the CLLB detector.	47
3.17	The calibrated energy spectrum measured by the CLLB detector.	48
3.18	The experimental setup for the energy measurement of a point gamma-ray source (^{22}Na and ^{137}Cs) detected by the LYSO detectors.	49
3.19	The uncalibrated energy spectrum of ^{22}Na and ^{137}Cs measured by the LYSO detector arrays at channel 122 (arbitrary channel).	49
3.20	The calibration curve of energy versus charge for the LYSO detector at Channel 122. The effect of non-linearity is already evident at 1275 KeV. . .	50
3.21	The calibrated energy spectrum of ^{22}Na and ^{137}Cs measured in the LYSO detector arrays at channel 122 (arbitrary channel).	51
3.22	The coincidence timing resolution measurements of the CLLB and LYSO detector.	52

3.23	The energy spectra from LYSO (left) and CLLB (right) detector, recorded in a coincidence timing window of 90 ns for 511 keV photons (i.e. peaks in the graph).	53
3.24	The time difference distribution of the CLLB and LYSO detector (left). The improved distribution after applying an energy cut on the 511 keV peak for both detectors (right).	54
3.25	The experimental setup for the energy response of a fibre probe and plastic counter.	54
3.26	The energy spectra of ^{90}Sr with SiPM dark count (noise) in the fibre probe (top). The real energy histogram corresponding to ^{90}Sr once the background spectrum is subtracted (bottom).	55
3.27	The energy spectra of ^{22}Na with SiPM dark count (noise) in the fibre probe (top). The real energy histogram corresponding to ^{22}Na once the background spectrum is subtracted (bottom). The thresholds for both cases were slightly different.	55
3.28	The energy spectra of ^{22}Na (in black) and ^{90}Sr (in blue) in the plastic counter. 56	56
4.1	The cylindrical phantom implemented in Geant4 simulation to study the effect of secondary radiation.	60
4.2	A GEANT4 simulation of the Bragg curves for different proton beams at various energies ranging from 38 to 200 MeV in a water phantom as calculated by the simulation.	61
4.3	A GEANT4 simulation of the statistics of secondary particles (i.e. neutrons, secondary protons and PGs) along the depth in a water phantom irradiated with a proton beam at 150 MeV (the dash line indicates the BP).	61
4.4	A GEANT4 simulation of the statistics of PGs generated along the depth in a water phantom irradiated with proton beams at various energies ranging from 38 to 200 MeV.	62
4.5	A GEANT4 simulation of the statistics of neutrons generated along the depth in a water phantom irradiated with proton beams at various energies ranging from 38 to 200 MeV.	63
4.6	A GEANT4 simulation of the energy spectra of various secondaries produced in a water phantom irradiated with proton beams at 150 MeV.	64
4.7	A GEANT4 simulation of the angular distribution versus energy for various secondaries (PG on the left, neutron in the centre and secondary protons on the right) produced in a water phantom irradiated with a proton beam energy of 150 MeV.	64

4.8	A GEANT4 simulation of the angular distribution of PGs produced in a water phantom irradiated with a proton beam energy of 150 MeV. There is a slight preference for gamma-ray emission in the forward direction (y-axis is zoomed in).	65
4.9	A GEANT4 simulation of the timing spectra of PGs produced in a water phantom irradiated with proton beams at various proton beam energies ranging from 38 to 200 MeV.	65
4.10	A GEANT4 simulation of the timing spectra of PGs gated for specific energy peaks (i.e. 4.44, 5.24 and 6.13 MeV) produced in a water phantom irradiated with a proton beam energy of 65 MeV.	66
4.11	A GEANT4 simulation of the timing spectra of neutrons produced in a water phantom irradiated with proton beams at various energies ranging from 38 to 200 MeV.	67
4.12	A GEANT4 simulation of the energy spectra of PGs produced in a water phantom irradiated with proton beams at various energies ranging from 38 to 200 MeV.	68
4.13	A GEANT4 simulation of the energy versus depth distribution of PGs produced in a water phantom irradiated with a proton beam at 150 MeV. It is clear that the intensity of the 5.24 MeV gamma-ray spreads at a wide range of depth, while that of the 6.13 MeV peaks at depths near the BP (indicated with the horizontal line).	69
4.14	A GEANT4 simulation of the statistics of PGs gated at specific energy peaks (4.44, 5.24, and 6.13 MeV) versus depth in a water phantom irradiated with proton beams at 150 MeV (the dash line was scaled).	70
4.15	A GEANT4 simulation of the energy spectra of PGs produced in various phantom (water, PMMA and Graphite) irradiated with a proton beam energy of 150 MeV.	71
4.16	A GEANT4 simulation of the timing spectra of PGs produced in water, PMMA and Graphite phantoms when irradiated with a proton beam of 150 MeV incident energy. The starting position of the proton beam is 6 cm upstream the phantom entrance window.	72
4.17	A perfect ‘ring’ detector defined in Geant4 simulation.	73
4.18	A GEANT4 simulation of the PG profiles (i.e. selected gamma-ray energy higher than 1 MeV) recorded in a perfect ‘ring’ surrounded a water phantom. The water phantom was shifted in the beam direction up to 4 mm and the applied incident beam energy was at 150 MeV.	74

4.19	A GEANT4 simulation of the PGS (i.e. selected gamma-ray energy higher than 1 MeV) scored in a perfect ‘ring’ surrounding the water phantom at various positions. The water phantom was shifted in the beam direction up to 4 mm and the applied incident beam energy was 150 MeV.	75
4.20	A GEANT4 simulation of the ratio distribution of PGS detected in a perfect ‘ring’ surrounded a water phantom at various positions. The water phantom was shifted in the beam direction up to 4 mm and the applied incident beams was 150 MeV.	76
4.21	A GEANT4 simulation of the PGT (i.e. selected gamma-ray energy higher than 1 MeV) scored in a perfect ‘ring’ detector surrounding a water phantom placed at various positions (shifts from 0 to 4 mm). The incident proton beam energy was 150 MeV.	77
4.22	The experimental setup defined in Geant4 simulation.	78
4.23	A GEANT4 simulation of the simulated energy spectra of secondary radiation detected in the CLLB with and without a timing cut. The water phantom was irradiated with a proton beam energy of 150 MeV.	79
4.24	A GEANT4 simulation of the timing spectrum of secondary radiation scored in the CLLB, for a proton beam energy of 150 MeV.	80
4.25	A GEANT4 simulation of the spatial distribution of secondaries scored in the LYSO arrays for a proton beam energy of 150 MeV (10^{10} incident protons). The y-axis is just arbitrary unit representing the geometry of the crystal arrays. 81	81
4.26	A GEANT4 simulation of the PG intensity profile in the LYSO arrays along the depth of a water phantom irradiated with a proton beam energy of 150 MeV. 81	81
4.27	A GEANT4 simulation of the energy (left) and timing (right) spectrum scored in the fibre probe inserted at 150 mm in a water phantom that is irradiated with a proton beam energy of 150 MeV. The starting position of the proton beam is 6 cm upstream to the entrance window of the phantom.	82
4.28	A GEANT4 simulation of the comparison of BP and the integrated total energy deposited (scaled) in the fibre probe inserted at various positions in a water phantom that irradiated with a proton beam energy of 150 MeV. The error bar in the Bragg curve is too small to show, as 10^5 protons were used or each position.	83
4.29	A GEANT4 simulation of the timing scored in the fibre probe inserted at various positions in a water phantom irradiated with a 150 MeV proton beam. 84	84

5.1	The schematic drawing (top view) of the experimental setup in Birmingham. The fibre probe can only be used in the water phantom and not the solid PMMA and graphite.	88
5.2	The photography of the experimental setup in Birmingham. The water phantom was placed on the top of the linear stage. Two PG detection systems were placed on the two sides of the phantom and there was a plastic start counter placed on the beam line.	89
5.3	The calibrated energy spectrum from ^{22}Na and ^{24}Na detected in the CLLB (1.5 inch).	90
5.4	The energy spectrum obtained from a water phantom run analysed with (red) and without PSD (blue), as detected in the CLLB (1.5 inch). A total of 7.6×10^{11} protons impinged on the water phantom in this run. The characteristic neutron absorption peak of the dual-mode CLLB scintillator is evident at 3.2 MeV when it is not excluded by the PSD analysis. The energy threshold is not the same as the that stated in Figure. 5.3 due to the increase of the temperate (SiPM noises increase with temperate).	91
5.5	The comparison of energy spectra from a water phantom in experiment and simulation detected in the CLLB (1.5 inch). A total of 10^{10} protons were applied for both cases. The simulation underestimates the production of d.e. and s.e. peaks from the 6.13 MeV gamma line.	91
5.6	The energy spectra from various target media (water, PMMA and graphite) in the CLLB (1.5 inch) placed near the BP position. A total of 7.6×10^{11} protons were applied for each of the three cases.	92
5.7	The energy histogram of PGs from a water phantom detected in the CLLB (1 inch) that coupled with the plastic counter. A coincidence window of 496 ns was applied for the CLLB and the plastic counter. A total of 7.6×10^{10} protons were used at a relatively low beam current 10^8 p/s.	93
5.8	The experimental timing spectrum (left) and that with x -axis zoomed in (right) detected in the CLLB. A coincidence window of 496 ns was used for the CLLB and plastic counter.	94
5.9	The simulated timing spectrum scored in the CLLB.	94
5.10	The retrieved PG distributions along the depth in a water phantom detected in the CLLB with and without coincidence mode (PG intensity profile from coincidence mode was scaled by a factor of 15). The counts shown are selected from 3.2 to 4.5 MeV in the corresponding energy spectrum for each position. The error bar is too small to show.	95

5.11	The calibrated energy spectra from the ^{24}Na radioactive source detected in the LFS arrays. The gamma-rays from the ^{24}Na are expected at energies of 1.37 and 2.75 MeV; the peak structure at 1.73 MeV corresponds to the d.e. peak of 2.75 MeV.	96
5.12	The energy spectra of PGs detected in the LFS arrays. A total of 3×10^{11} protons were applied.	97
5.13	The comparison of experimental (top) and simulated (bottom) energy spectra of secondaries from a water phantom detected in the LFS arrays. A total of 10^{10} protons were applied in both cases.	97
5.14	The simulated spatial spectra of secondaries from a water phantom detected in the LFS pixels. A total of 10^{10} protons were applied in the simulation. . .	98
5.15	The simulated statistics of secondaries scored in the LFS pixels along the depth in the water phantom (energy cut: higher than 1.3 MeV). The corresponding experimental results are not shown since only 4 pixels (totally 128 pixels) were extracted with the digitiser.	98
5.16	The simulated (left) and experimental (right) energy spectra recorded in the fibre probe that was inserted at a depth of around 10.5 mm in the water phantom. A total of 3×10^9 protons were applied in both cases.	99
5.17	The comparison of experimental and simulated curves of the normalised energy deposition at various depth in the water phantom.	100
5.18	The experimental timing spectrum (left) and that with x -axis zoomed in (right) detected in the fibre probe that was inserted at the depth of around 10.5 mm upstream of the water phantom.	101
5.19	The simulated timing spectrum scored in the fibre probe that was inserted at a depth of 10.5 mm upstream of the water phantom.	101
5.20	The comparison of coincidence timing spectra recorded in the fibre probe inserted at various depth in the water phantom.	102
5.21	The simulated timing of protons scored in the fibre at various depths inside the water phantom. A total of 10^5 incident protons were simulated at each depth.	102
6.1	A schematic drawing of the experimental setup at KVI (top view, not to scale). Eight LYSO detectors were placed behind the multi-slit tungsten collimator on the left side of the phantom, and the CLLB detection system was placed on the right side of the phantom. A calcium hydroxide cell was inserted inside the phantom.	106

6.2	A photograph of the experimental setup at KVI (looking upstream). On the left, there is a black box housing the LYSO arrays, ASICs and multi-slit collimator, and on the right, there is the CLLB detector behind the single-slit collimator.	107
6.3	The experimental PG transitions emitted from water and Ca(OH) ₂ when irradiated with 10 ¹¹ protons at 66.5 MeV (upper). The simulated PG transitions emitted from water and Ca(OH) ₂ running with 10 ¹⁰ protons at 66.5 MeV (lower). The CLLB detector was placed near the BP position, corresponding to Confi. 1 and 3 listed in Table. 6.1.	109
6.4	The experimental PGs intensity ratio of two histograms (i.e. water divided by Ca(OH) ₂) presented with coarse energy binning at BP position (Confi. 1 and 3) and entrance part of the phantom (Confi. 2 and 4) when irradiated with 10 ¹¹ (left) and 10 ¹⁰ (right) incident protons at 66.5 MeV.	111
6.5	The PGs intensity ratio of two histograms water/Ca(OH) ₂ near BP position (Confi. 1 and 3) presented with coarse energy binning from experiment and simulation, when irradiated with proton beams at 66.5 MeV.	112
6.6	The simulated PG energy spectra near the BP position of a water-only phantom irradiated with proton beams at 150 MeV, with and without the timing cut (< 3.2 ns) applied (upper). The simulated PG timing spectra near the BP position of a water-only phantom irradiated with proton beams at 66.5 and 150 MeV (lower).	114
6.7	The simulated PGs intensity ratio from two histograms water/Ca(OH) ₂ near BP position of the phantom irradiated with proton beams at 150 MeV, when applied with and without timing cut (< 3.2 ns).	115
6.8	The coincidence timing spectrum of the CLLB (1 inch) and plastic counter, which was recorded only when the two signals from both detectors arrived within the time window of 496 ns (upper). The three energy spectra measured in the CLLB (1 inch) before timing peak cut (blue), after timing peak cut (red, i.e. cut on the individual Gaussian peak in the above timing spectrum) and background of timing peak cut (black) for further background suppression (lower). A total of 3 × 10 ⁹ protons were incident on the water phantom. . .	116
6.9	The sigmoid fitted PG intensity profile detected in the CLLB (1 inch) along the beamline for 21 positions. The statistics were selected for an energy range of 3.2 to 6.2 MeV in the PG energy spectra for each of the position. .	117

6.10	A schematic drawing of the water phantom and LYSO detectors showing the relative position (D) of the phantom with respect to the start of the collimator with an incident proton beam energy of 150 MeV (left) and 66.5 MeV (right). The position D can be adjusted by moving the phantom on the linear stage.	118
6.11	The calibrated energy spectrum for a ^{22}Na and ^{137}Cs sources detected in one of the LYSO pixels (channel 120) (upper). The energy spectrum of PGs from the water phantom detected in the pixel (lower). A total of 3×10^{11} protons were used.	119
6.12	The experimental 2D spatial distribution of PGs detected in the LYSO pixels (i.e. energy cut at 1.3 MeV). A total of 3×10^{11} protons were applied.	120
6.13	The experimental PG intensity profile detected in the LYSO detectors along the depth in a water phantom.	120
6.14	The simulated 2D spatial distribution of PGs detected in the LYSO detectors along the depth in a water phantom with an energy selection of larger than 1.3 MeV). A total of 10^{10} protons were used.	121
6.15	The simulated PG intensity profile scored in the LYSO detectors along the depth in a water phantom.	122
6.16	The comparison of energy spectra measured in one of the LYSO pixels (channel 120) under different proton beam energies. The number of incident protons was around 2×10^{11} for both cases.	123
6.17	The experimental 2D spatial distribution of PGs detected in the LYSO pixels (i.e. energy cut at 1.3 MeV). A total of 2×10^{11} protons were applied in this beam run.	124
6.18	The experimental intensity profile of PGs detected in the LYSO pixels in the first data set (upper). The experimental spatial distribution of secondaries detected in the LYSO pixels in the second data set obtained 1 cm upstream (lower).	124
6.19	The subtraction of the two histograms showing in Fig. 6.18 of PGs detected in the LYSO pixels along the depth of the water phantom.	125
6.20	The simulated 2D spatial distribution of secondaries detected in the LYSO arrays from a water phantom (i.e. energy cut at 1.3 MeV). A total of 10^{10} protons were applied.	125
6.21	The simulated 1D intensity profile of PGs of secondaries detected in the LYSO pixels along the depth in a water phantom.	126

-
- 6.22 The comparison of experimental (scaled) and simulated results of the normalised energy deposition in the fibre probe with proton beams at 66.5 MeV. The error bar in the experimental data set is too small to show. A total of 2×10^9 and 10^5 protons were used in experiment and simulation, respectively, for each position. 127
- 6.23 The coincidence timing spectrum of the fibre and plastic counter, which is recorded only when the two signals from both detectors arrive within the time window of 80 ns. The fibre was placed at a depth of 21 mm inside the water phantom. 128
- 6.24 The comparison of coincidence timing spectra at various depth in the water phantom. The centroid of the timing peak is shifted to the right side with the increase of depth in the water phantom. 129
- 6.25 The comparison of experimental (upper) and simulated (lower) proton timing in the fibre probe with proton beams at 66.5 MeV as a function of depth in the phantom. Both the experiment and the simulation show the same trend but the experimental points suggest a larger time difference compared to the simulation. The experimental timing curve is not as smoothing as the simulated one, since the timing resolution of the two coincidence detectors is less satisfactory. 130
- 6.26 The comparison of experimental (scaled) and simulated results of the normalised energy deposition in the fibre probe for the proton beam at 150 MeV. Good agreement is found in the location of the BP, while the absolute energy deposition comparison is less accurate due to the response of the fibre (threshold and quenching effects) and the lack of a reliable energy calibration. The error bar in the experimental data set is too small to show. A total of 4×10^9 and 10^5 protons were used in experiment and simulation, respectively, for each position. 131
- 6.27 The coincidence timing spectrum between the fibre and plastic counter recorded when signals from both detectors arriving within the time window of 496 ns. 132
- 6.28 The comparison of experimental (upper) and simulated (lower) proton timing in the fibre probe as a function of depth, with proton beams at 150 MeV. The centroid of the time difference distribution is plotted on the y-axis versus the depth in the water phantom on the x-axis. The experimental timing values are negative since they are the coincident timing differences between two detectors, however, the simulated timing values represent the absolute time. 133

B.1	DPP firmware functional description in the normal acquisition mode.	153
B.2	System Diagram - SiPM Readout System.	154
B.3	Functional block diagram of ASIC and channel.	154

List of tables

1.1	Proton-induced reaction channels and the corresponding beta decay isotopes in human tissues [10].	6
1.2	Proton-induced reaction channels and the corresponding Prompt gamma-ray isotopes in human tissues.	8
1.3	The comparison of range verification methods in PT.	10
4.1	The nuclear reactions of interest in water (H ₂ O) and the generated gamma-rays.	67
4.2	The statistics of generated gamma-rays in water for proton beam at various energies.	68
4.3	The interested nuclear reactions and the statistics of the corresponding PGs in various target media.	70
4.4	The simulated PGT and the corresponding statistics from various target media for a proton beams energy of 150 MeV.	71
4.5	The simulated PG range with various lengths of phantom shift. A total of 10 ⁸ protons (number was chosen when the statistical error is small and computing time is acceptable) were applied for each case.	73
4.6	The simulated PG range errors and the corresponding statistics of incident protons for the no phantom shift case.	74
4.7	The PGS ratios for each phantom shift. A total of 10 ⁸ protons were applied for each case.	76
4.8	The PGT with various lengths of phantom shift. A total of 10 ⁸ incident protons were applied for each case.	77
5.1	The nuclear reactions of interest in target media and the yield of generated gamma-rays.	92

6.1	The different configurations of the CLLB detector position and the phantom setup used during the irradiation with the 66.5 MeV proton beam. The estimated range of a 66.5 MeV proton beam in water is around 37 mm (from NIST).	106
6.2	The functionality of the different types of detector configurations that were employed in the KVI experiment.	108
6.3	Nuclear reactions of interests and the corresponding prominent gamma-rays for the different isotopes in the composite phantom.	110
6.4	The mean values of ratio at different energy regions for PG detected near the entrance and BP position of the phantom.	111
6.5	The simulated mean values of ratio for PG detected near the BP of the phantom irradiated with 10^{10} protons for each run at 150 MeV.	113
6.6	The centroid of the timing spectrum at various depths in the water phantom.	129
6.7	The centroid position of the prompt-peak proton timing (150 MeV) at various depths in the water phantom as determined experimentally and by Geant4 simulation. The experimental timing values are negative since they are the coincident timing differences between two detectors, however, the simulated timing values represent the absolute time. Here, we have added an offset (2519 ps) to correct the experimental values to be comparable with the simulated ones.	134
6.8	Comparison of retrieved absolute range via fibre and LYSO detectors in experiment and simulation.	136
A.1	Data sheet of scintillating crystals [11–14].	152

Nomenclature

Greek Symbols

c	speed of light
f	wave frequency
γ	gamma-rays
h	Planck constant $\simeq 6.602 \times 10^{-34}$ J·s
λ	wavelength
μ	attenuation coefficient
π	$\simeq 3.14$

Acronyms / Abbreviations

1D	1-Dimensional
3D	3-Dimensional
ASIC	Application-Specific Integrated Circuit
BP	Bragg Peak
CFD	Constant Fraction Discrimination
CSDA	Continuous Slowing Down Approximation
DPP	Digital Pulse Processing
EM	Electromagnetic
FC	Faraday Cup

FoV	Field-of-View
FPGA	Field-Programmable Gate Array
FWHM	Full Width Half Maximum
IC	Ion Chamber
IMPT	Intensity-Modulated Proton Therapy
MCS	Multiple Columb Scattering
NIM	Nuclear Instrumentation Module
PDE	Photon Detection Efficiency
PET	Positron Emission Tomography
PGI	Prompt Gamma-ray Imaging
PG	Prompt Gamma-ray
PGs	Prompt Gamma-rays
PGS	Prompt Gamma-ray Spectroscopy
PGT	Prompt Gamma-ray Timing
PHA	Pulse Height Analysis
PMT	Photo-multiplier Tube
PSD	Pulse Shape Discrimination
PT	Proton Therapy
QA	Quality Assurance
QDC	Charge-to-Digital Converter
QE	Quantum Efficiency
RBE	Relative Biological Effectiveness
SiPM	Silicon Photo-multiplier
SNR	Signal-to-Noise Ratio

SOBP Spread-Out Bragg Peaks

SPECT Single-photon Emission Computed Tomography

TDC Time-to-Digital Converter

TPS Treatment Planning System

Chapter 1

Introduction

Radiotherapy is one of the major modalities in cancer treatment that delivers penetrating radiations into a conformal target volume. Traditionally, X-rays produced by a linear accelerator that provides precise doses are widely used in treating malignant tumours. In the past decade, with the development of accelerator physics and active beam delivery techniques, some charged particles, such as protons and carbon ions are increasingly applied in radiotherapy. So far, around 100 new proton therapy (PT) centres have been commissioned worldwide with many more under construction or planned. In the UK, two NHS founded PT facilities were constructed in Manchester and London, providing high-quality cancer treatment to the general public. It is believed that more patients will benefit from the advanced ion therapy in the future with further reduction of treatment cost.

In this thesis, I will firstly introduce the advantages of PT over traditional photon therapy and the current novel beam delivery techniques that have been applied in PT. The proton-matter interaction mechanisms lead to a localised ‘Bragg Peak’ (BP) in the target volume, which also creates challenges in the quality control of range uncertainties during the treatment. Some widely studied range verification methods are reviewed, including the detection of beta emitters and prompt gamma-rays (PGs) via current or proposed detectors. Regarding the properties of those generated PGs during the treatment, there is no commercial detector that can monitor the beam range in a real-time fashion. The development of a dedicated and cost-effective detector for this application is highly demanded in clinical practice, and the aim of this thesis project is to present the construction and characterisation of a simple multi-detector prototype system for the real-time range verification in PT.

1.1 Proton therapy: Overview

1.1.1 Proton therapy and X-ray therapy

Proton therapy is one of the advanced radiotherapy modalities that utilise high energy proton beams (typically 75 - 250 MeV) for cancer treatment, corresponding to the tumour depth at around 4.6 - 37.9 cm in human body. The majority of the energy deposition of proton beams is localised in the tumour region (i.e. BP), reducing the side effects to normal tissues. The form of BP relies on the interaction mechanisms between protons and matter. Specifically, the high speed protons lose energy traversing matter and the mean energy loss per distance increases with the slowing down of protons (described in Chapter 2 by the Bethe-Bloch formula 2.2). In contrast, X-ray or photon beams deposit most energy in the entrance part of the beam path and deliver decreasing dose with depth in the human body (see Fig. 1.1). The dose-depth curves in the figure show the advantage of proton therapy over conventional photon therapy schematically. Thus, proton therapy might lead to better patient outcomes than traditional X-ray therapy for some types of cancer (e.g. paediatric cancer).

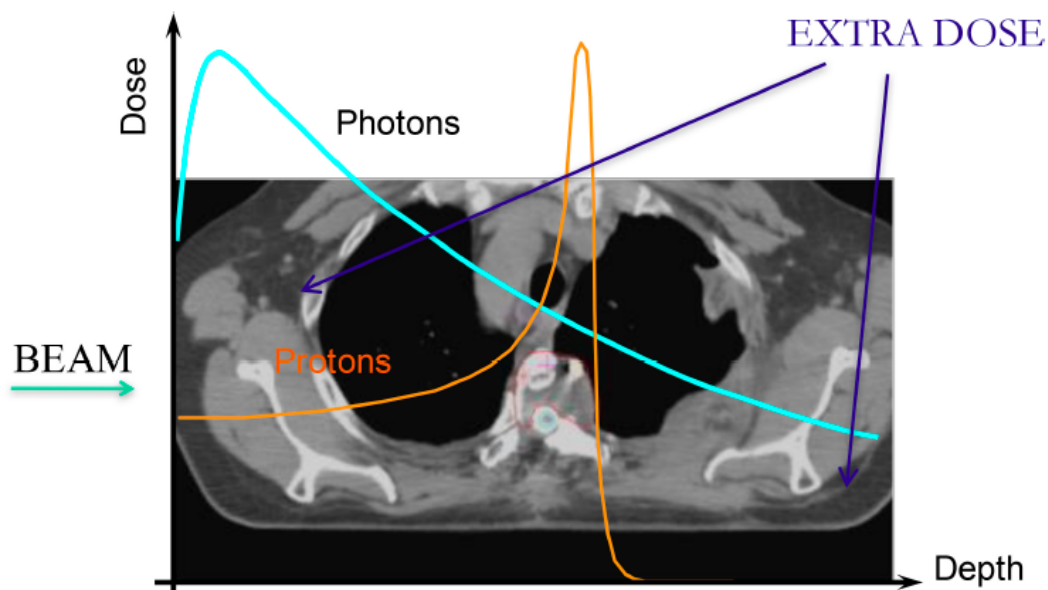


Figure. 1.1 Depth-dose profiles for a mono-energetic proton and photon beam [1]. The proton beam deposits increased energy with depth, resulting in a Bragg peak at the end. The photon beam delivers decreased energy with depth and there is a dose buildup region to the entrance.

The choice of PT or X-ray therapy depends on patient-specific cases. Both the patient benefits and the cost should be considered in clinical practice. Nowadays, the conventional

photon therapy remains the primary radiotherapy modality due to its low cost and availability. To reduce the cost and improve the beam delivery accuracy in PT, the collaboration between physicists, engineers and radiologists is of great importance.

1.1.2 Spot scanning and IMPT

The aim of PT is to ensure that every tissue element in the target volume receives the same dose [5]. The intensity-modulated proton therapy (IMPT) that delivers depth-shifted, arbitrarily complex proton fluency maps from each incident field direction has been realised using the spot-scanning approach [15]. The total prescribed dose is assigned in multi-fractions (i.e. divide the total doses in around 20 to 30 fractions and deliver one fraction per day) based on biological models. For each fraction of the treatment, proton beams are delivered in several courses, leading to a homogeneous dose distribution in the target volume. As displayed in Fig. 1.1, there is a BP in the depth-dose profile of a mono-energetic proton pencil beam, which rises sharply at the end of its penetrating range. In order to obtain a homogeneous dose distribution in the target volume, one must build a superposition of many BPs with the proper intensities and locations. As shown in Fig. 1.2, proton beams with various incident energies are delivered in the same direction leading to multiple BPs (dashed lines) in different locations, which spreads out in depth, known as **spread-out Bragg peaks** (SOBP). The SOBP are delivered through a physical device (i.e. ridge filter or modulation wheel) or by energy section system from the accelerator in conjunction with the variable weighting of each individual BP [16].

The beam delivery using passive scattering (i.e. physical devices) has been gradually replaced by modern active beam scanning technique in recent years. The development of the active beam scanning (also known as ‘pencil’ beam scanning) technique improves the precision and flexibility of beam delivery in PT, realising the real conformal dose distribution in the treatment plans [17, 18] (see Fig. 1.3). Moreover, the active beam scanning technique replaced the heavy collimators in passive beam scanning with four scanning magnets, minimising the secondary radiations in the beam line. The spot-scanning beam intensity and location can be accurately controlled through the energy selection system, which ensures the dose sculpting in any shape of tumour volumes and excellent dose distribution uniformity.

1.1.3 Range uncertainties in proton therapy

As explained in section 1.1.2, the spot scanning technique has been applied via energy selection system in modern accelerators, realising the ‘dose sculpture’ in irregular target

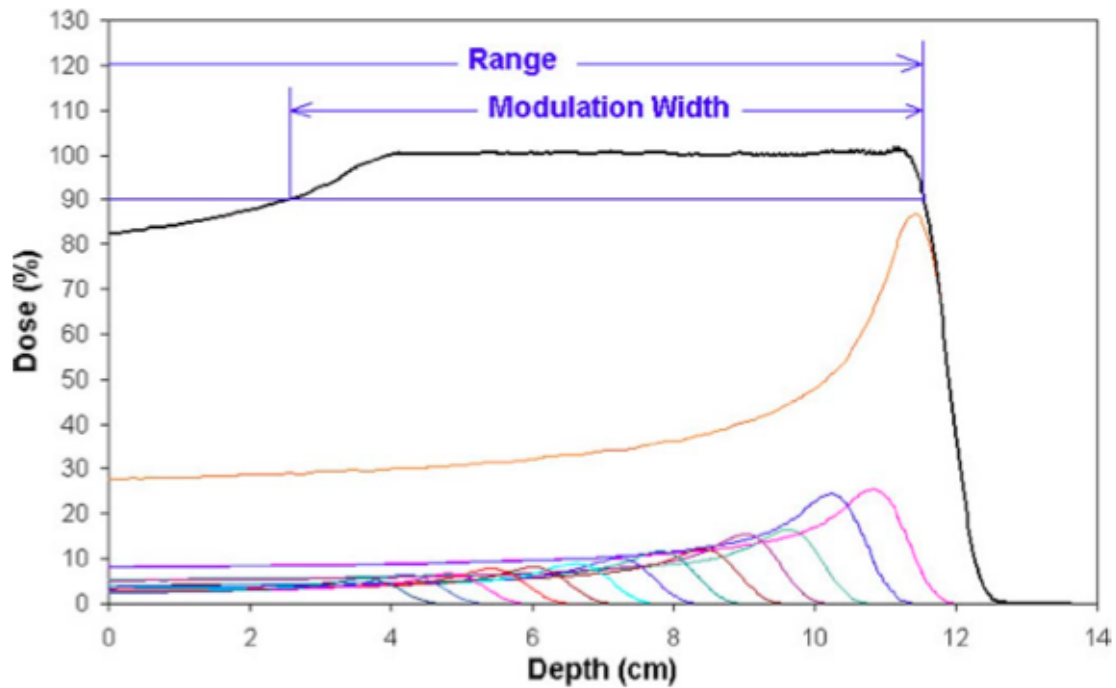


Figure. 1.2 The total SOBP dose distribution (black line) and the individual BP components (coloured lines) [2].

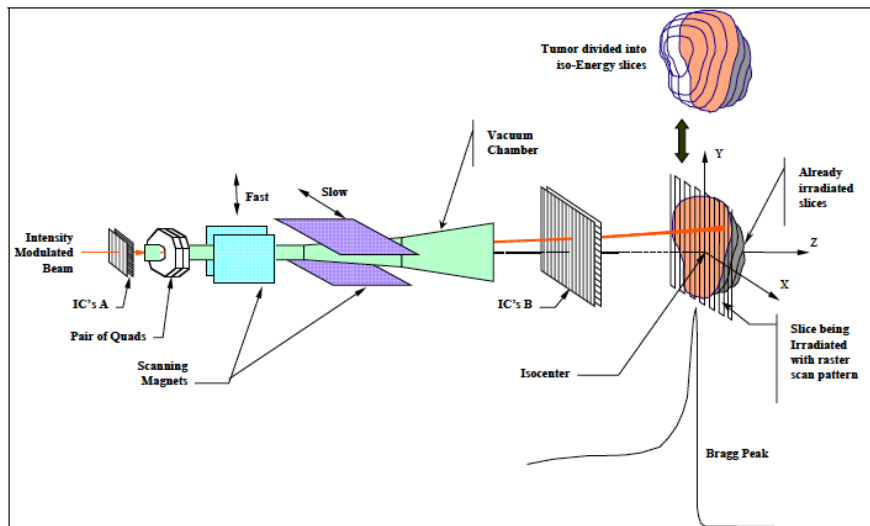


Figure. 1.3 Active beam scanning technique from IBA accelerator [3]. The beam nozzle includes a pair of quadrupoles, two scanning magnets and a vacuum chamber to ensure the precision of beam delivery during the irradiation.

tumours. Thus, any ‘undershoot’ or ‘overshoot’ of the beams causes more damage to the patients due to the localised energy deposition in BP region. In order to fully utilise the advantage of PT, the prediction of range needs to be as accurate as possible during the treatment planning and delivery process, minimising the unnecessary dose to normal tissues. However, in a clinical environment, uncertainties arise from many sources: organ motion, patient setup and anatomical variations, dose calculation approximations and biological considerations [19]. The acceptable range uncertainty in treatment planning at Massachusetts General Hospital (MGH, Boston, US) is 3.5 % of the beam range plus an additional 1 mm [19], while other institutes have different but similar margin standards. In this project, we follow the recipe suggested by MGH.

Hence, it is required to measure the range of the proton beams as a part of the quality assurance (QA) process using an ion chamber (IC) [20], which is a direct method for pre-treatment range verification. However, there are further uncertainties during the treatment (e.g. patient setup and organ motion) that cannot be identified in the QA process. Considering these sources of range uncertainties during the treatment, the real-time monitoring of the beam delivery is of great significance not only for maximising the therapeutic effect but also the safety of the patients. An indirect range verification method was proposed [21] via detecting the secondary emissions from the patients for the online range verification. As the high-energy proton beam slows down in the human body, protons interact with tissues via both electromagnetic (EM) and nuclear interactions, leading to the emission of penetrating secondary radiation along the proton path. Those nuclear-induced secondaries contain the information of the location of distal dose gradient, where the beam stops.

1.2 Range verification methods: review

In the past two decades, many research groups have focused on the study of *in vivo* range verification methods and achieved promising results via the detection of nuclear-induced secondaries during PT. In this section, we review the widely studied methods of range verification, including the detection of beta emitters by position emission tomography (PET) and PGs by other proposed detector prototypes.

1.2.1 Positron emission tomography

The PET/CT scanning system provides a practical approach for the *in vivo* treatment verification in PT, which has been applied clinically in some institutes (e.g. MGH). It measures the 3-Dimensional (3D) imaging of the beta decay activity after proton irradiation. There are

Table 1.1 Proton-induced reaction channels and the corresponding beta decay isotopes in human tissues [10].

Target	Reaction channels	Beta isotopes	Half-life
^{12}C	$^{12}\text{C}(p,p2n)^{10}\text{C}$, $^{12}\text{C}(p,pn)^{11}\text{C}$	^{10}C , ^{11}C	19.29 s, 20.33 m
^{14}N	$^{14}\text{N}(p,2p2n)^{11}\text{C}$, $^{14}\text{N}(p,pn)^{13}\text{N}$, $^{14}\text{N}(p,n)^{14}\text{O}$	^{13}N	9.96 m
^{16}O	$^{16}\text{O}(p,pn)^{15}\text{O}$, $^{16}\text{O}(p,3p3n)^{11}\text{C}$, $^{16}\text{O}(p,2p2n)^{13}\text{N}$, $^{16}\text{O}(p,p2n)^{14}\text{O}$, $^{16}\text{O}(p,3p4n)^{10}\text{C}$	^{14}O , ^{15}O	70.61 s, 122.24 s
^{31}P	$^{31}\text{P}(p,pn)^{30}\text{P}$	^{30}P	2.50 m
^{40}Ca	$^{40}\text{Ca}(p,2pn)^{38}\text{K}$	^{38}K	7.64 m

three operational modalities for PET verification: in-beam PET, which uses the PET detection panels integrated with the beam delivery system; off-line PET, the patient needs to be moved to a nearby PET facility; in-room, which uses a PET scanner installed independently in the same treatment room (i.e. patients can be scanned directly after the beam irradiation on the same couch) [22].

The major nuclear creation channels for proton induced positron emitter productions can be seen in Table. 1.1. The half-life of those isotopes range typically from around 2 mins (^{15}O) to 20 mins (^{11}C). In the case of off-line PET/CT (post-treatment) imaging, the short half-life isotopes are rarely detected due to the time needed for the patients to be transferred to the other scanning room (typically, 10 mins). The most sensitive activity is from ^{11}C with a half-life of around 20 mins, which introduces the biological washout in this modality [23–25]. Apart from the washout challenge, A. Knopf *et al* [26] also mentioned that the *in vivo* PET measurements are challenged due to patient motion, image co-registration uncertainties and variations of tissue compositions (heterogeneous tissues).

To reduce the washout effect, in-room PET imaging has been trialed to reduce PET scan times [27, 28]. Firstly, the short half-life isotope ^{15}O can be detected so that a short-length PET scan of 5 minutes can yield similar results to a 20 minute scan performed offline. In the meantime, patients do not need to be re-positioned, which reduces the setup uncertainties.

Real-time monitoring requires the in-beam PET method that was studied by many research groups [29–33] with a dedicated PET camera. The major technical challenge of in-beam monitoring lies on the geometric constraints in a treatment environment, which makes it difficult to integrate a full-ring PET scanner in the beam delivery system. Moreover, the dedicated PET scanner studied were dual-head configuration that limits the Field-of-View (FoV) in image reconstruction. Finally, the cost of such a dedicated PET scanner is high, restricting its application in hospital-based PT facilities.

Overall, treatment verification using PET imaging has been studied clinically with patient-specific cases, which shows favourable results in some cases, depending on the tumour sites. As mentioned above in the off-line PET part, the research group at MGH pointed out many challenges ongoing with this method, such as biological washout that cannot be solved easily without in-beam PET scanning. They have not yet worked out the co-registration between beta activity distribution and the treatment planning dose distribution for the post-treatment verification. This requires the improvement of the cross section database for the main reaction channels in Monte Carlo (MC) simulation and precise modeling of washout effects.

1.2.2 Prompt gamma-ray prototype: Imaging system

The other leading method for non-invasive range/dose verification is measuring PGs during PT. As opposed to the PET/CT method which uses commercially produced PET instruments, the PG method requires a bespoke camera for the detection of high-energy gamma-rays (4 - 6 MeV). One of the merits of this method over PET scanning is that it monitors the beam delivery in a real-time fashion. The PG detector is expected to be compact and movable, so that it can be placed in room during inter-fraction treatment for online verification, as the PGs are generated instantly. This method requires the detection of high energy gamma-rays and calls for novel detector systems such as those commonly developed for use in fundamental nuclear physics. The multi-discipline cooperation offers nuclear physicists a great opportunity to be a part of innovative particle therapy research.

The non-elastic nuclear interactions between target nuclei (e.g. ^{16}O , ^{12}C) and protons release high energy gamma-rays at certain energies. The relevant reaction channels have been illustrated in Table. 1.2, including $^{16}\text{O}(p,p' \gamma 6.13 \text{ MeV})^{16}\text{O}^*$, $^{12}\text{C}(p,p' \gamma 4.44 \text{ MeV})^{12}\text{C}^*$ and $^{16}\text{O}(p,x \gamma 4.44 \text{ MeV})^{12}\text{C}^*$. We notice that those reactions occur immediately during the irradiation and continue to be generated along the beam path, yielding most of the PGs near the end of the beam path (i.e. BP region) where there are often the highest cross sections.

Based on the observation above, we can monitor the proton range by examining the 1-Dimensional (1D) PG intensity distribution along the beam depth in a phantom using a mechanical collimation detection system [34–38]. C.H. Min *et al* [21] were first to compare the measured dose-depth profile and PG profile experimentally and suggested there is promising future for the real-time in vivo range verification via PG detection. J. Smeets *et al* [39] improved the collimation by using a knife-edge slit gamma camera for the 1D PG distribution and their device has been tested clinically [40] with a brain cancer patient and showed excellent accuracy in range verification.

Other groups have obtained the 3D PG imaging using a dedicated Compton gamma camera [41–46]. A. Koide *et al* [47] have managed to reconstruct the image from $^{12}\text{C}(p,p' \gamma$

Table 1.2 Proton-induced reaction channels and the corresponding Prompt gamma-ray isotopes in human tissues.

Target	Reaction channel	Gamma-ray energy [MeV]
^{12}C	$^{12}\text{C}(\text{p},\text{x})^{11}\text{C}^*$	2.0
	$^{12}\text{C}(\text{p},\text{p}')^{12}\text{C}^*$	4.44
^{16}O	$^{16}\text{O}(\text{p},\text{p}')^{16}\text{O}^*$	6.13
	$^{16}\text{O}(\text{p},\text{x})^{12}\text{C}^*$	4.44
	$^{16}\text{O}(\text{p},\text{x})^{15}\text{O}^*$	5.24
	$^{16}\text{O}(\text{p},2\text{p})^{15}\text{N}^*$	5.27
^{14}N	$^{14}\text{N}(\text{p},\text{p}')^{14}\text{N}^*$	1.64, 2.13
^{40}Ca	$^{40}\text{Ca}(\text{p},\text{p}')^{40}\text{Ca}^*$	3.73

4.44 MeV) $^{12}\text{C}^*$ with a 70 MeV proton beam at low beam current and an acquisition time of 5 hours.

We introduced two collimated PG detection systems, one with a mechanical collimator and the other contains a multi-stage detector as an electronic collimation for the collection of PGs at a certain angle from Compton scattering. The technique for mechanical collimated PGI is mature and has been tested clinically in terms of the 1D range verification, while there is space to improve the Compton scattering collimation for 3D range/dose verification in clinical environment, such as count rate limitation, image reconstruction and high cost.

1.2.3 Prompt gamma-ray prototype: Non-Imaging system

From section 1.2.1 and 1.2.2, we notice the in-beam PET imaging and PGI are promising to be applied clinically for the 3D dose/range verification or 1D range verification. However, the cost to build such a detector system is high and the image reconstruction in PET and Compton scattering is complicated. A key point of image reconstruction is that we cannot do effective and highly precise online image reconstruction yet, which makes PET and Compton imaging less appealing for the real-time beam monitoring.

In the recent years, radiation detection technology from nuclear and particle physics is studied intensively for the beam delivery safety in ion beam therapy. Some novel scintillator materials, such as LaBr_3 , CeBr_3 and BaF_2 have been studied in PG energy and timing measurements. Those novel scintillators have either fast decay time or excellent energy resolution that can provide the energy and/or timing information of the PGs. On the other hand, solid-state detectors, such as HPGe (high purity Germanium detector), usually applied in nuclear or particle physics for gamma-ray spectroscopy, has also been employed in the PG energy detection.

To reduce the cost and complexity of image reconstruction, some non-imaging systems have been proposed and tested by many groups based on the detection of energy and/or timing of the interested gamma lines for the relative range verification in PT. Those non-imaging methods include prompt gamma-ray timing (PGT), Prompt gamma-ray spectroscopy (PGS) and other methods extending from those two primary methods.

The authors in references [48–50] have studied the range verification in particle therapy based on the PGT measurements. The incident proton time can be recorded as the starting time of the system while the produced PGs are detected in the fast scintillators as the end time. The Full-Width Half Maximum (FWHM) of the PGT spectrum increases with the initial proton energy and the centroid position of the PGT shifts with the proton range in the phantom. These observations can be applied for inter-fraction relative range verification [51]. Furthermore, the PGT peak integration technique provides the information for a cost-effective beam monitoring by removing the collimation system [52]. The beam structure of accelerators restricts this method to be applied widely, as different PT institutes might install different cyclotrons or synchrotrons.

The PGS is independent from the accelerator, which is an indirect method based on the measurements of characteristic gamma lines (i.e. 4.44 MeV, 6.13 MeV) and their relative emission for the range verification. J.C. Polf *et al* [53] have shown the quantitative measurements of prominent gamma lines from $^{12}\text{C}(p,p')^{12}\text{C}^*$ and $^{16}\text{O}(p,p')^{16}\text{O}^*$ at 4.44 MeV and 6.13 MeV allow the quantification of the target composition. J.M. Verburg *et al* [54] have intensively studied the magnitudes of discrete gamma lines and their correlations with the proton energy. Moreover, the quantitative gamma lines from specific nuclear transitions can be directly related to the nuclear reaction cross section, which enables the elemental analysis of the tissue. To enable the PGS, a detector with good energy resolution is essential. HPGe detector is considered as the optimal choice in nuclear physics for gamma-ray spectroscopy for its superior energy resolution. However, this type of detector requires a cooling system that is less practical for hospital based PT facilities. Some novel scintillators mentioned above, such as LaBr_3 or CeBr_3 also have excellent energy resolution (3 - 4% at 662 keV), and have been studied for use in PGS [55]. They also have relatively short decay time (around 25 ns) so that the timing information of PGs can be used to reject the neutron induced noise at high energy range, improving the Signal-to-Noise ratio (SNR) of the PG energy spectrum.

In this section, we reviewed the range verification methods, such as PGT and PGS and compared them to the PET and Compton camera methods. The timing and energy information of PGs can realise the range/dose verification in real-time fashion. Furthermore, the cost can be reduced without building a multi-stage detector or a full-ring PET scanner. On the other hand, PET scanning and Compton camera can provide post-treatment 3D gamma-ray

Table 1.3 The comparison of range verification methods in PT.

Methods	3D imaging	1D range	Relative range	Real time	Additional cost
Off-line PET	Y	Y	Y	N	None
In-room PET	Y	Y	Y	N	high
In-beam PET	Y	Y	Y	Y	high
PGI	N	Y	Y	Y	medium
Compton camera	Y	Y	Y	N ¹	medium
PGS, PGT, PGPI	N	N	Y	Y	low

intensity mapping to compare with calculated dose mapping in treatment planning system (TPS) and avoid the use of heavy collimators.

1.3 Motivation

1.3.1 Challenges

So far, we have introduced the advantages and challenges in PT, the necessity for real-time range verification and reviewed some methods dealing with range monitoring, including the detection of positron annihilated photons or PGs via current or proposed detector prototypes. Even though the range verification using off-line PET was applied clinically, the real-time PET-based monitoring of the proton range is still challenging due to the lack of a dedicated detection system. Moreover, while many research groups have made good progressions in developing an in-beam PET or Compton camera for the 3D dose verification in PT, these remain very costly and require complicated detection systems and image reconstruction algorithms. The simple method via mechanical slit collimation detector has been clinically proved to be effective in head and neck cancer, providing a promising future for online beam monitoring via the detection of PGs produced instantly in the target media. To further reduce the cost, the collimation was removed by other research groups to measure the energy and timing of the PGs only, which has been proved to be effective for the relative range verification in PT.

Overall, the biggest challenge is the lack of a cost-effective detector supporting the online beam monitoring in clinical scenarios. To achieve the range uncertainty (3.5 %, 1 mm) proposed at MGH, the detector is also expected to be highly sensitive under limited incident protons for one beam shot (around 10^9 to 10^{10}). As we have seen there are advantages and drawbacks for each of the monitoring methods (see Table. 1.3) and a commercial product for this application is not available yet. In the next section, we illustrate the aim of this project and propose our designed prototype to tackle this challenge.

1.3.2 Aim and objectives

In this research work, we focus on the detection of PGs rather than delayed photons following positron annihilation, since the biological washout in off-line PET cannot meet the requirement of real-time verification and the cost for an in-beam PET system is far more expensive. At the same time, the PET technique is mature and has been commonly applied in hospital for functional imaging, while the dedicated detection system for PGs is still on the research stage. To develop such a detector, the cost, simplicity and sensitivity should all be considered in a hospital based PT facility.

We have developed, tested and characterised a novel detector prototype consisted of a combination of scintillating detectors, providing a fast detecting method for the real-time range/dose verification in PT. In particular, the scintillator detectors include a monolithic CLLB (i.e. $\text{Cs}_2\text{LiLaBr}_6:\text{Ce}$) crystal, LYSO (i.e. $\text{Lu}_{1.8}\text{Y}_2\text{SiO}_5:\text{Ce}$) arrays and a plastic fibre probe to study the PGS, PG profile (i.e. statistics along depth) and the energy and timing of proton beams. The configuration of those detectors will be introduced in Chapter 3. As discussed in subsections 1.2.2 and 1.2.3, the PGI was proved to be promising for the absolute range measurements, while some novel methods, such as the PGS and PGT were also studied intensively due to their high-efficiency and cost-effectiveness in the relative range verification. Combing those methods realise our final aim: developing a simple, low-cost and sensitive prototype for the real time beam monitoring in hospital based PT facilities, which provides not only absolute and relative range verification but also the energy-depth distribution (i.e. in fibre) for comparison.

Chapter 2

Theory

In this chapter, we introduce the fundamental physics background in PT and radiation detection. First of all, the charged particle interaction mechanisms are presented, including the electromagnetic (EM) and nuclear interactions. The EM interactions govern the continuous energy loss mechanism and are the main contribution to the BP, while the proton-nucleon interactions are responsible for the production of secondary gamma-ray and neutron radiation. The relation between the cross section of nuclear reactions and the dose-depth curve is also discussed to cover the essential physics background that governs in range verification using PGs. The definitions of absorbed dose and relative biological effectiveness (RBE) are also introduced to highlight some basic concepts in radiotherapy. Moreover, the gamma-ray interactions in matter are discussed to cover the most important three types of interactions and the neutron interactions are introduced briefly. Finally, the principles of radiation detection using scintillation detectors are discussed.

2.1 Particle interaction with matter

The energy of therapeutic proton beams can typically reach values of 250 MeV. These high-speed particles interact with matter mainly through the Coulomb-force (i.e. EM) and nuclear interactions. In the meantime, secondary gamma rays and neutrons are produced during the proton irradiation. So, it is essential to cover the radiation interaction mechanisms of not only the primary protons but also the secondaries in PT.

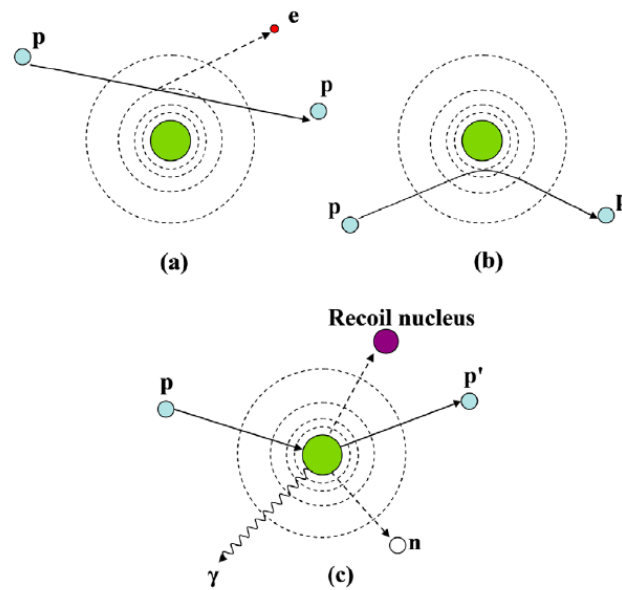


Figure. 2.1 Schematic view of proton interaction mechanisms [4]. (a) Energy loss via inelastic Coulomb interactions with electrons, (b) deflection of proton by Coulomb elastic scattering with the electric field of the nucleus, (c) nuclear reactions and the production of secondary particles.

2.1.1 Charged-particle interactions in matter

EM interaction

EM interactions dominate the energy loss in PT: the incident protons lose kinetic energy continually via exciting and ionising atomic electrons of the medium. As the velocity of protons decreases along the beam path in the medium, the scattering of protons via elastic Coulomb interactions is enhanced. The above stopping and scattering interactions are illustrated in Fig. 2.1 (a) and (b) respectively.

To describe the stopping process, we firstly introduce the definition of **Stopping Power** (S) that is the expectation value of the rate of energy loss (dE) per unit of path length x , (i.e. $\langle dE/dx \rangle$) [56]. It is more convenient to define the energy loss rate with independent mass density, so the **Mass Stopping Power** (S/ρ) is most often used, which is defined as:

$$\frac{S}{\rho} = -\frac{dE}{\rho dx}. \quad (2.1)$$

The expression of the energy loss rate accounting for both the relativistic and quantum mechanical effects is known as the **Bethe-Bloch** formula:

$$-\left\langle \frac{dE}{\rho dx} \right\rangle = 4\pi N_A r_e^2 m_e c^2 \frac{Z}{A} \frac{z^2}{\beta^2} \left[\ln \frac{2m_e c^2 \gamma^2 \beta^2}{I} - \beta^2 - \frac{\delta}{2} - \frac{C}{Z} \right], \quad (2.2)$$

where, N_A is Avogadro's number, r_e is the classical Bohr radius, Z is the atomic number of the target, z is the charge of the projectile, m_e is the mass of an electron, A is the atomic weight of the target material, C is the shell correction item, δ is the density correction, β equals to v/c , v is the particle speed and c is the speed of light and I represents the average excitation energy of material. Eq. 2.2 implies the mass stopping power is approximately proportional to the inverse square of the velocity (i.e. $1/\beta^2$) of the projectile. It also states that the absorbing material strongly influences the energy loss rate which is proportional to the density of electrons in the absorber, as the inelastic Coulomb interactions occur between the protons and atomic electrons.

From the mass stopping power, one can already estimate the range of the charged particles in a medium. The **Range** (R) is defined as the average path length traveled by a charged particle up until it is considered to be at rest. This value can be approximated by the **continuous-slowing-down range** (R_{CSDA}) that is defined as [5]:

$$R_{CSDA} = \int_0^{E_0} -\frac{dE}{dx} \rho dE. \quad (2.3)$$

For practical purposes, the CSDA range can be taken as identical to the actual range R which is slightly higher (by 0.2 % or less for protons) than the calculated R_{CSDA} due to the occurrence of discrete and discontinuous energy loss [56]. To simplify the calculation of Eq. 2.3, there is a more practical method for the estimation of the CSDA range, which is given by the **Bragg-Kleemann** rule:

$$R(E) = \alpha E^p, \quad (2.4)$$

here α is a material-dependent constant, E (in MeV) is the initial energy of the proton beam, and the exponent p depends on the proton energy. By interpolating range-energy tables, we can fit Eq. 2.4 to the range in water at 100 and 200 MeV to find the two constant parameters [5]:

$$R(E) = 0.000244E^{1.75} \quad \text{g/cm}^2. \quad (2.5)$$

These two parameters (α and p) can be slightly different depending on the energy range used for the power-law fit. Another commonly used definition of range is the **Projected Range** that is the expectation value of the furthest depth of penetration of a charged particle in a medium measured along its initial direction [5]. Generally, the path of most protons is nearly straight, so the projected range is nearly equal to the actual path length. More precisely, the projected range is always slightly smaller than the CSDA range. Due to the

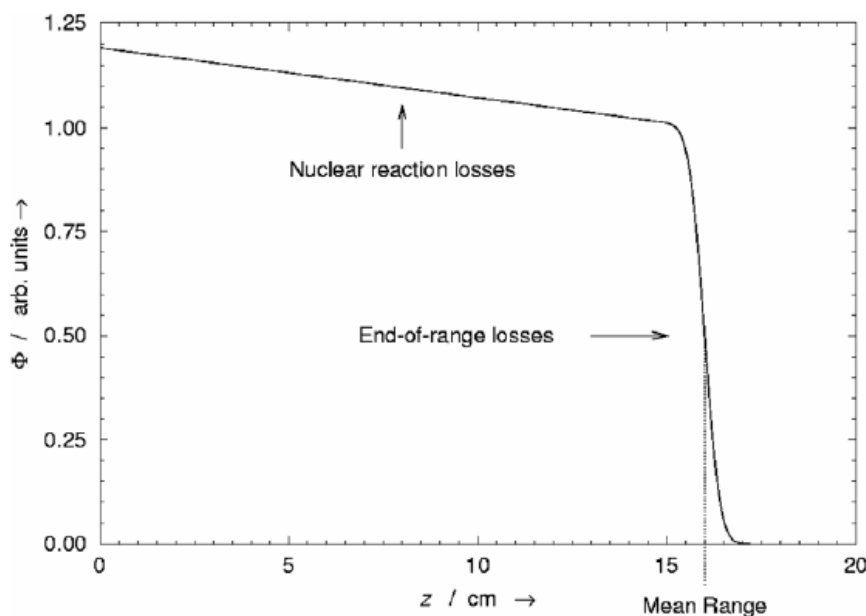


Figure. 2.2 The relative fraction of the fluence in a broad beam of protons remaining as a function of depth z in water [5].

nearly equal projected and CSDA ranges, in PT, the range definition typically refers to the **Mean Projected Range** R_0 . It is the depth at which half of the protons have stopped in the medium, excluding the effect of nuclear interactions (illustrated in Fig. 2.2).

In PT range experiments, the mean projected range can be measured using a “Faraday Cup” (FC), which records the charge of the proton beam after it has traversed an adjustable thickness of the material. One can then estimate the range of the proton beams by determining the required thickness of a material in order to stop half of the incident protons when the nuclear interactions are not considered. Simply, one can measure the range in terms of dose/energy deposition via scanning a dosimeter along the depth z in a water phantom. The R_0 measured by dose can be defined as [5]:

$$R_0 = d_{80}, \quad (2.6)$$

where d_{80} refers to the depth of water (corrected for the water phantom entrance window and the dosimeter wall thickness) at the distal 80 % point of the peak. The 80 % value used in this definition is an approximation value that was first suggested by A. M. Koehler *et al* [57], and has since been confirmed theoretically and experimentally.

So far, only the beam stopping in the longitudinal direction has been discussed, neglecting the scattering of beam on the transverse plane. ‘Multiple Coulomb Scattering’ (MCS) describes the beam spreading in the medium as shown in Fig. 2.1 (b). When a proton passes near the centre of the atom where the nucleus is located, it gets repelled from the target nucleus, so that its trajectory is changed and it loses energy. The MCS angular distribution for thick targets (such as in PT) is typically considered to be Gaussian. Furthermore, there are many ways to describe the scattering angle [5, 4] and we do not cover those equations here, as the scattering angle does not affect the range. One thing we should notice is that the broadening of the beam width coming from the MCS interactions increases with the incident proton energy.

Nuclear interaction

Nuclear interactions in PT are much harder to model than the EM interactions, but their biological effect is small. In this section, we focus on the inelastic nuclear interactions in PT, revealing their effect to the BP curve. Inelastic interaction occurs when the energy is not conserved, for example:



In this case, the incident proton lost energy (equal to the binding energy) to knock out one α particle in the target nucleus, so that the ${}^{16}\text{O}$ becomes ${}^{12}\text{C}$. Another typical interaction of proton - ${}^{16}\text{O}$ is given by:



during which process the final nucleus remains the same as the target nucleus, while the energy is not conserved either. The above nuclear interaction (Eq. 2.8) indicates the incident proton loses some energy to excite the target nucleus ${}^{16}\text{O}$ to a higher quantum state ${}^{16}\text{O}^*$. The inelastic interaction is the primary process in proton-tissue interactions for the generation of secondaries (i.e. protons, neutrons, gammas, heavy fragments such as alphas, and the recoil residual nucleus). The probability of a nuclear interaction to occur can be characterised by the **Cross Section**, denoted as σ with units of barn ($1 \text{ barn} = 10^{-28} \text{ m}^2$). The cross section for all interaction processes is the total cross section. Fig. 2.3 shows the cross-section of

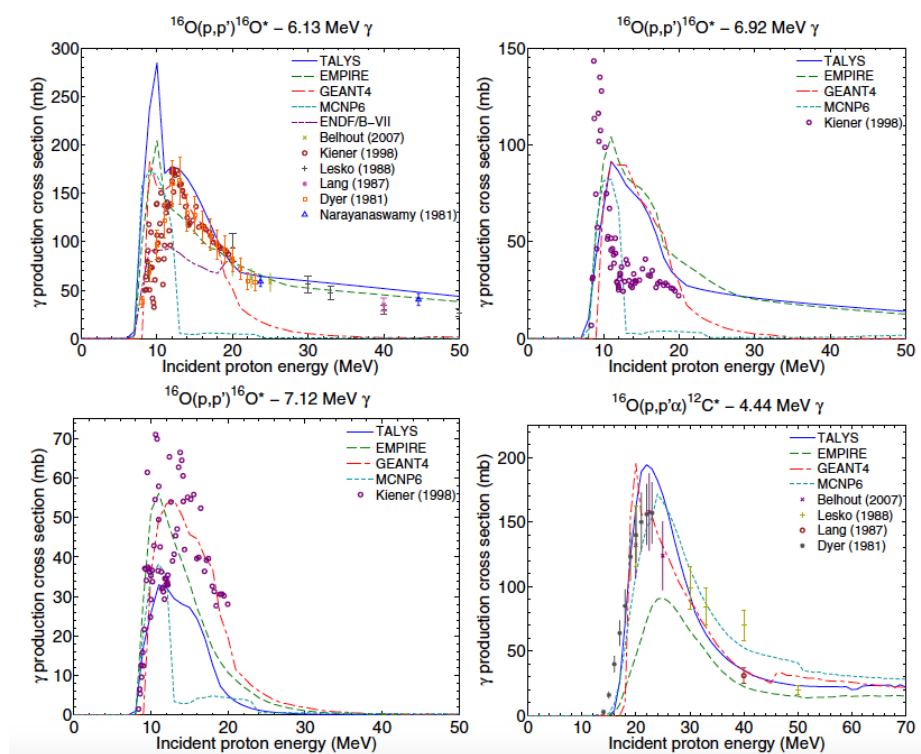


Figure. 2.3 Cross section of 4.44, 6.13, 6.92 and 7.12 MeV gamma-ray emission from proton - ^{16}O nuclear reactions [6].

several proton-induced reactions on ^{16}O . This cross section of $^{16}\text{O}(p,x\ \gamma\ 4.44\ \text{MeV})^{12}\text{C}^*$ shows the highest interaction probability when the incident proton energy is around 22 MeV, while the cross section for $^{16}\text{O}(p,p'\ \gamma\ 6.13\ \text{MeV})^{16}\text{O}^*$ peaks at around 12 MeV. These two gamma-ray emission from proton - oxygen irradiation dominate in clinical PT.

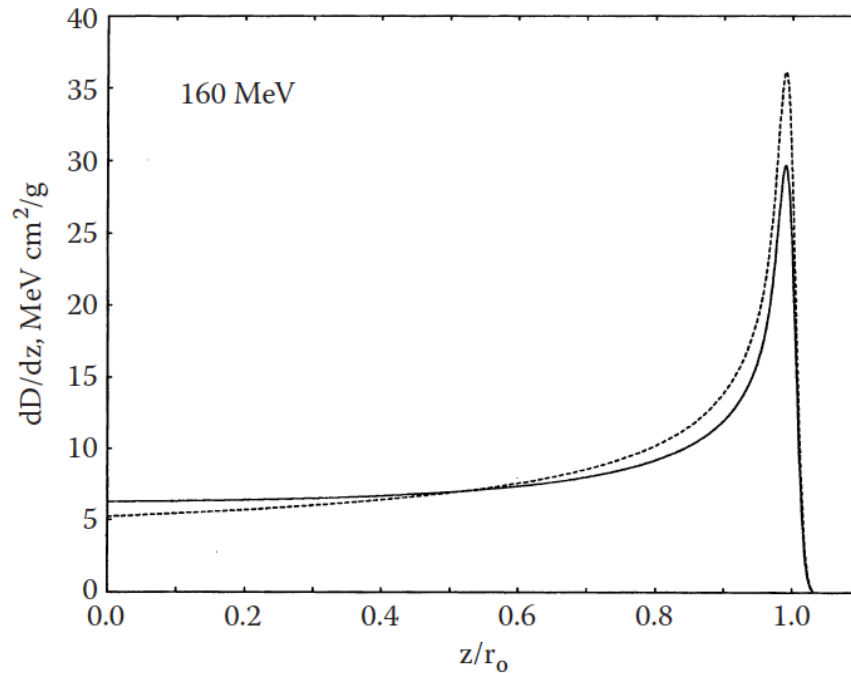


Figure. 2.4 Bragg peak curves of 160 MeV proton beam in water when the nuclear interaction is considered (solid line) and excluded (dashed line) [5].

In contrast to EM interactions, the nuclear interactions scatter the proton to a large angle, so the total fluence reduces gradually from 0 to 15 cm as illustrated in Fig. 2.2. Moreover, the dose on the entrance part is enhanced, while that in the BP region is reduced (see Fig. 2.4) during the nonelastic interactions, since protons have been removed from the EM peak and secondary radiations deposit their energy further upstream. However, their effect to the calculation of range can be neglected.

2.1.2 Uncharged-particle interactions in matter

Gamma-ray interaction

Gamma rays consist of short EM waves and so possess high photon energy. Photons have zero mass, no charge and their energy can be characterised with the **Planck-Einstein** relation:

$$E = hf = \frac{hc}{\lambda}, \quad (2.9)$$

where h represents the Planck constant, f represents the frequency of the photon, c represents the speed of light and λ represents the wavelength of the photon. Since these particles are neutral, they do not lose energy continually via Coulomb interactions with atomic electrons, as the charged particles do. In contrast, they interact with matter stochastically via three primary interactions: photoelectric effect, Compton scattering and pair production. The probability of these interactions to occur per unit path length in the absorber material is reflected in the linear attenuation coefficient (μ , cm^{-1}), when we consider that a narrow photon beam penetrates a medium. The attenuation of the photon beam intensity (I) is given by the following relation:

$$I = I_0 e^{-\mu t}, \quad (2.10)$$

where I_0 is the initial photon intensity, I is the number of the transmitted intensity and t is the thickness of the absorber (in units of cm). Alternatively, the mass attenuation coefficient can be expressed as μ/ρ in units of cm^2/g , compensating for the density dependence of the coefficients on the material being traversed. The total linear attenuation coefficient is the sum of the probability of the three primary interactions[7]:

$$\mu = \tau_{\text{photoelectric}} + \sigma_{\text{compton}} + \kappa_{\text{pair}}. \quad (2.11)$$

The photoelectric effect represents the emission of an energetic photoelectron when a photon hits an absorber atom, during which process the photon has been completely absorbed. The initial photon energy should meet the threshold:

$$E_e = hf - E_b, \quad (2.12)$$

where E_b represents the binding energy of the photoelectron in its original shell. The photoelectric process dominates when the material has a high atomic number Z and the initial photon energy is relatively low (see Fig. 2.5).

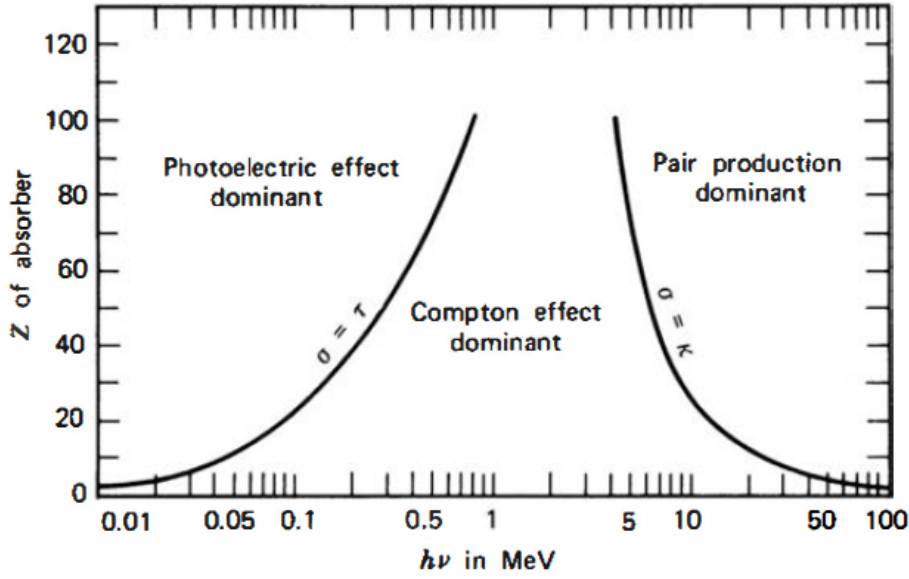


Figure. 2.5 The photon interaction mechanisms [7].

Compton scattering becomes the dominant process for photon interaction when the photon energy is on the range from 100 keV to 10 MeV (for $Z \approx 20$) and is only weakly dependent on the material atomic number Z . The Compton scattering formula is given by the following relation:

$$\cos(\theta) = 1 - \frac{(E_p - E'_p)m_e^2}{E_p E'_p}, \quad (2.13)$$

where θ is the scattering angle, E_p is the produced gamma-ray energy (before scattering), E'_p is the detected gamma-ray energy (after scattering), m_e is the electron mass and c is the speed of light. This formula can be applied for the Compton gamma camera in detecting the PGs to retrieve the vertex of the gamma-ray interaction.

The probability of Compton scattering decreases with increasing photon energy and pair production, which starts to occur for photon energies higher than 1.022 MeV, slowly takes over and becomes the most prominent process as the photon energies increase further. When the photon passes near the nucleus of an atom, it is subject to the strong EM field from the nucleus and may produce a positron-electron pair if its energy exceeds the rest mass (2×0.511 MeV) for those particles. Thus, the kinetic energy of the produced electron and positron can be calculated by:

$$E_{e^+} + E_{e^-} = hf - 1.022 \quad (\text{MeV}). \quad (2.14)$$

As shown in Fig. 2.5, the probability of this process increases with the atomic number Z and photon energy.

Neutron interaction

Neutrons can interact easily with the nucleus and penetrate deeply into matter, since they are electrically neutral. Unlike photons, which interact mostly with the orbital electrons of an atom, neutrons primarily interact with the nucleus and neutron interactions can take place at any energy. For dosimetry purposes, it is convenient to divide the neutron fields into three energy categories: thermal neutrons (less than 0.5 eV), intermediate-energy neutrons (0.5 eV - 10 keV) and fast neutrons (10 keV upward) [56]. The typical energy range of neutrons generated in PT covers all the three categories (i.e. from thermal to fast neutrons) and the maximum neutron energy depends on the incident proton energy.

The cross section of neutron interactions depends on the target nucleus and the neutron energy. In general, the cross section decreases with increasing energy. When the neutron energy is below 1 MeV, the elastic cross section is nearly constant, while the inelastic cross section and absorption cross section are proportional to the reciprocal of the neutron's speed. At high energies, the cross section may have large peaks (called resonances) that occur where reactions with nuclei are enhanced [58]. The attenuation law discussed above for photons is also valid for neutron transmission. The detailed neutron interactions in human tissues (i.e. four-element composition: C, H, O, N) are not discussed here, since the neutron dosimetry is irrelevant to the main topic of this work. Thus, we only consider the fast neutrons that can penetrate human tissues to the environment. These fast neutrons induce substantial background noises for the detection of interested PG signals, and the noise level increases with the incident proton energy. Finally, it is required to include dedicated shielding techniques for neutron absorption or data acquisition strategies to reject neutron-induced noises (e.g. timing selection), improving the Signal-to-Noise Ratio (SNR) of our PGs.

2.2 Absorbed dose and relative biological effectiveness

One of the most commonly used terms in radiotherapy is **absorbed dose**, D , which indicates the energy absorbed per unit target mass at some point in a radiation field. We usually use the unit Gy for D in radiotherapy: $1 \text{ Gy} = 1 \text{ J/kg}$. For a typical case in PT, a total of 70 Gy dose can be prescribed to a tumour volume of around 1000 cm^3 , given in 35 fractions (2 Gy/fraction). The absorbed dose can be related to the mass stopping power (as described with Eq. 2.1) and proton fluence. Considering dN protons pass through an infinitesimal

cylinder of cross sectional area dA and thickness dx , in the cylinder [5]:

$$D = \frac{\text{energy}}{\text{mass}} = \frac{(dE/dx) \times dx \times dN}{\rho \times dA \times dx} = \phi \frac{S}{\rho}, \quad (2.15)$$

giving that dose equals fluence times mass stopping power. The above equation can also be transformed to be expressed in unit Gy:

$$D = \frac{0.1602\phi S}{\rho} \text{ Gy}, \quad (2.16)$$

with ϕ in Gp/cm^2 , $1 \text{ Gp} = 10^9$ protons, and S/ρ in $\text{MeV}/(\text{g}/\text{cm}^2)$, $1 \text{ MeV} = 0.1602 \times 10^{-12} \text{ J}$. Those equations are useful for estimating the dose rate from a proposed machine and beam line, however they cannot be used for the determination of therapy dose delivered to a patient (i.e. only with a carefully calibrated dosimeter). During the EM interactions, the protons deliver most of their energy/dose to the medium via ionisation of the atomic electrons. Nuclear interactions plays a small part (i.e. around 10 %) in the absorbed dose due to the removal of protons, see Fig. 2.4. Some heavy fragments like α particles generated during non-elastic interaction can affect the absorbed dose as well, but those effects are negligible since the production of those ions is less than 1 % and they have a very short range, depositing their energy locally [5]. Another concept in proton therapy is related to the biological effect of protons compared to photons, given by **Relative Biological Effectiveness** (RBE). For different types of radiation, the dose-response relationships are different. Protons are light charged particles that are more biologically effective than photons, which means a lower dose is prescribed in PT to cause the same biological effect than photon therapy. The reason that protons have a slightly better biological effectiveness is related to radiobiology, which is not covered here. Thus, the RBE value of protons is just an estimation from clinical experience. The RBE is defined as the dose of reference photons, D_x , divided by the proton dose, D_p , in order to achieve the same biological effect [5]:

$$\text{RBE} = \frac{D_x}{D_p}. \quad (2.17)$$

The prescription of dose in PT based on clinical experience, corresponds to an $\text{RBE}_{\text{proton}}$ of around 1.1.

2.3 Gamma-ray detection with scintillator detectors

2.3.1 Scintillating material

The use of scintillating materials to detect ionising radiation constitutes a commonly used detection method. It has been applied in many areas that require the detection and spectroscopy of a wide assortment of radiations with medical applications being no exemption. Scintillating materials can be classified into two main categories, inorganic crystals (such as alkali halide crystals, e.g. sodium iodide) and organic based liquids and solids (such as scintillating plastics). The scintillation mechanism is different in these two types of material. For inorganic crystals, the scintillating process depends on the structure of the crystal lattice. In pure crystals, the electrons can only occupy the valence band and there is a band gap between the valence and conduction band. The absorption of radiation energy elevates electrons from the valence band to the conduction band leaving a gap in the valence, and the return of an electron to the valence band generates a photon. This scintillating process is inefficient in pure crystals, so small amount of impurities are added to the crystal, called activators, creating special energy states within the original band gap of the pure crystal such that the excited electrons can de-excite through these states back to the valence band. Fig. 2.6 illustrates the energy band structure of activated scintillating crystals, which shows a much narrower energy gap between activator states than the band gap. As a result, the emitted photon spectrum is shifted to longer wavelengths (visible range) and is also not absorbed by the bulk material of the crystal.

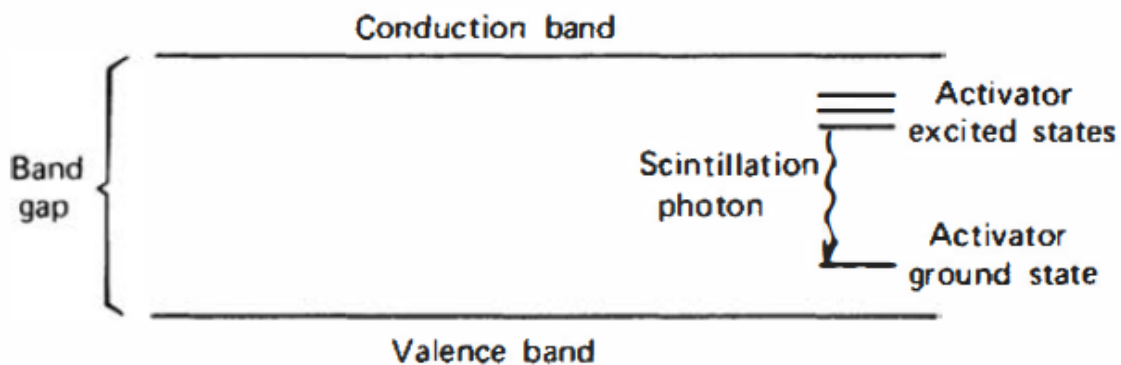


Figure. 2.6 Energy band structure of activated crystalline scintillators [7].

The organic scintillating mechanism is different than that in inorganic crystals, and arises from transitions in the energy levels of a single molecule rather than between band gaps in a crystal structure. The energy levels in a molecule can be presented with the pi-electron structure, as shown in Fig. 2.7. The singlet energy levels (spin = 0) are labelled as S_0 (ground

state), S_1 , S_2 and S_3 . The spacing between S_0 and S_1 is around 3 - 4 eV while the spacing between excited states is smaller. We can also see the fine structure in each of the S states and the spacing for these subdivided levels is around 0.15 eV. Radiations transfer energy to the molecule when they pass through the material, exciting the molecule to higher energy levels. The excited states in an S band quickly de-excite to S_{10} state via internal conversion (in ps) and then decay to the ground state, emitting scintillation light via a process known as prompt fluorescence. Thus, most of the organic scintillators are fast (compared to scintillation produced by inorganic crystal) as the decay time of fluorescence is in the order of few ns. Another process that can occur if the molecule is excited in one of the triplet levels and then decays to the S_0 single state (ground state), is known as phosphorescence and this process generates longer wavelength emission light and is typically much slower than the fluorescence as it connects two different quantum configurations.

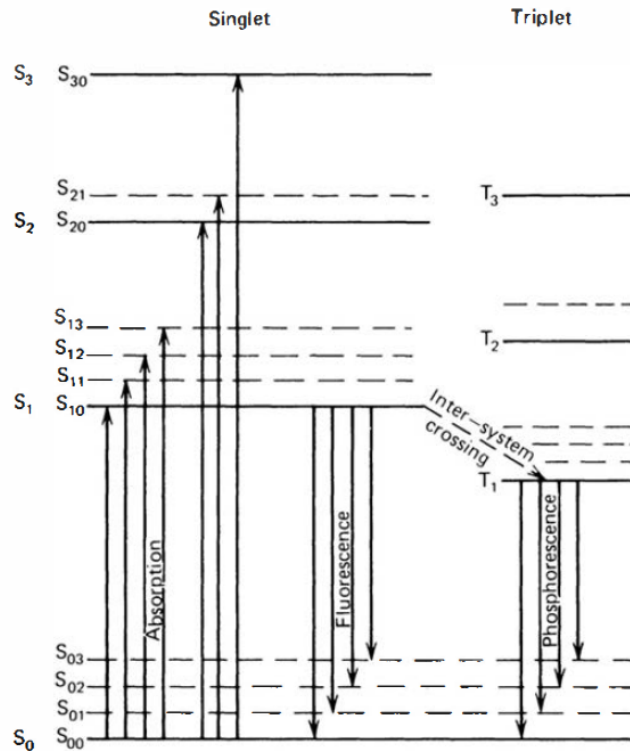


Figure. 2.7 Energy levels of an organic molecule with pi-electron structure [7].

organic scintillator materials have been applied widely for medical applications regarding radiotherapy dosimetry due to their water equivalence and minimal perturbation of the radiation field. However, the non-proportional between the scintillating signal and the energy deposition was observed for high energy electrons and for heavy charged particles, which process is known as the quenching effect. The ionization quenching can be modeled by

the Birk's law by two parameters, known as Birks parameter, which quantifies the relation between light production and stopping power [59]. Here, we briefly introduce the formula of the Birk's law, which describes the production of light by electrons traversing a slab of scintillator material:

$$\frac{dL}{dx} = \frac{A \frac{dE}{dx}}{1 + kB \frac{dE}{dx}}, \quad (2.18)$$

where dL is the light yield for a single primary electron per unit of path length dx in the scintillating material with the ionization density, and A is the scintillator efficiency and kB is a quenching parameter [59]. In this project, we have not yet corrected the scintillating quenching effect by Birk's law, since our topic is related to range verification rather than proton dosimetry.

The fluorescence emission is the most important process in scintillating material, so the radiation detection using scintillator detectors is indirect in the sense that the energy lost by the radiation is first converted into scintillation light before being detected by photosensors. The inorganic crystals are usually dense (high atomic number Z) to increase the interaction probability and the light yield in these crystals is much higher than that in the scintillating plastics. Thus, scintillating crystals are mostly used for the measurements of gamma-ray energy spectroscopy, while the plastics have very short decay time that can be used for fast timing pick up in charged particle detection.

2.3.2 Photosensors for scintillator detectors

Radiation detection using scintillating materials is an indirect measurement of ionising radiation, and relies on effective detection of the scintillation light emitted by the material. In a scintillator detector, the relatively weak scintillation light emission needs to be converted to an electric signal for further signal processing using a photosensor. One of the best known photosensors is the photomultiplier tube (PMT), which remains the most widely used photosensor for converting weak light signals into a usable current pulse. The weak scintillation light (no more than a few thousand photons) interacts with the photocathode material where it is and converted to low energy electrons (known as photo-electrons) inside the vacuum tube. These photo-electrons are first amplified internally through a series of dynodes that are at different voltages. The electrons accelerate considerably between the dynodes and once they reach the next dynode each of them can cause multiple other electrons to be emitted. The final amplified electron signal has typical gains in the order of 10^7 to 10^9 , which is sufficiently large to be monitored with instruments [7].

There are many advantages of PMT for scintillator light readout. Firstly, the amplified charge signal is almost proportional to the original light yield, providing a good linear response. Additionally, the random noise from the amplification is low so that the detected signal is still distinguishable when the initial photon number is low. The quantum efficiency (QE) of PMT is usually 20 to 30 %, which defines the sensitivity of photocathode [7]:

$$QE = \frac{\text{number of photoelectrons emitted}}{\text{number of incident photons}}. \quad (2.19)$$

The QE of any photocathode is strongly dependent on the wavelength of incident light, and the current upper limit of QE is around 30 %. On the other hand, the Silicon photomultipliers (SiPMs) are becoming more appealing in medical application with their superb performances in terms of high QE, compact design and fast timing response. SiPMs are insensitive to magnetic fields, enabling solutions for hybrid medical imaging systems that involve magnetic fields, such as PET/MRI and SPECT/MRI. The small size of SiPMs offers also flexibility in the design of modern imaging systems achieving much more compact instruments and a higher spatial resolution compared to e.g. traditional PET/CT scans. SiPMs consist of an array of photosensitive microcells, called single-photon avalanche photodiodes (SPAD) operating in Geiger mode. A typical SiPM has microcell densities of between 100 and several 1000 per mm², depending on the size of the microcell [8]. When a single photon hits one of the microcells, it generates electron-hole pairs which are then accelerated under the influence of a strong electric field. The fast moving electrons produce an avalanche of secondary electrons, causing a photocurrent to flow through the microcell. During this time the microcell is no longer responsive for approximately hundred of ns before it recovers. In the meantime, other microcells on the same SiPM are not affected and are ready to detect photons. The sum of all photocurrent produced from the microcells of a single SiPM provides a measure of the energy of the gamma ray absorbed in the scintillator. In an analog SiPM, signals from microcells are firstly summed up and then digitised to provide the timing and energy information.

Overall, the SiPMs have a comparable gain (around 10⁶) with PMT, but with all the advantages of a solid-state sensor. SiPMs are sensitive to single photon and its photon detection efficiency (PDE) can be as high as 40 % at a certain light wavelength [8]. One of the disadvantages of SiPM is its relatively small dynamic range which causes saturation and introduces a non-linear response for high energy gamma rays, leading to the incident scintillation photon flux to be comparable to the total number of microcells in the active area, as shown in Fig. 2.8, due to the intrinsic dead time of each microcell that has been triggered

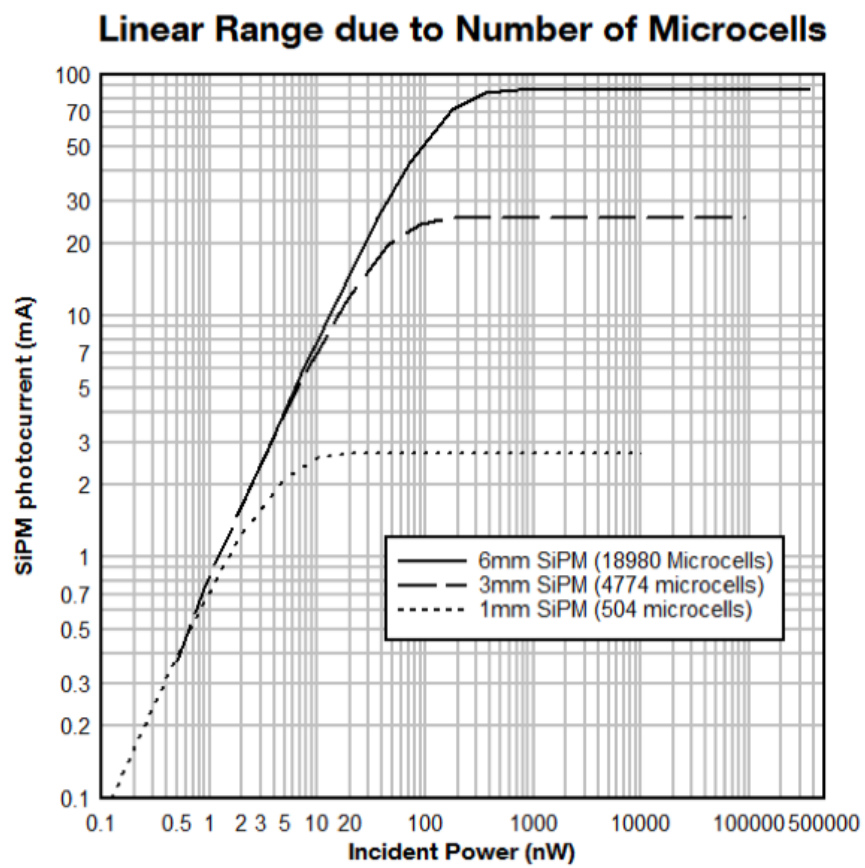


Figure. 2.8 The SiPM photon-current as a function of incident power on a log-scale [8].

by a photon. The details of non-linearity in SiPM will be discussed further in Chapter 3, subsection 3.3.1 for the LYSO detector.

2.4 Summary

As proton beams penetrating human body, protons primary interact with the orbital electrons via Coulomb interactions, depositing energy/dose along the beam path. The energy loss rate per unit path length is characterised by the Beth-Bloch formula considering both the relativistic and quantum effects. The range of the proton beams in the tissue can be calculated analytically from the formula. In the meantime, a relatively large quantity of protons are also scattered by the target nucleus via the elastic Coulomb interactions (i.e. MCS), causing the beam profile to spread along the beam path. We did not describe the scattering angle from MCS, since the angle is not related to the range.

A relatively small number of protons interact directly with the nucleus via proton-nuclear interactions, producing secondary particles and recoiled ions. These interactions do not affect the range. The cross section for nuclear reactions peaks as the beam slows down reaching a maximum at around 20 MeV, which is close proximity to the BP region. Thus, the PGs that are emitted along the depth can be used in order to deduce the location of the BP, and provide an indirect real-time method for range verification.

On the other hand, gamma-rays interact with matter mainly through photoelectric effect, Compton scattering and pair production. The probability of those interactions depends on to the atomic number of the target material and the gamma ray energy. The fluorescence processes in organic and inorganic scintillation materials were also explained. The scintillating plastics have short decay time and can be applied for the timing measurement of charged-particles, while the crystalline scintillators are dense and have high light yield so that they are commonly used for gamma-ray spectroscopy. Moreover, the photosensor is an essential component in radiation detection using scintillators, which converts weak scintillating photons to detectable electron signals for other instruments.

Chapter 3

The configuration of a new Prompt Gamma-ray Imaging detection system

In this chapter, we present the configuration of the PGI detector prototype that was developed as part of this thesis project and consists of three types of scintillator detectors and mechanical collimators. The data acquisition (DAQ) systems are also introduced, from the analog signal processing system to the latest digital signal processing system. Finally, the results regarding the characteristics of the detectors are presented.

3.1 Experimental setup

In this section, we discuss the experimental setup that was developed as part of this thesis project. The setup comprises of two bespoke inorganic scintillator detectors for gamma-ray detection and two plastic scintillators for charged-particle measurements. The setup also includes a purpose-built multi-slit collimator and a computer controlled linear stage. Finally, the setup includes different phantoms based on water, PMMA, Calcium hydroxide etc.

In particular, a dual gamma-neutron scintillator detector based on CLLB ($\text{Cs}_2\text{LiLaBr}_6:\text{Ce}$) was used for high energy resolution measurements of PGs. The detector was placed behind a single-slit collimator created by two lead blocks. The second gamma-ray detector was based on multi-arrays of LYSO detectors placed behind a multi-slit collimator based on tungsten sheets. The purpose of this latter detector was to provide the 1D PG intensity profile along the depth of the proton trajectory in the phantoms. Moreover, a scintillating fibre detector was designed to measure the energy deposition of proton beams in a water phantom. To obtain the timing of the primary proton beams, we also designed a dedicated plastic scintillator as the start counter placed in the beam line. In the following sections, the detection systems are

presented in detail together with their performance obtained using radioactive sources in the laboratory.

3.1.1 Targets

Fig. 3.1 shows the targets used in this project, including three solid targets and two water phantoms. Unlike the solid targets, the liquid water was enclosed in the plastic containers with an open slit on the top. Two sizes of water container ($5 \times 5 \times 5 \text{ cm}^3$ and $4 \times 8 \times 27 \text{ cm}^3$) were made in-house to stop different proton beam energies. The solid targets were made from graphite ($5 \times 5 \times 5 \text{ cm}^3$, density $\approx 1.7 \text{ g/cm}^3$), PMMA ($3 \times 3 \times 3 \text{ cm}^3$, density $\approx 1.19 \text{ g/cm}^3$) and calcium hydroxide (4 cm-length and 7 cm-diameter, density $\approx 1.32 \text{ g/cm}^3$) respectively. The calcium hydroxide ($\text{Ca}(\text{OH})_2$) cell, which was originally in powder form had been pressed in-house into a solid disk. It could be positioned at different depths inside the water phantom 2 to reproduce different therapy scenarios.

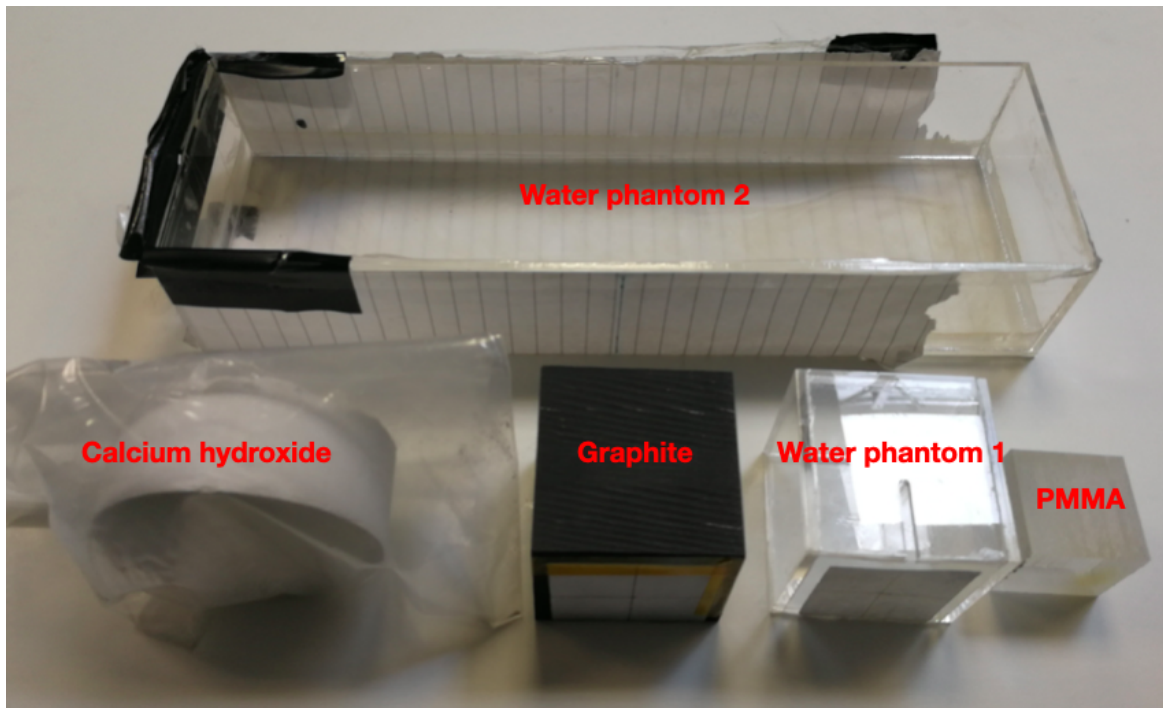


Figure. 3.1 A photograph of targets used in this project. There are two water phantoms with different volumes and three solid targets made from graphite, PMMA and calcium hydroxide respectively.

Each phantom can be placed on the top of a linear stage that can move in the beam direction with a sub-millimetre resolution. The movement of the stage was controlled by a laptop to ensure the scanning of the 1D PG emission along the depth of the phantom during

the in-beam experiment. The laptop runs an in-house developed software to control the linear stage and can also be remotely controlled from e.g. the control room. As described above, the PG yield along the depth can be recorded in the detector with the movement of the phantom via the linear stage.

3.1.2 Single-slit collimated CLLB detection system

As discussed in section 2.1.2, the photoelectric effect and pair production probabilities increase with the atomic number Z of the medium. To increase the gamma-ray detection efficiency, a scintillator with relatively high density and atomic number is desired. Its peak emission spectrum should also match the region of maximum QE of the SiPMs. For spectroscopic studies, the detector should also provide excellent energy resolution, high light output and fast timing response. Considering the above factors we have chosen the CLLB for the energy spectroscopy of the PGs.

The CLLB is a dual gamma-neutron sensitive scintillator detector that has been utilised in homeland security (see Appendix A for the CLLB data sheet). The ${}^6\text{Li}$ enriched crystal allows for thermal-neutron detection which can be separated from a gamma-ray source via pulse-shape discrimination (PSD) and has an excellent energy resolution of around 4 % at 662 keV for gamma-ray detection. This detector has a decay time constant of 180 ns which is not as fast as other scintillators such as LaBr_3 (16 ns) or LYSO (40 ns), but is still relatively fast. The density of this material is around 4.2 g/cm^3 , which is comparable with that of the traditional NaI(Tl) crystal with 3.67 g/cm^3 , see Appendix A for the properties of different scintillators. In this project, two CLLB detectors with similar properties but different sizes (1 inch and 1.5 inch) were prepared for the PGS study.

Fig. 3.2 is a schematic drawing of the CLLB detection system placed behind the single-slit collimator created by two lead blocks. We introduce the definition of FoV of the collimation system in detecting PGs that are emitted from the water phantom. The distances indicated in Fig. 3.2 are: D stands for the diameter of the phantom, d_1 represents the distance from the front face of the collimator to the surface of the phantom, d_2 represents the depth of the collimator and w stands for the width of the open slit. The FoV of the detector can be calculated by:

$$FoV = w \times \left(1 + \frac{2d_1}{d_2} + \frac{D}{d_2}\right) \quad (3.1)$$

The open slit width is around 3 mm, the collimator depth d_2 is around 100 mm and the beam-to-collimator (i.e. $D/2 + d_1$) distance is around 110 mm, defining the FoV to be around 9.6 mm. The CLLB has a volume of 1-inch in diameter and length, which was coupled

directly to SiPMs for signal readout. A larger CLLB detector with 1.5-inch in diameter and length was also prepared as an alternative for the PG measurements.

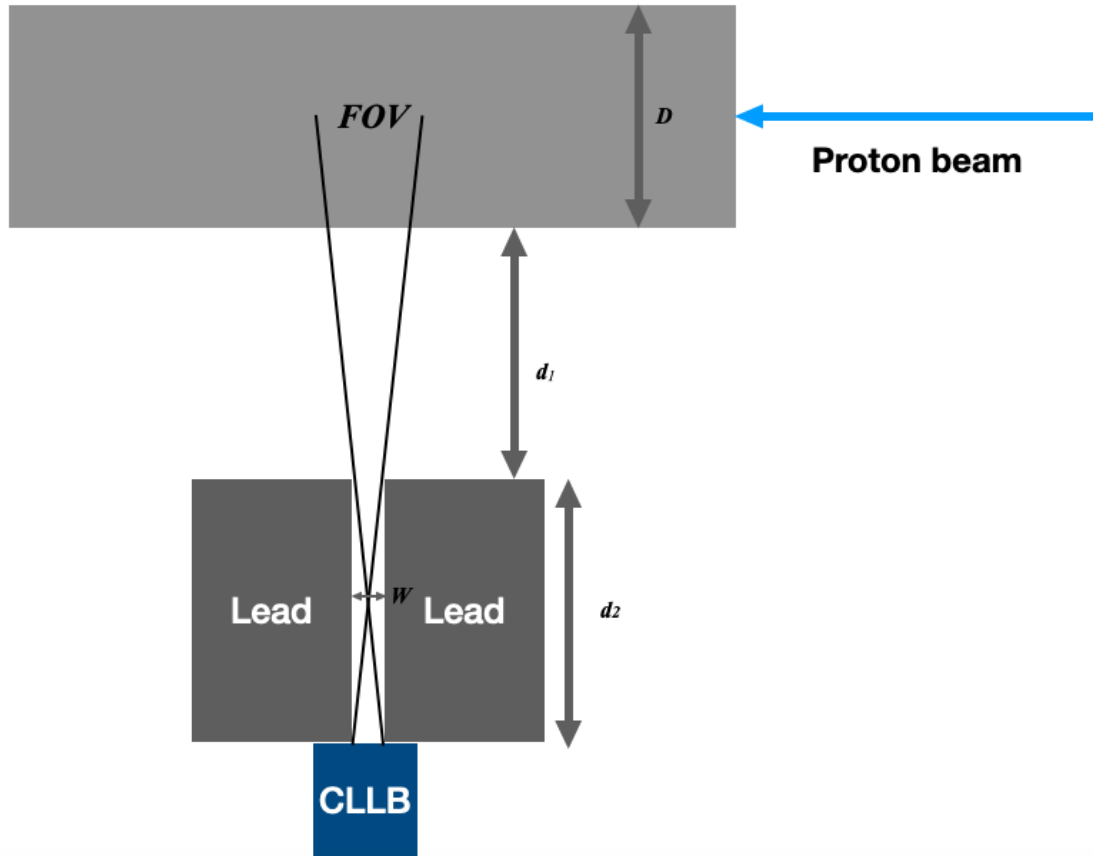


Figure. 3.2 Schematic drawing (top view) of a CLLB detector collimated by two lead blocks.

3.1.3 Multi-slit collimated LYSO detection system

In the meantime, we also prepared a detection system based on arrays of LYSO detectors that align with a purposely built multi-slit tungsten collimator for absolute 1D range measurements. Each of the 8 LYSO detector arrays consist of 16 crystals (4×4 array) and each individual crystal has a size of $3.2 \times 3.2 \times 50 \text{ mm}^3$, as shown schematically in Fig. 3.3. The LYSO crystal is a dense material (7.1 g/cm^3) with high atomic number and hence has high stopping power for high energy gamma-rays compared to other scintillating materials. It also has a rather fast decay time (42 ns), relatively high scintillating light output and a modest energy resolution of around 10 % at 662 keV. This type of scintillating crystal has been commercially used in medical imaging systems, such as ToF PET/CT [60–62], albeit with

smaller lengths compared to the ones chosen here. The excellent performance of timing resolution and high cost-effectiveness make this material an optimal choice to build the PGI prototype. The size of each crystal channel was custom made to match the SiPMs (Hamamatsu MPPC, [63]) with 100 % fill factor for optimum light collection. The length of the crystal was also custom made to be 50 mm, i.e. a factor of two longer than the crystals used for PET imaging, increasing the high energy PG detection efficiency compared with traditional PET/CT (20 mm, for 511 keV photons). We also prepared another 8 LFS (Lutetium Fine Silicate) detectors (same configuration with the LYSO detectors) in this project. The LFS crystal has similar properties compared to the LYSO crystal [64].

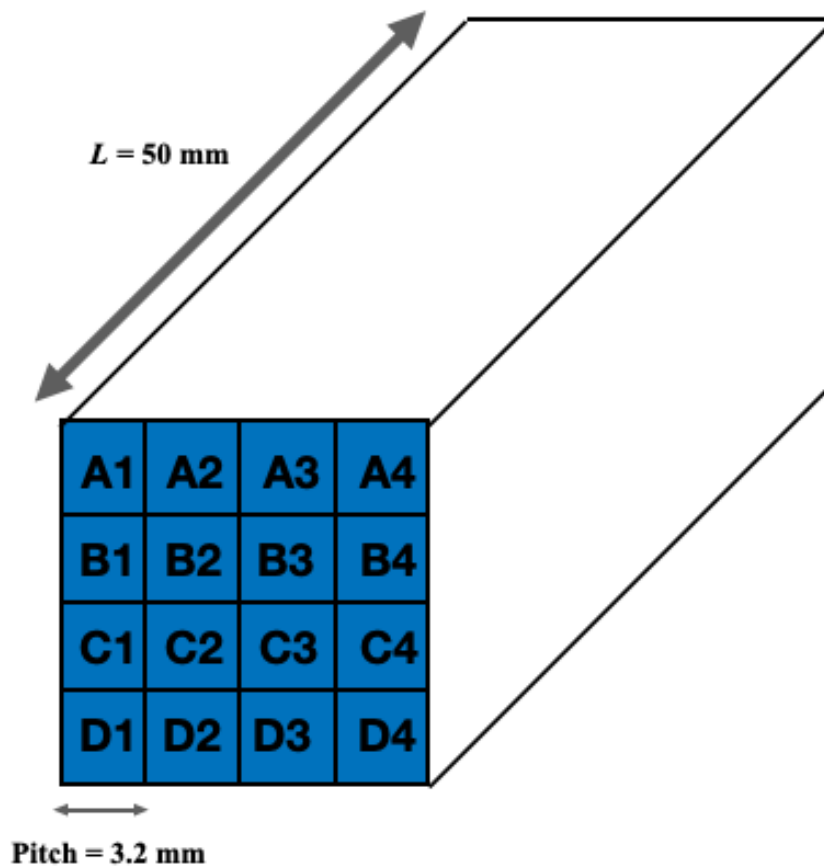


Figure. 3.3 Schematic drawing of a LYSO detector array with 16 crystals.

A total of 8 LYSO detectors were aligned with the multi-slit tungsten collimator, as shown in Fig. 3.5 and 3.4. The pitch of the collimator is 3.2 mm, with a width (w_1) of the tungsten slabs of 1 mm and a slit gap (w_2) to be 2.2 mm to match the LYSO pixel size. The height of the collimator opening is 13 mm matching the height of LYSO detector and the depth of the collimator d_3 is 70 mm. The beam-to-collimator distance (i.e. $D/2 + d_4$) is around 112 mm.

All the tungsten slits were supported by four pieces of lead sheets to cover the top, bottom, left and right sides of the tungsten collimator with the front and end surfaces open for PG detection. The entire collimation system (lead + tungsten) was machined in-house and held together with an Aluminium case for safety, rigidity and compactness, see Fig. 3.4.



Figure. 3.4 A photography of the multi-slit collimator with eight LYSO detector arrays arranged behind its slits, leaving one every five slits without being seen by the detectors..

These LYSO detector arrays were placed in a row behind the tungsten collimator, and one every five gaps of the collimator were not covered by LYSO crystals. In other words, between each two LYSO arrays, for example $LYSO_0$ and $LYSO_1$ in Fig. 3.4, there was a gap left to compensate for the thickness of external case of each LYSO detector array.

Similar to section 3.1.2, the FoV_1 and FoV_2 defined by the dimensions of the multi-slit collimator can also be calculated using Eq. 3.2, and is found here to be around 9.2 mm.

$$FoV_1 = FoV_2 = w_2 \times \left(1 + \frac{2d_4}{d_3} + \frac{D}{d_3}\right) \quad (3.2)$$

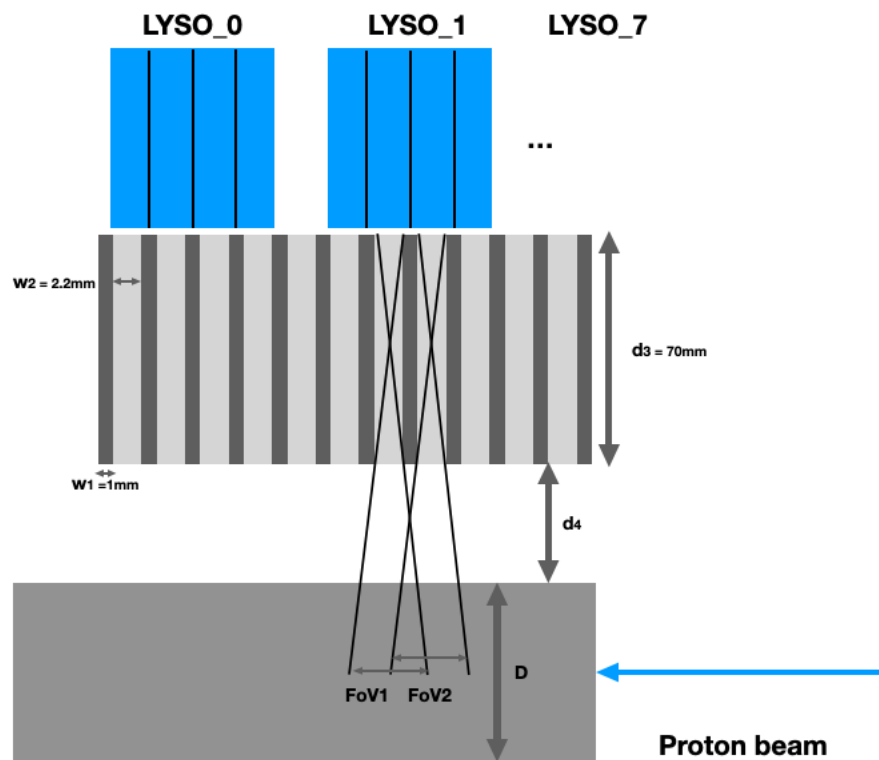


Figure. 3.5 A schematic drawing (top view) of the LYSO detector arrays that aligned behind the multi-slit tungsten collimator and with a view of the phantom through the collimator's slits.

However, there is an overlapping area between two continuous $FoVs$ of the multi-slit collimation and the projected overlapping area in the beam direction can be calculated by Eq. 3.3, giving around 2.6 mm.

$$\text{Overlapping view} = w_1 \left(1 + \frac{D}{d_4}\right) \quad (3.3)$$

The total FoV of multi-slit collimated LYSO detector is around 130 mm, together with the 7 gaps, one between each detector array. The proton range can be retrieved with the statistics of PG events recorded in these 128 LYSO crystals. For this purpose, a multi-channel readout data acquisition system (DAQ) is necessary to record the energy and timing of the detected gamma-rays. More details regarding the multi-channel DAQ system are discussed in section 3.2.3.

3.1.4 Fibre probe and plastic counter

As discussed earlier, the organic scintillating material, such as plastic scintillator, has a very short decay time of fluorescence (i.e. a few nanoseconds) in a molecule, making this material an optimum choice for fast timing measurements. Moreover, the plastic scintillator has a similar density (around 1.05 g/cm^3) with water, and can be considered as a water-equivalent material for dosimetry purposes. In this project, we designed two detector prototypes based on scintillating plastics for the measurements of energy and timing of incident protons.

In a parallel project, we developed a beta microprobe with thin scintillating fibres for small animal PET activity monitoring [65]. The fibre probe consists of 5 scintillating fibres (Saint-Gobain Model BCF-10, [66]) with a size of $250 \mu\text{m}$ each in diameter. A layer of white paint was added as a light reflector, then another layer of black paint outside the white layer to ensure light tightness, so the diameter of the fibre probe is around 1.45 mm. The small amount of scintillating light was collected and amplified by a SiPM with an active area of $1 \times 1 \text{ mm}^2$, as shown in Fig. 3.6. This fibre probe shows accurate timing and activity measurements for positron emitters in small animal PET experiments. In this project work, the fibre probe was repurposed to measure the energy deposition of proton beams along the depth of a water phantom, as the protons interact with water via electromagnetic interactions generating secondary electrons. The fibre-based dosimeter is water-equivalent and has a small size, compared with traditional ion chamber that is a gas detector (i.e. correction factor needed for dose measurements) and has a detecting area of a few centimeters.

As mentioned in the beginning of this section, the organic scintillating material has a fast timing response which suits the timing monitoring of the proton beam. The clinical proton beams are usually pulsed with a radio-frequency in the tens of MHz region, corresponding to

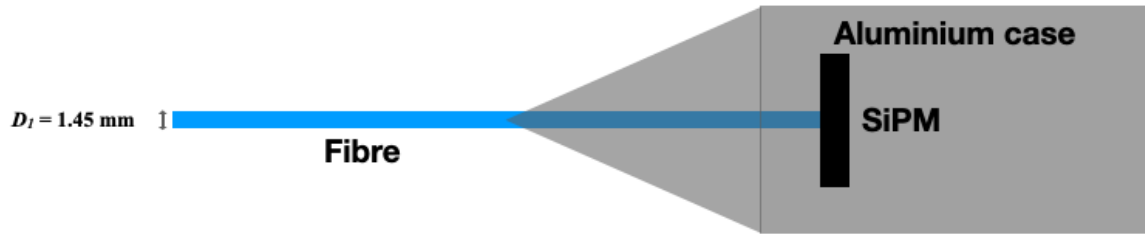


Figure. 3.6 A schematic drawing of the scintillating fibre probe.

a period between beam bunches that are in the tens of ns region, so we developed a plastic scintillator counter, referred to plastic counter in this thesis, to record the incoming timing of incident protons. The configuration of the plastic counter is shown in Fig. 3.7. A thin plastic

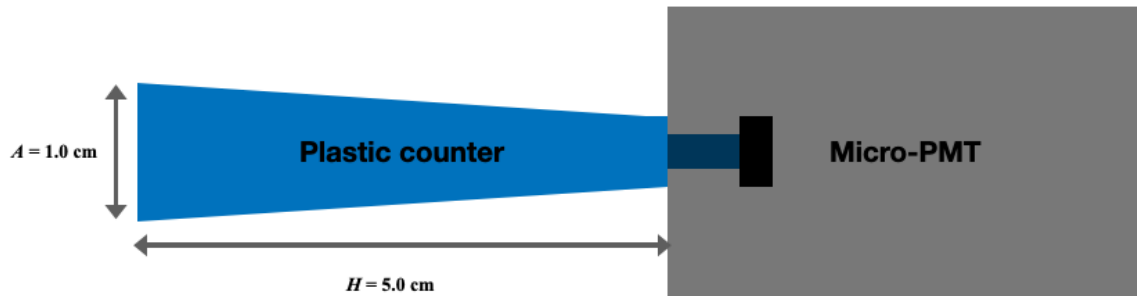


Figure. 3.7 A Schematic drawing of the plastic counter.

scintillator (1 mm thickness) was cut in the shape of trapezoid and coupled to a Micro-PMT (Hamamatsu Model H12403 , [67]) for signal readout. The trapezoid shape increases the cross section of the proton beam monitoring when the wider part of the plastic counter was placed in the beam line, while the other side of the scintillator matches the entrance window of the Micro-PMT and in this way we avoid the use of light guides which may compromise the performance. We have applied a Micro-PMT rather than a SiPM for this counter, due to the low dark current and fast response of the Micro-PMT. It is also compact (i.e. $30 \times 38 \times 15 \text{ mm}^3$) compared with a traditional PMT and the active window for accepting light is $1 \times 3 \text{ mm}^2$.

3.2 Electronics readout system, data acquisition and pulse processing

In this section, the different DAQ systems that were used in this project are introduced separately. In particular, the description starts with the more traditional analog signal processing system to the digital signal processing system, and finally the compact ASICs (i.e. application-specific integrated circuits) that were adopted for the multi-channel readout of the LYSO arrays.

3.2.1 Analog signal processing

The first setup is based on "standard" nuclear instrumentation modules (NIM) which are widely used for radiation measurements in nuclear physics experiments. It is shown in Fig. 3.8, the schematic drawing of the signal processing chain regarding the measurements of energy and count rate of the coming events. A charge sensitive module is required, known as preamplifier to convert the current pulse to a voltage step that is proportional to the total charge Q . This voltage pulse has a long tail in the time domain and is then converted to a semi-Gaussian-shape pulse via a shaping amplifier. After the shaping amplifier, the height of the semi-Gaussian pulse V_{peak} is proportional to the total charge deposited in the detector and can be digitised by the analog-to-digital converter (ADC) of a multi-channel analyser (MCA) that histograms the pulse height distribution corresponding to the energy distribution of the incident particles. In the meantime, the pulse is also sent to a timing discriminator that generates a fast trigger that sets a threshold for the event pick-up, which enables only events with a pulse height larger than the threshold to be recorded in the MCA.

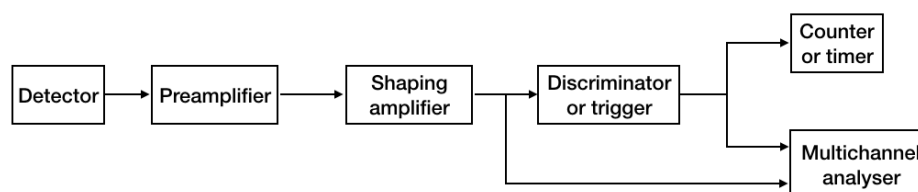


Figure. 3.8 A schematic drawing of the electronics readout chain in radiation measurements [7].

3.2.2 Digital signal processing

Modern electronics combine many parts of the signal processing chain listed in Fig. 3.8 to a compact digitiser module that samples and digitises the analogue input signal with high frequency in the hundreds of MHz region (i.e. every few ns). The digitised pulse is then processed in software rather than in hardware, which reduces the complexity and often the cost of the readout system. Fig. 3.9 shows the block diagram of a digitiser based signal processing chain for the radiation spectroscopy. The input analogue signal from the SiPMs are sent to the ADC that digitise the analog pulse into discrete samples at fixed time intervals. The samples are sent to an FPGA (field-programmable gate array) that has been programmed with DPP (digital pulse processing) algorithms (see Appendix B for details) to perform the energy and time measurements and pulse shape analysis of the digitised pulses. The coincidence algorithms are also programmed in the FPGA to enable conditional measurements between two or more channels.

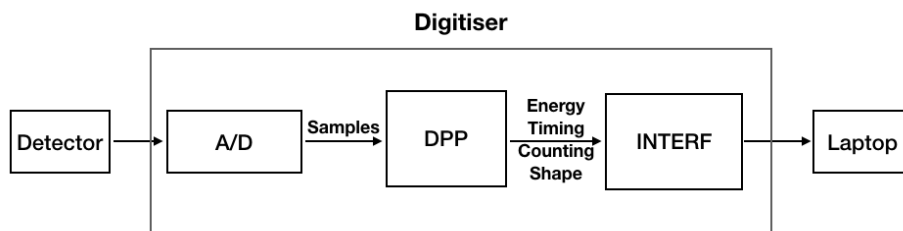


Figure. 3.9 A schematic drawing of the signal processing chain with a digitiser [9].

The digitiser (DT5730 CAEN, [9]) that was used in this project can support two types of DPP based algorithms, including DPP-PSD (pulse shape discrimination) and DPP-PHA (pulse height analysis). The DPP-PHA offers the trapezoid method to calculate the total energy of the input pulse with a resolution of about 16k channels (i.e. 14 bit ADC resolution). This algorithm is optimised for the gamma-ray energy spectroscopy using long-tail pulses that are following a charge sensitive preamplifier stage in semiconductor detectors. However, in this project, the signals from the dual-mode (neutron/gamma-ray sensitive) scintillator detector (CLLB) were processed using the DPP-PSD algorithm that allows for neutron/gamma-ray discrimination. As illustrated in Appendix A, the CLLB crystal has two different decay times, fast decay(180 ns) and slow decay (1080 ns). The fractions of fast decay and slow decay are different for gamma-rays (i.e. 61 % fast decay and 39 % slow decay) and neutrons (i.e. 50 % fast decay and 50 % slow decay), resulting in different pulse shapes, as shown in Fig. 3.10. This results in the decay tail of neutrons being longer than that of gamma-rays.

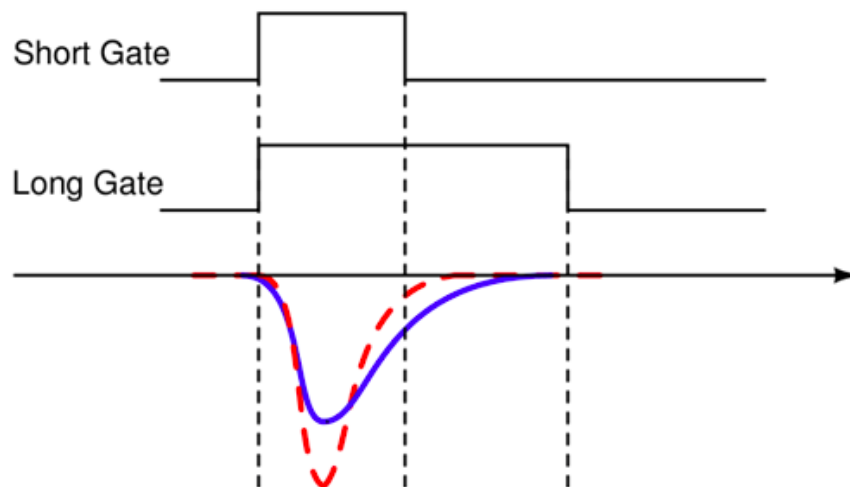


Figure. 3.10 The pulse shape discrimination of a neutron (blue solid line) and a gamma-ray (red dash line) signal [9].

In contrast to the DPP-PHA algorithm, the DPP-PSD is based on the charge accumulation on different time regions of the input pulses, rather than trapezoid method in PHA which is optimised for the total energy spectroscopy using preamplified signals. In the following, we briefly introduce the principle of DPP-PSD firmware as it is implemented in the digitiser module DT5730. As shown in Fig. 3.11, the input signal (digitised) is split into two branches for time pick up and charge accumulation respectively. A discriminator is applied for the time pick-up method, including a leading edge discrimination (LED) or a constant fraction discrimination (CFD) that can be selected. To avoid the time jitters presented in the LED method for pulses with different amplitudes, we chose the CFD method as our time pick up method. A threshold is applied to the discriminator to select events with amplitude higher than the applied threshold. In parallel, in the energy branch, we can set a short and a long gate on the time scale for charge integration of pulses as shown in Fig. 3.10. These different integration regions enable PSD. Finally, the charge integration value and the time stamp of an event is output for data storage and further processing in a PC. The DPP-PSD can provide both online and offline data analysis and the data can be saved in different formats, such as ROOT [68] that was chosen in our measurements.

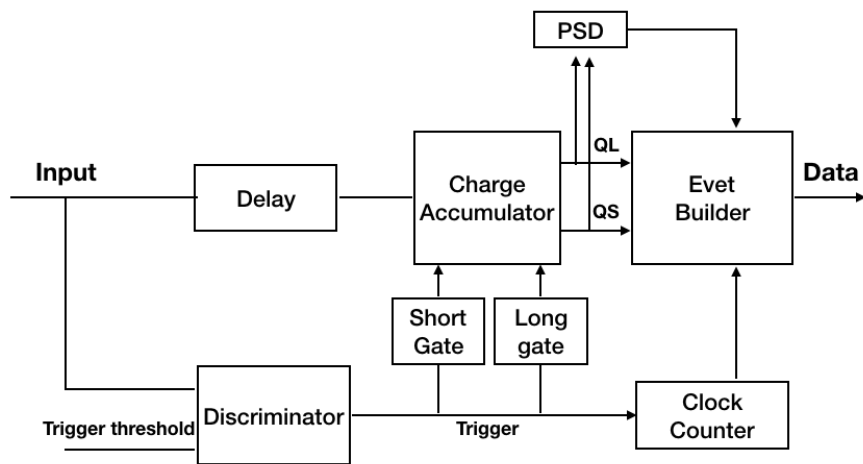


Figure. 3.11 The functional block diagram of DPP-PSD in DT5730 [9].

3.2.3 ASICs for multi-channel readout

The digitiser module can provide digitised signal of pulses and all functionalities needed in radiation detection. It compresses all analog electronics modules into one single device and can support multi-channel readout (e.g. 8 channels for DT5730), a high count rate and PSD. However, as the number of signal channels increases to several hundreds, it is not possible to provide the energy and timing information of multi-channel detectors (e.g. 128 LYSO crystals in this project) with the DT5730 module. For this high-density multi-channel readout, we used the PETsys TOFPET2 ASIC evaluation kit [69]. This readout product is commercially available and was developed for time-of-flight (ToF) PET for diagnostic medical imaging, which supports the coincidence timing measurements of positron emitters in PET scanning. It is designed in standard CMOS technology and has an extendable number of input channels. The fast timing pick-up and flexible input channels met our requirements for the electronics readout of the PGI prototype.

In this subsection, we are going to introduce the hardware of the ASIC evaluation kit and how it works for multi-channel readout in PGI application, while the electronics design of ASICs circuit is beyond the scope of this thesis (see Appendix B for more details about the system diagram). Fig. 3.12 shows a photograph of the ASIC evaluation kit with an experiment setup for coincidence measurements. Specifically, the detectors connected to the ASICs were placed in a cooling box to ensure the stability of temperature, as shown in Fig. 3.13. Then, the signal from ASICs were transmitted to the Mother Board which corresponds to the board on the bottom in Fig. 3.12. The middle board is named as Mezzanine and its function is to supply the voltage of the SiPMs. The digitized data were extracted and recorded in the laptop via the interface board (i.e. top one) which is a Gigabit Ethernet mezzanine providing the access and control of the evaluation kit over the Ethernet port. There also is a cooling system (i.e. a black box with two fans installed inside and outside the box) includes the ASICs and LYSO detectors to keep the SiPMs and ASICs in a stable temperature for data reproducibility.

The ASICs evaluation kit needs to be calibrated before the first measurement, which includes the calibration of discrimination, TDC and QDC using the recommended ASIC threshold settings. The data acquisition and processing were controlled by a graphical user-interface. The results of LYSO detector tests using the ASICs tool kit is illustrated in section 3.3.1.

So far, we have introduced the PG detector prototype, which includes a collimated CLLB detector for the high-resolution spectroscopy, a number of LYSO detector arrays for the 1D PG intensity profile, a scintillating fibre-based probe for the energy and timing measurements of proton beams and a plastic counter to monitor the beam structure of the



Figure. 3.12 The ASICs setup connected with the SiPMs of two small LYSO detectors for coincidence measurements.

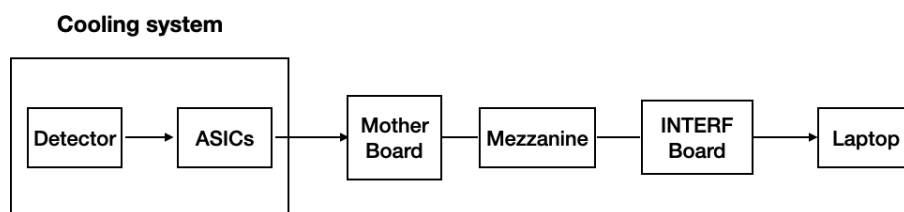


Figure. 3.13 A schematic drawing of the ASICs tool kit for radiation detection.

incoming protons. We have also covered the electronics DAQ system for the signal processing of those scintillator based detectors. All the detectors have been tested initially in our nuclear application laboratory using the presented DAQ systems. In the following section, we show some of the important results that characterised those detectors regarding their energy and/or timing resolution.

3.3 Characterisation of scintillating detectors

3.3.1 Energy resolution of CLLB and LYSO detection systems

Firstly, we calibrated the CLLB with two commonly used radioactive sources, ^{137}Cs with a gamma-ray line at 662 keV and ^{152}Eu using the 344, 779, 964, 1117 and 1408 keV gamma-ray lines. The experimental setup is shown in Fig. 3.14 and includes a digitiser and laptop for data acquisition. The collected pulses were processed offline rather than using the online DPP algorithms.

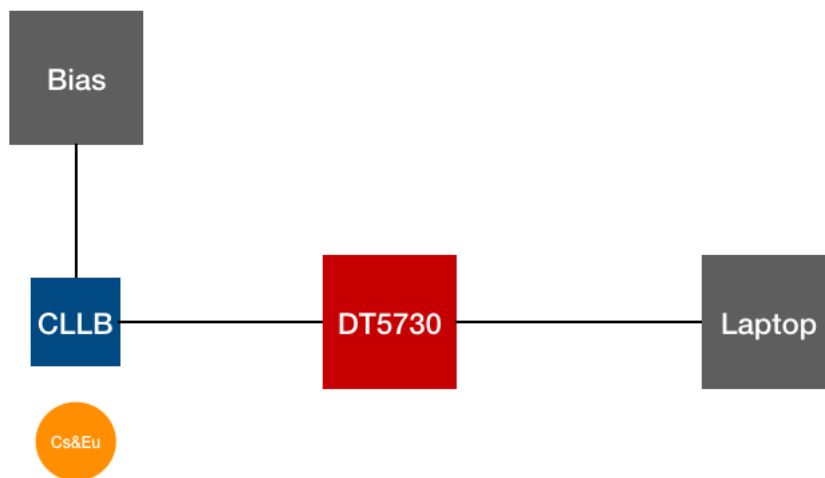


Figure. 3.14 The experimental setup for the energy spectroscopy of two gamma-ray sources (^{137}Cs and ^{152}Eu) detected by the CLLB detector.

The uncalibrated energy spectrum of ^{137}Cs and ^{152}Eu is illustrated in Fig. 3.15 of which the highest intensity peak is the 662 keV from ^{137}Cs . The peak follows a Gaussian distribution and is fitted with a Gaussian function, as shown in Fig. 3.15. Similarly, gamma-ray peaks from ^{152}Eu were also fitted using the same algorithm to obtain the corresponding centroids, plotting centroid channel versus energy as the calibration function. In Fig. 3.16, we fitted

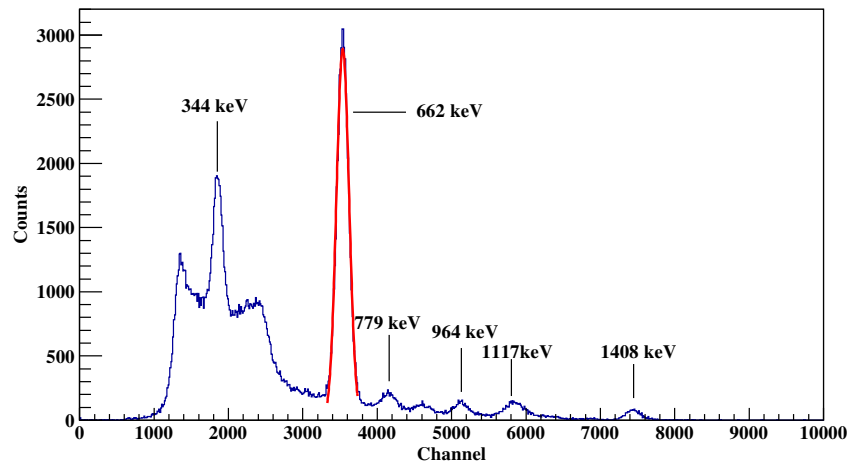


Figure. 3.15 The uncalibrated energy spectrum of ^{137}Cs and ^{152}Eu in the CLLB detector. The energy peak at 662 keV was fitted with a Gaussian function.

the six calibration points with a linear function giving the relationship between energy and channel by Eq. 3.4:

$$\text{Channel} = 5.25 \times \text{Energy} + 58.92 \quad (3.4)$$

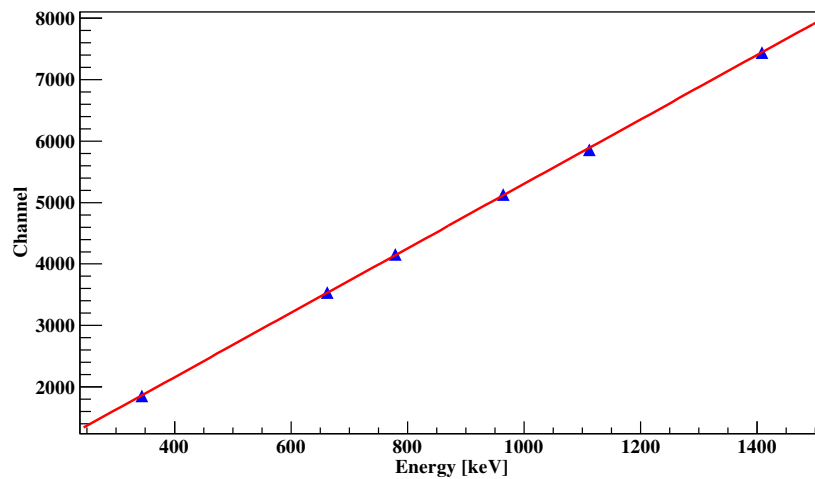


Figure. 3.16 The fitted linear function of channel energy for the calibration of the CLLB detector.

The above function (Eq. 3.4) was used to calibrate the histogram displayed in Fig. 3.15, resulting in the calibrated gamma-ray energy spectrum shown in Fig. 3.17. Thus, the energy resolution of the CLLB at 662 keV can be calculated by Eq. 3.5, where FWHM equals to $\sigma \times 2.355$, which is around $(5.12 \pm 0.03) \%$. The results is slightly worse than the previous tests with around 4 %, since PSD is not perfect to measure the energy spectroscopy compared with PHA.

$$\text{Energy resolution} = \frac{\text{FWHM}}{\text{centroid}} \times 100\% \quad (3.5)$$

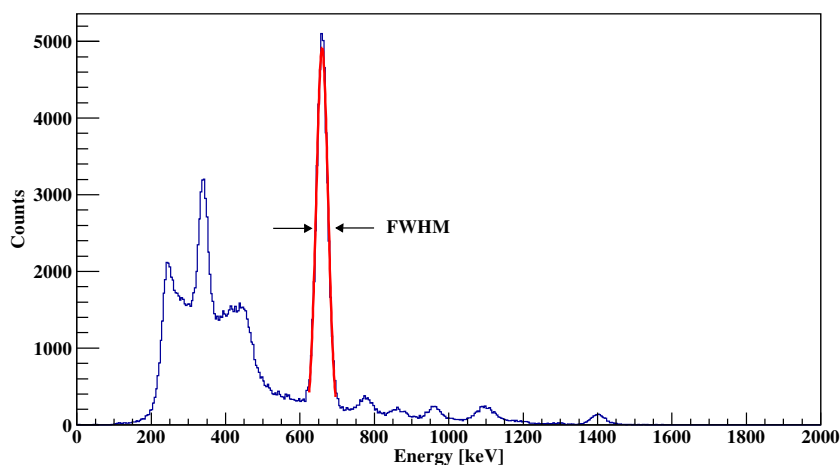


Figure. 3.17 The calibrated energy spectrum measured by the CLLB detector.

The LYSO detector arrays were also tested with the ASICs for gamma-ray spectroscopy of ^{137}Cs and ^{22}Na (^{22}Na was not used for the calibration of CLLB detector), see Fig. 3.18. Data from a total of 128 channels were recorded in the QDC mode and then processed via the DAQ software that converts the binary data to ROOT file. In the QDC mode, the total charge of a pulse was integrated in timescale, which was recorded as energy in the ROOT file. The plotted energy (charge) spectrum is shown in Fig. 3.19 with three distinct peaks at 511, 662 and 1275 keV. It is important to point out that the LYSO crystal is a Lutetium based scintillator with a naturally occurring radioisotope ^{176}Lu that decays into three gamma lines at 88, 202 and 307 keV. The gamma-ray events at low charge range in Fig. 3.19 are from ^{176}Lu decays (i.e. the first tiny peak is the 202 keV gamma line and the 307 keV peak is mixed with the Compton edge of the 511 keV peak).

Similarly, the calibrated function of LYSO can be extracted from the histogram displayed in Fig. 3.19 with only three gamma lines, from ^{22}Na and ^{137}Cs , as labelled in the figure. The

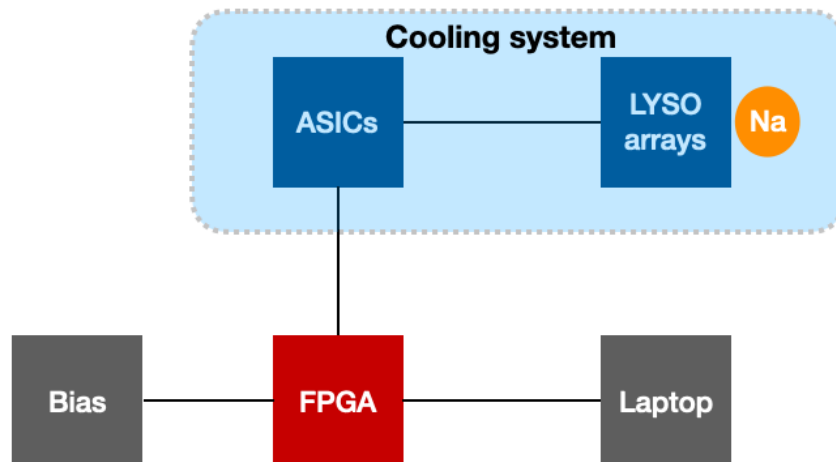


Figure. 3.18 The experimental setup for the energy measurement of a point gamma-ray source ^{22}Na and ^{137}Cs detected by the LYSO detectors.

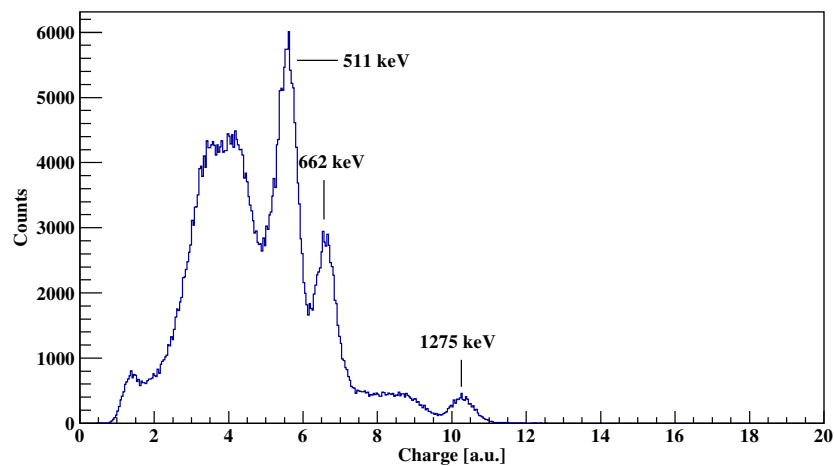


Figure. 3.19 The uncalibrated energy spectrum of ^{22}Na and ^{137}Cs measured by the LYSO detector arrays at channel 122 (arbitrary channel).

energy calibration curve plotted is non-linear at 1275 keV, assuming it is linear at low energy range. In contrast to the CLLB which has a large surface covered with many SiPMs for light collection, a single LYSO crystal has a light-readout area of $3.2 \times 3.2 \text{ mm}^2$ (front face) coupled with an SiPM of the same size. The microcell size in each SiPM is $25 \mu\text{m}^2$, resulting in a total of 14336 microcells in the SiPM's active area. As mentioned in section 2.3.2, each

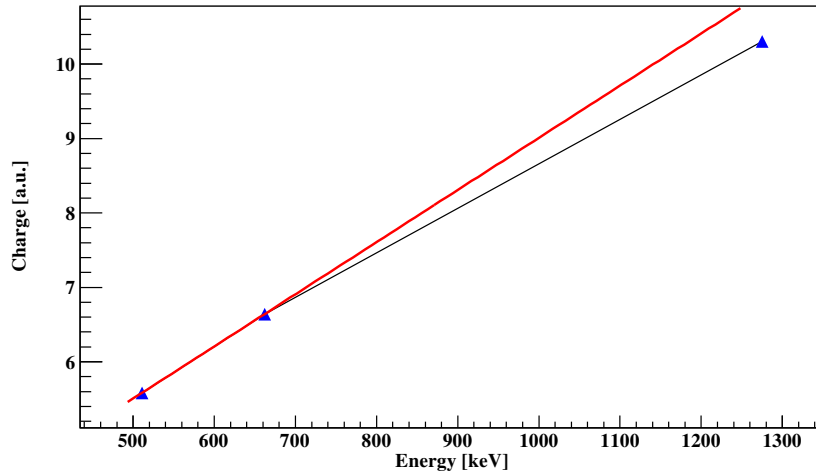


Figure. 3.20 The calibration curve of energy versus charge for the LYSO detector at channel 122. The effect of non-linearity is already evident at 1275 KeV.

microcell can only be fired by a single photon and remains inactive (dead) for a time period of about 100 ns. The light output of LYSO crystal is 29000 photons per MeV gamma-ray. Thus, the total light output is around 36975 photons at 1275 keV. Considering the QE (40 %) of the SiPM, the number of photons that can be detected by the SiPM (around 14790) is comparable the total microcells in the active area (14336), so the probability to hit a "dead" microcell is high and the SiPM gets saturated significantly at 1275 keV, causing non-linearity at high energy gamma-ray range ($>1000 \text{ keV}$).

It is also possible to calibrate the LYSO detector roughly with a linear function, while the energy resolution was reduced (i.e. around 12.7 % at 662 keV), as displayed in Fig. 3.21). The non-linearity of the SiPM saturation at high energy region is not a problem in our experiment, since we do not expect high-resolution energy spectroscopy from the LYSO detector.

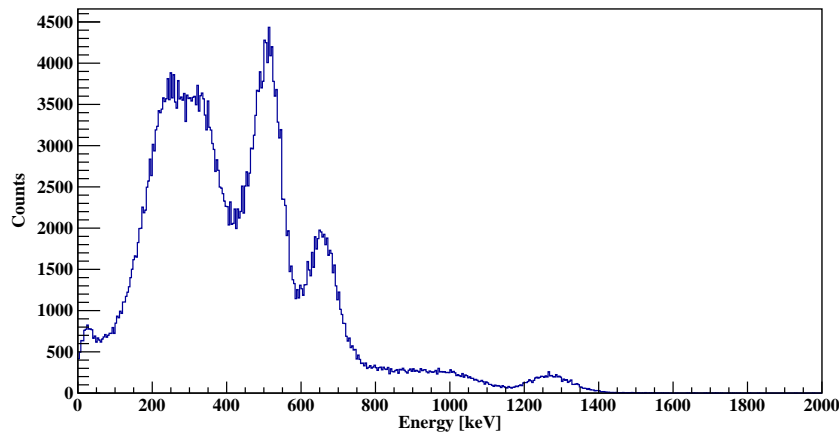


Figure. 3.21 The calibrated energy spectrum of ^{22}Na and ^{137}Cs measured in the LYSO detector arrays at channel 122 (arbitrary channel).

3.3.2 The coincidence timing resolution between the CLLB and LYSO detector

The timing response is also one of the most significant properties of scintillator detector for the PGI application. The organic scintillators usually have a much shorter decay time than the inorganic scintillators due to the different fluorescence processes in the material. However, some inorganic crystals also possess fast decay time, such as LYSO (42 ns), LaBr_3 (25 ns) and BaF_2 (0.87 ns for fast decay), while the CLLB crystal has a decay time of 180 ns for gamma-rays. Not only the crystal itself but also the electronics affect the timing response of a detector system.

We tested the coincidence timing resolution of the CLLB and LYSO detectors, as shown in Fig. 3.22. A ^{22}Na radioisotope source was placed in the middle of the CLLB and LYSO detector (i.e. signal from one crystal was extracted), generating two coincidence 511 keV photons emitted back to back detected by the two detectors that were placed head to head. Then, signals from those two detectors were connected to channel 0 and 1 in the digitiser operating in DPP mode and with a coincidence timing window of 90 ns between the channels.

Fig. 3.23 shows the energy spectra from those two detectors for coincidence gamma-rays detected within the 90 ns timing window. There are two peaks in the graph, representing the coincidence 511 keV photons detected in the CLLB and LYSO detector. To obtain the coincidence timing distribution, the timing differences of each pair of correlated hits are considered, which gives the left histogram in Fig. 3.24. The random events can be further rejected by applying an energy window around the 511 keV peaks to select only full energy events in Fig. 3.23. Finally, the improved timing distribution with only true coincidence

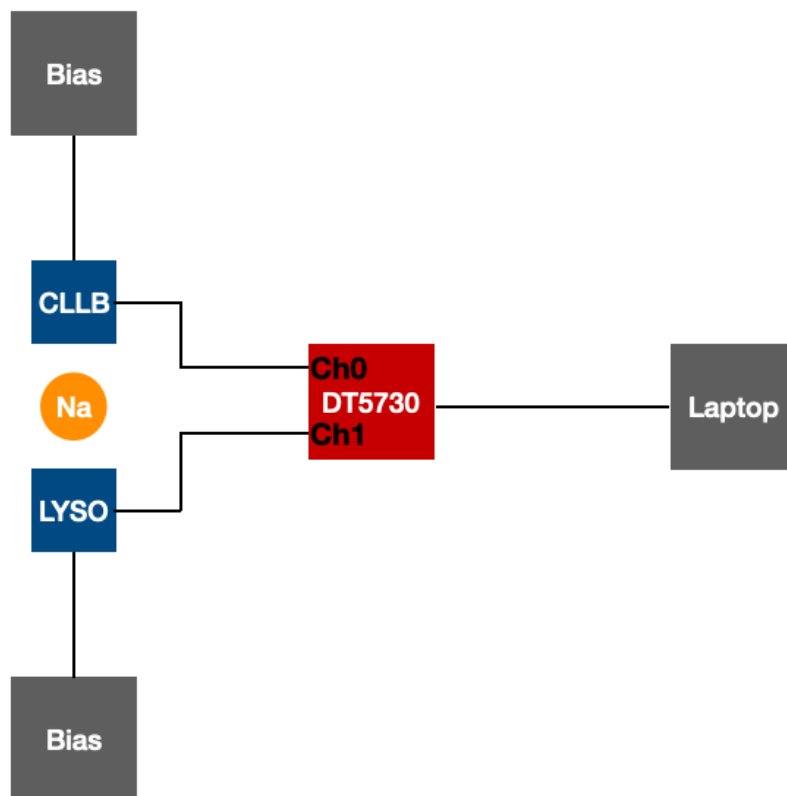


Figure. 3.22 The coincidence timing resolution measurements of the CLLB and LYSO detector.

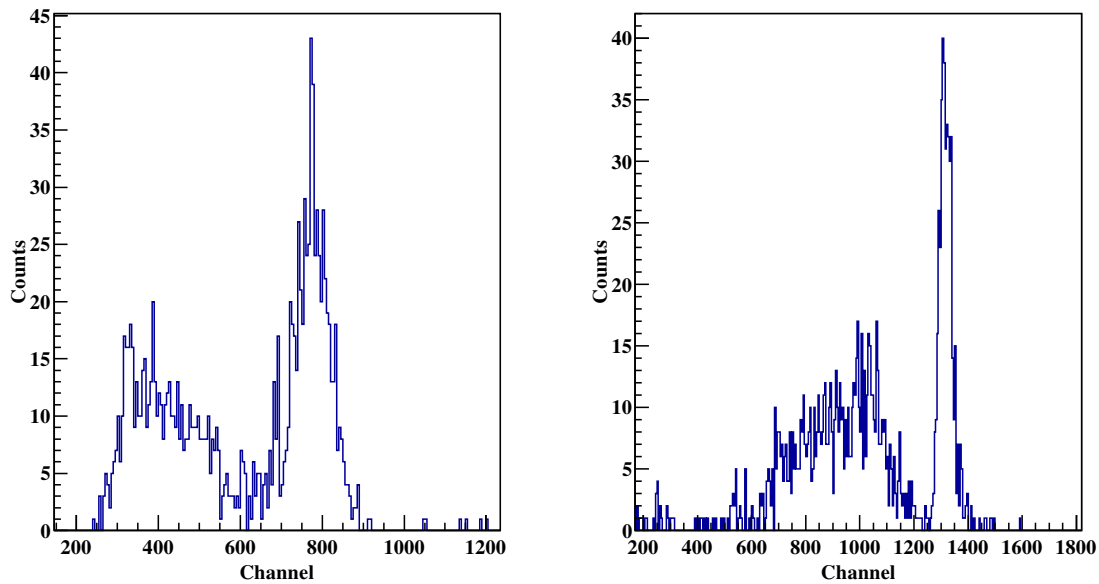


Figure. 3.23 The energy spectra from LYSO (left) and CLLB (right) detector, recorded in a coincidence timing window of 90 ns for 511 keV photons (i.e. peaks in the graph).

events that is displayed on the right histogram of Fig. 3.24. The coincidence resolving time was estimated with a Gaussian fitted peak, giving a FWHM time resolution of (4.9 ± 0.1) ns. The statistics are low due to the small cross section of the LYSO crystal (3.2×3.2 mm²).

3.3.3 Energy measurements of fibre and plastic counter

The organic scintillators were also tested using the digitiser operating in DPP-PSD mode for the energy measurement of an electron source (⁹⁰Sr) and a gamma-ray source (²²Na), as illustrated in Fig. 3.25 for the experimental setup. This material is usually applied in nuclear physics experiments for charged particle detection.

The small SiPM (1×1 mm²) coupled to the fibre probe generates a discrete output when illuminated with low-level light (i.e. low number of photons), such as scintillating light generated from the fibre. The photoelectron spectrum from the SiPM itself is shown in Fig. 3.26, recorded from the dark counts of the SiPM and background radiation. These peaks indicate the single-photon detection, i.e. the first peak corresponds to the detection of a single photon. The ⁹⁰Sr energy spectrum was also plotted in the same graph (Fig. 3.26, top). The real energy spectrum was obtained from the subtraction of those two histograms, plotting on the bottom graph in Fig. 3.26. Similarly, the spectra of ²²Na is illustrated in Fig. 3.27, in which case the statistics are low due to the small size of the probe and the small cross section

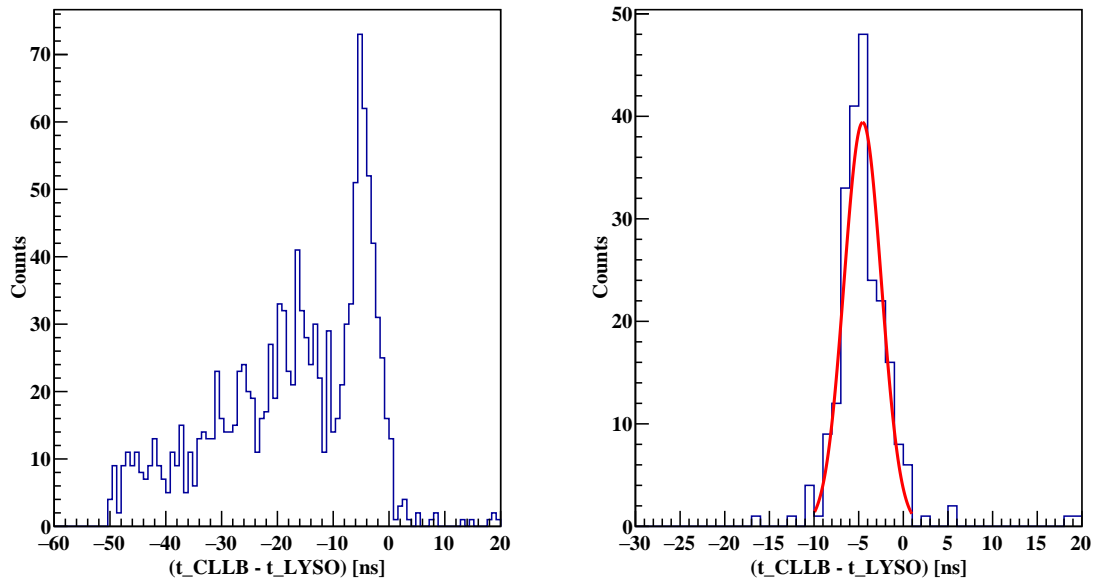


Figure. 3.24 The time difference distribution of the CLLB and LYSO detector (left). The improved distribution after applying an energy cut on the 511 keV peak for both detectors (right).

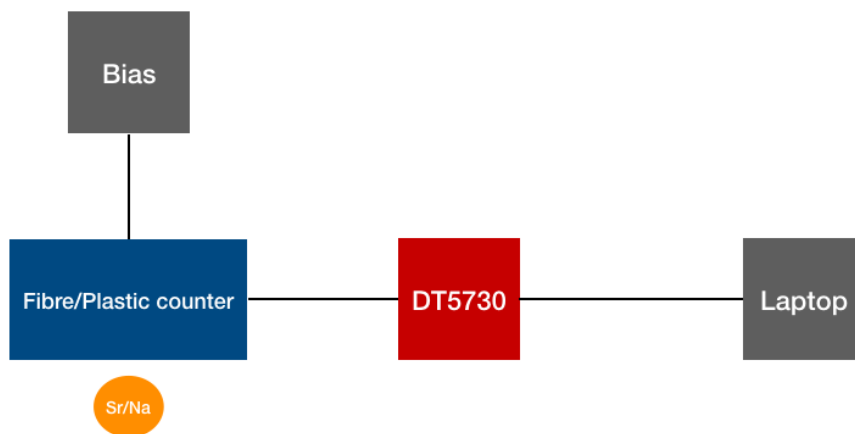


Figure. 3.25 The experimental setup for the energy response of a fibre probe and plastic counter.

of gamma interaction in the probe. The gamma-ray spectrum is a reference for us, since we would like to use the probe for proton energy deposition in a water phantom.

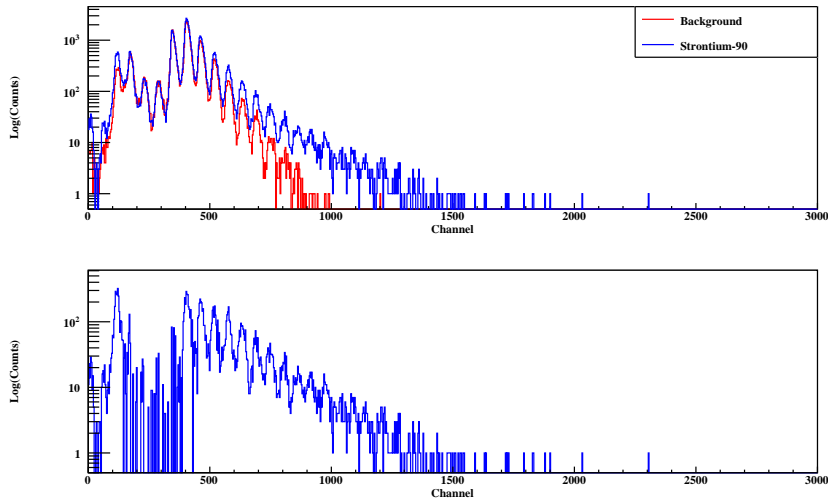


Figure. 3.26 The energy spectra of ^{90}Sr with SiPM dark count (noise) in the fibre probe (top). The real energy histogram corresponding to ^{90}Sr once the background spectrum is subtracted (bottom).

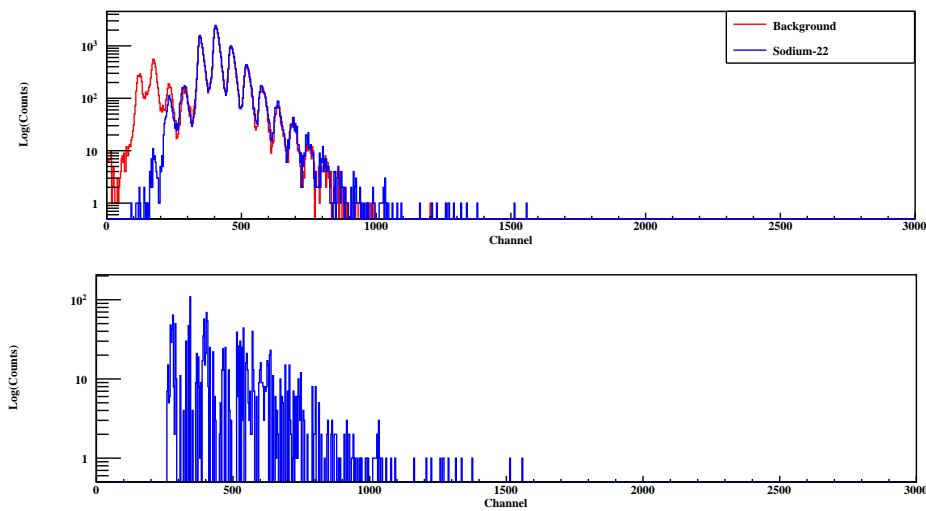


Figure. 3.27 The energy spectra of ^{22}Na with SiPM dark count (noise) in the fibre probe (top). The real energy histogram corresponding to ^{22}Na once the background spectrum is subtracted (bottom). The thresholds for both cases were slightly different.

The micro-PMT coupled to the plastic counter will not generate discrete output down to single photon level and the background noise from the PMT is negligible. Fig. 3.28

represents the energy spectra from a ^{90}Sr and ^{22}Na source that were plotted in the same graph for comparison. The plastic counter has a larger size allowing a higher detection efficiency, so the statistics in the spectra are much higher than that in the fibre probe. The statistics of the electron spectrum in Fig. 3.28 are also much higher than that of the gamma sources, which is consistent with the results we observed in the fibre probe. As mentioned in section 3.1.4, the plastic counter was designed to record the arrival time of the proton beam in the experiment. This simple test using an electron source indicates the plastic counter reacts well for charged particles in terms of energy and timing information.

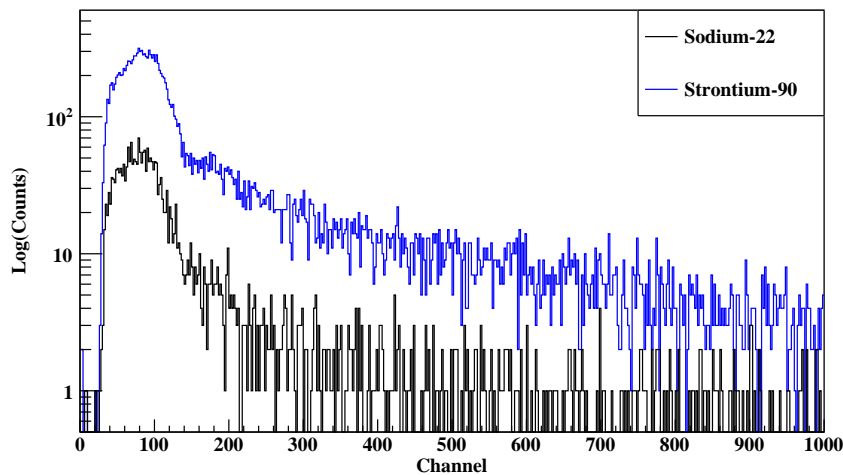


Figure. 3.28 The energy spectra of ^{22}Na (in black) and ^{90}Sr (in blue) in the plastic counter.

3.4 Summary

The configuration of the PGI detector developed and used in this project was described in detail. Namely, a monolithic CLLB detector for the PG energy spectroscopy, an array of LYSO crystals for the 1D PG intensity distribution along with the target and a fibre probe for the energy and timing of proton beams hitting a water phantom. Also, we assembled a dedicated plastic counter for the timing measurements of incident protons. The different electronic readout chains and DAQ systems were also presented.

Finally, the results of detector response to low-energy gamma-rays and electrons were presented. The energy resolution of the CLLB is around 5.1 % and that for one of the LYSO pixels is around 12.7 % at 662 keV. The linearity of energy response in the CLLB is much better than that in the LYSO, due to the smaller saturation of the SiPMs. The non-linearity in LYSO becomes obvious at 1275 keV. The coincidence timing resolution between the

CLLB and a pixel of LYSO is around 4.9 ns (FWHM). Finally, the energy spectra of ^{22}Na (i.e. gamma-ray source) and ^{90}Sr (i.e. electron source) measured in both the fibre probe and plastic counter show similar properties, apart from the background noise recorded in the fibre (i.e. dark noise from SiPMs) is much higher than that in the plastic counter (i.e. low noise from micro-PMT).

Chapter 4

Monte Carlo Geant4 simulation

MC simulation is a critical toolkit in particle and nuclear-related physics, which is powerful, flexible and has also been applied widely in medical physics [70]. In this project, the MC Geant4 simulation [71] (version 10.5.p00) was applied to study the properties of secondaries generated in a proton-irradiated phantom regarding the particle energy, timing, angular momentum and statistics etc. Dedicated simulation codes were used to study the range uncertainties estimated from novel PG methods, such as PGI, PGS and PGT via a perfect ‘ring’ detector in the simulation so that the minimum range error can be deduced for each of those methods. Finally, the realistic detector responses of our PGI prototype were examined, including the PG energy in the CLLB, the 1D PG intensity profile in the LYSO arrays and the energy and timing of proton beams in the fibre probe. In this chapter, we present the results that were obtained from the Geant4 simulations for the different detector configurations.

4.1 Secondaries produced in a proton-irradiated phantom

Understanding the secondaries produced in a proton-irradiated phantom is essential to design the PG detector prototype. In this section, the results from a simple cylindrical phantom irradiated with proton beams at different energies to rigorously study the properties of emitted secondaries (i.e. PGs, neutrons and secondary protons) are presented.

4.1.1 Methods

As shown in Fig. 4.1, a cylindrical water phantom with a size of 5 cm in diameter and 30 cm in length, was implemented as the sensitive volume. The properties of proton beams are chosen to be comparable with those applied in clinical PT, with a beam energy spread of 0.2 % ($E_{\sigma}/E = 0.2\%$, sigma of Gaussian distribution). The starting position of the beam is

considered at 6 cm upstream from the front face of the phantom. The physics lists included in the simulation were QGSP-BIC-HP [72], Emstandard-opt4 [73] and Radioactive Decay, as suggested by other authors [74–76].

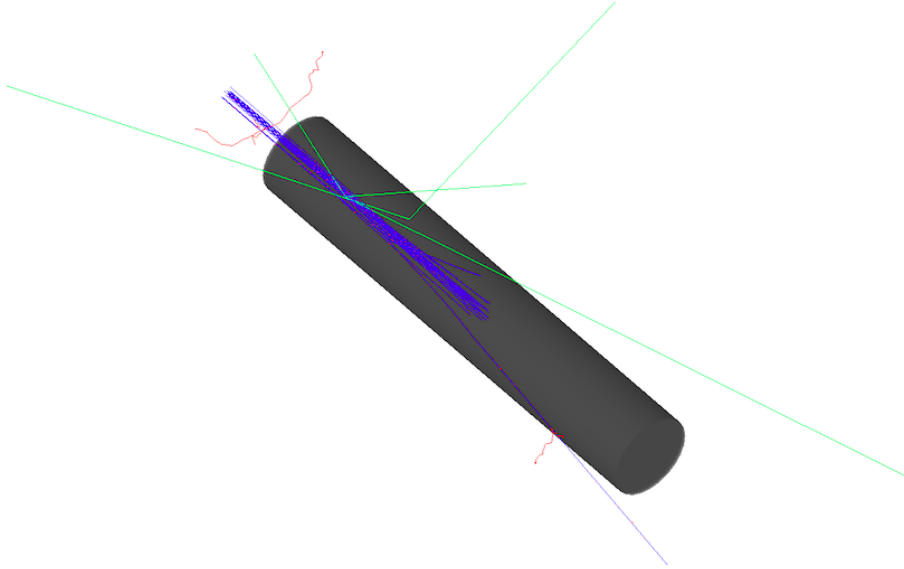


Figure. 4.1 The cylindrical phantom implemented in Geant4 simulation to study the effect of secondary radiation.

The package QGSP-BIC-HP involves the binary light-ion cascade model which was applied for the hadronic processes in the simulation. In the meantime, the radioactive decay model was activated to model the de-excitation of produced excited nuclei and the standard electromagnetic model Emstandard-opt4 was applied for the EM interactions of related particles and in particular to account for the precise treatment of gamma-ray interactions with matter (i.e. include the Doppler broadening due to Compton scattering from atomic electrons). For simplicity, the scintillator detectors incorporated into the Geant4 simulation was considered as perfect in terms of energy and timing resolution (optical processes were not considered).

4.1.2 Range and secondary radiation

The pristine BPs based on the Geant4 simulation are plotted in Fig. 4.2, displaying the dose-depth curves for various proton beam energies ranging from 38 to 200 MeV in a water phantom. The number of incident protons for each run is the same, 10^6 . With the increase of incident proton energy, both the surface and BP dose decrease. Moreover, BP is sharper when the incident beam energy is lower, and it gets broader for higher energies due to the increase of energy straggling.

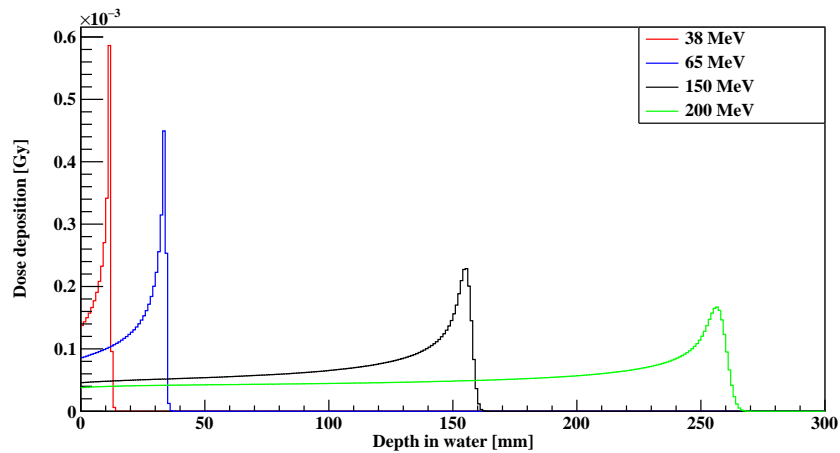


Figure. 4.2 A GEANT4 simulation of the Bragg curves for different proton beams at various energies ranging from 38 to 200 MeV in a water phantom as calculated by the simulation.

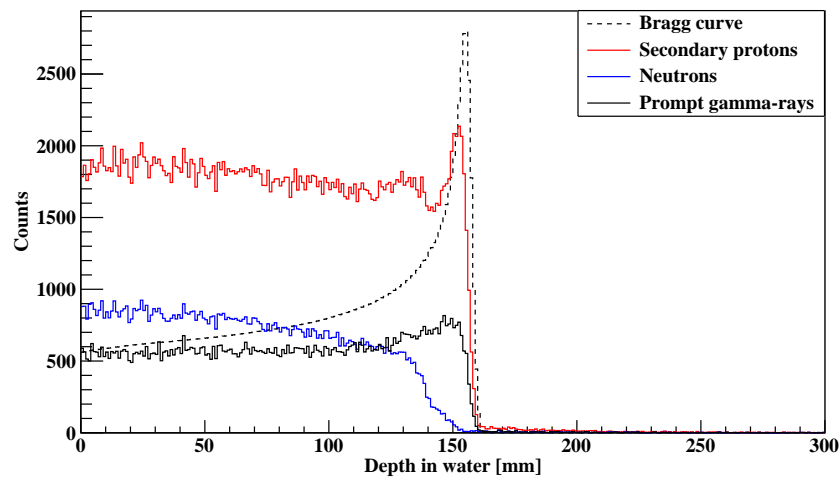


Figure. 4.3 A GEANT4 simulation of the statistics of secondary particles (i.e. neutrons, secondary protons and PGs) along the depth in a water phantom irradiated with a proton beam at 150 MeV (the dash line indicates the BP).

As the incident proton beams slow down in the phantom, secondary radiations were generated along the beam path instantly. Those secondary radiations consist of neutrons, PGs, scattered protons, electrons, positrons and other ions, among which we are particularly interested in neutrons and PGs since they are highly penetrating. Fig. 4.3 shows the statistics of secondaries along the depth in a water phantom. The dash line represents the BP (scaled) and those three solid lines indicate the profile of secondary protons, neutrons and PGs respectively. The production of neutrons decreases with the slowing down of incident beams and it drops considerably near the BP region. In contrast, the yield of secondary protons and PGs follow the trend of the Bragg curve that has a boost near the BP, then suddenly goes down where the incident protons stop. This can be explained by the increase of cross section of nuclear-induced reactions as the incident beam slows down, giving the maximum value at around 20 MeV which is approaching the fall-off region. It is also noted that the emission of neutrons is higher than that of the PGs for most of the range besides the BP region. These fast neutrons penetrate the phantoms and introduce substantial background noise in the detection of useful signals (i.e. PGs).

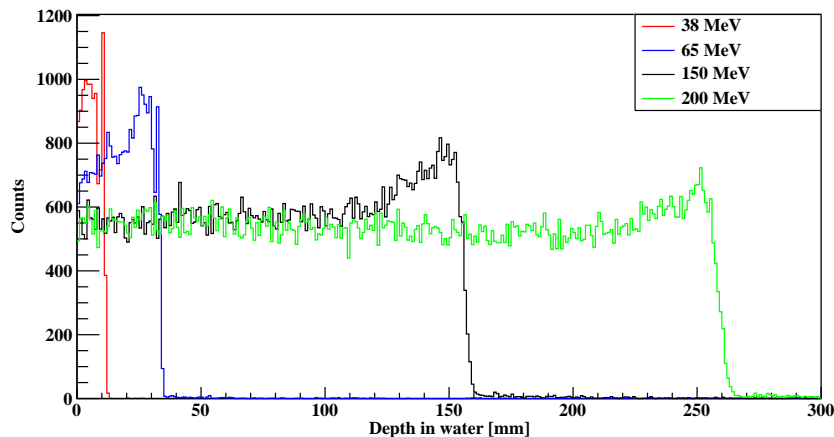


Figure. 4.4 A GEANT4 simulation of the statistics of PGs generated along the depth in a water phantom irradiated with proton beams at various energies ranging from 38 to 200 MeV.

In particular, the emission of PGs and neutrons emitted at different depths along the proton trajectory for various beam energies is summarised in Fig. 4.4 and Fig. 4.5, respectively. First, the PG yield at the surface region of the phantom has a maximum at 38 MeV, which is about 35 % higher than that from high energy proton beams such as at 150 and 200 MeV. The higher PG production at low beam energy is related to the nuclear cross section. In contrary, the production of neutrons is lowest at 38 MeV, and it increases with the incident beam

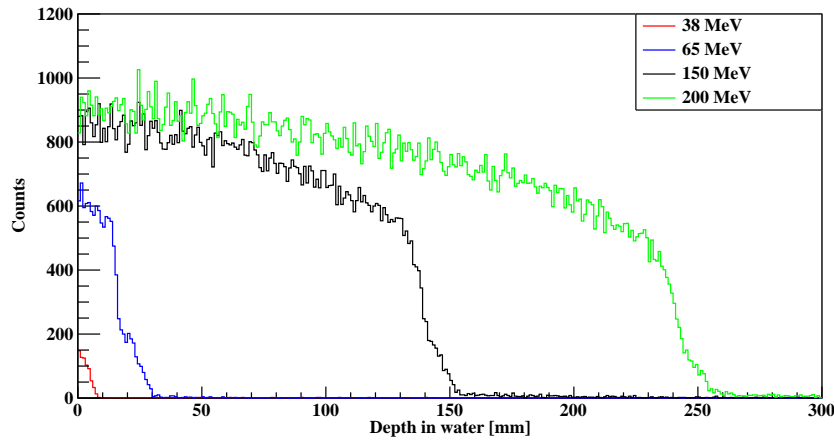


Figure. 4.5 A GEANT4 simulation of the statistics of neutrons generated along the depth in a water phantom irradiated with proton beams at various energies ranging from 38 to 200 MeV.

energy across the water phantom. Thus, the production of PGs and neutrons is correlated to the cross section of nuclear interactions.

4.1.3 Properties of secondary radiation

The properties of secondary radiation are studied in this section, including the particle energy, time and angular momentum. First, the energy distributions of those secondaries are presented in Fig. 4.6, where there are prominent gamma lines ranging from 0 to 10 MeV. However, the distribution of neutrons and secondary protons are ranging from 0 to the energy of incident beams without specific peaks.

In addition, the angular distributions versus energy of secondary radiations are plotted in Fig. 4.7 with PGs shown on the left, neutrons in the middle and secondary protons on the right. The negative and positive values of $\cos(\theta)$ refer to the emitted direction of the secondaries with respect to the incident beam direction, giving positive values as forward and negative values as backward direction. It is evident that there are more neutrons and secondary protons produced in the phantom travelling in the forward direction (i.e. incident beam direction), especially for high energy particles, since these emitters carry a part of the momentum from the incident protons when they were just created inside the phantom. Furthermore, the 1D angular distribution of PGs is displayed in Fig. 4.8, indicating more PGs are travelling in the forward direction. Verburg *et al* [6] point out that PGs emission generally is not isotropic and various angular dependence are possible depending on the quantum properties of excited nuclear level. They also suggest that each gamma line has a different double differential cross section, which also depends on the proton energy and

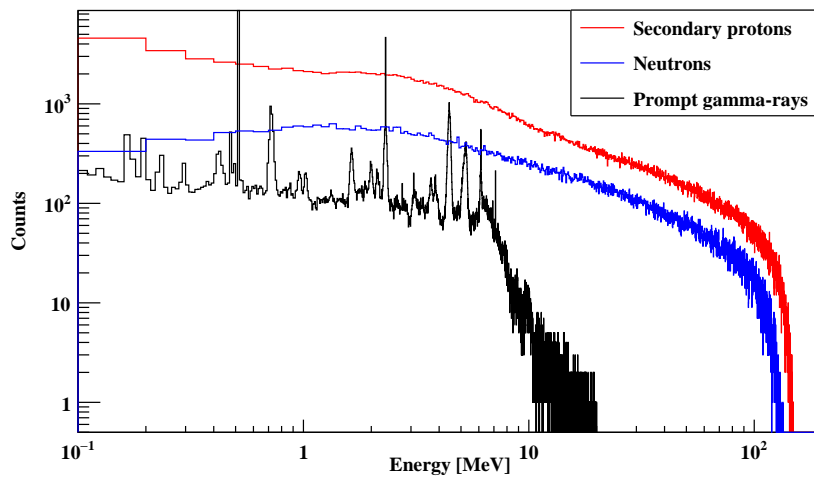


Figure. 4.6 A GEANT4 simulation of the energy spectra of various secondaries produced in a water phantom irradiated with proton beams at 150 MeV.

the Doppler broadening due to nuclear reaction kinematics is a factor that is specific to each nuclear reaction. Here, we have plotted the angular distribution of PG emission with energy higher than 1 MeV and we only notice more PGs travel in the forward direction.

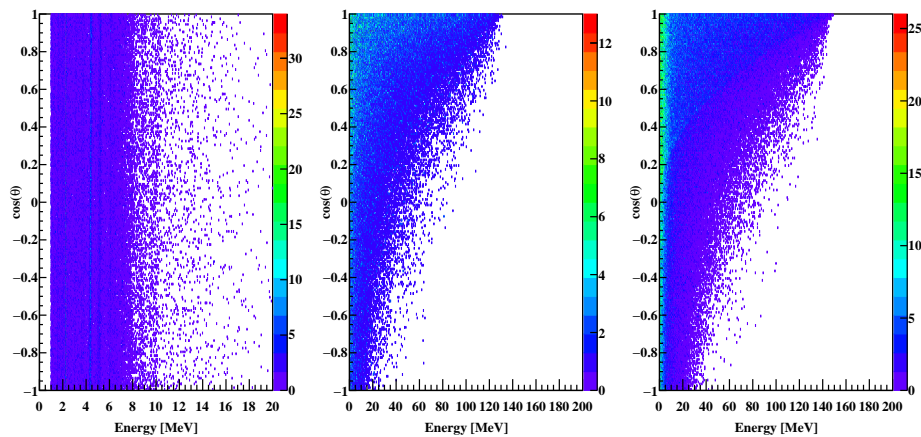


Figure. 4.7 A GEANT4 simulation of the angular distribution versus energy for various secondaries (PG on the left, neutron in the centre and secondary protons on the right) produced in a water phantom irradiated with a proton beam energy of 150 MeV.

The starting point of the timing distributions of PGs depends on the initial beam energy (i.e. the velocity of the beam), requiring longer time to reach the surface of the phantom at lower beam energy (see Fig. 4.9). The width of the timing distributions is also related to the beam energy, which means it takes longer for the high energy protons to stop. Fig. 4.9 shows

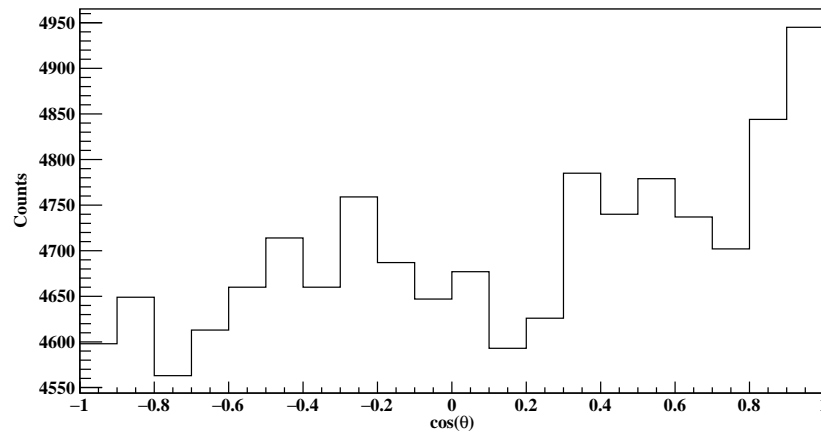


Figure. 4.8 A GEANT4 simulation of the angular distribution of PGs produced in a water phantom irradiated with a proton beam energy of 150 MeV. There is a slight preference for gamma-ray emission in the forward direction (y-axis is zoomed in).

timing spectra of PGs from various energies ranging from 38 to 200 MeV when the starting time $t = 0$ is considered 6 cm before the beginning of the phantom entrance window. When examining the timing spectrum of the 65 MeV proton beam in detail, one can notice a small peak near the end of the distribution in Fig. 4.10 (see dashed line).

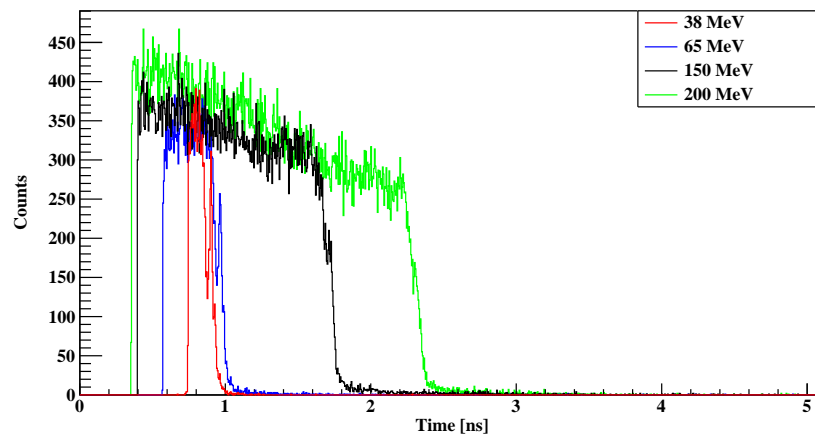


Figure. 4.9 A GEANT4 simulation of the timing spectra of PGs produced in a water phantom irradiated with proton beams at various proton beam energies ranging from 38 to 200 MeV.

To examine the origin of this peak, the timing distribution for specific gamma-ray energy peaks are illustrated in Fig. 4.10. The energy-gated timing spectra are much sharper than the total timing spectrum, indicating there is a higher probability for the emission of specific gamma lines (i.e. 4.44 and 6.13 MeV) at different depth regions. Thus, the small peak seen

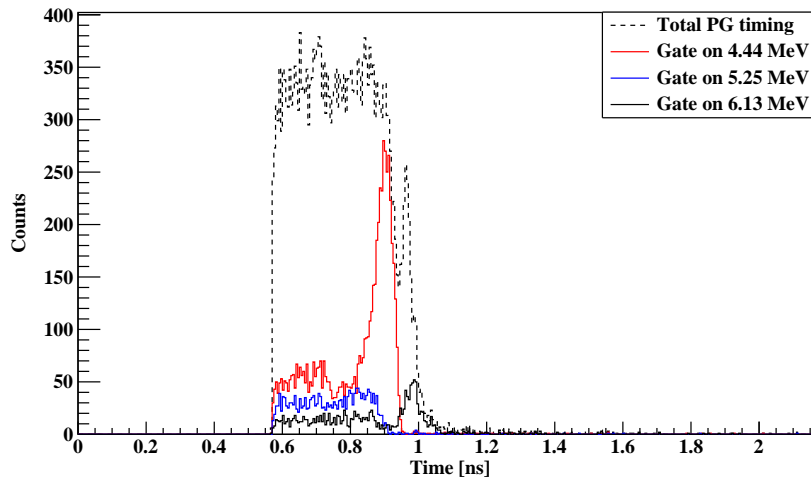


Figure. 4.10 A GEANT4 simulation of the timing spectra of PGs gated for specific energy peaks (i.e. 4.44, 5.24 and 6.13 MeV) produced in a water phantom irradiated with a proton beam energy of 65 MeV.

in the total PG timing distribution (dashed line) arises from the sum of PGs originating from specific reactions. In other words, the peak in the timing spectra reflects a maximum in the energy differential cross section for given reaction channels, e.g. for 6.13 MeV gamma-ray production intensity is maximum near the end of the proton trajectory when their energy is low while the 4.4 MeV that corresponds to an alpha knockout from ^{16}O shows a maximum much earlier when the protons still have substantial energy. Finally, for completeness, the timing spectra of secondary neutrons for various proton beam energies are displayed in Fig. 4.11, showing an increased emission probability for a higher incident beam energy and a decreasing emission probability as the different energy beams slow down.

4.2 The statistics of prompt gamma-rays

After the discussion of the properties of secondary radiations produced in the phantom, we concentrated on the statistics of PGs with regards to depth, medium and timing. The statistics are normalised to the total number of incident protons and the geometry of the simulation is the same as the one described in section 4.1.1 with a cylindrical water phantom as the scoring volume.

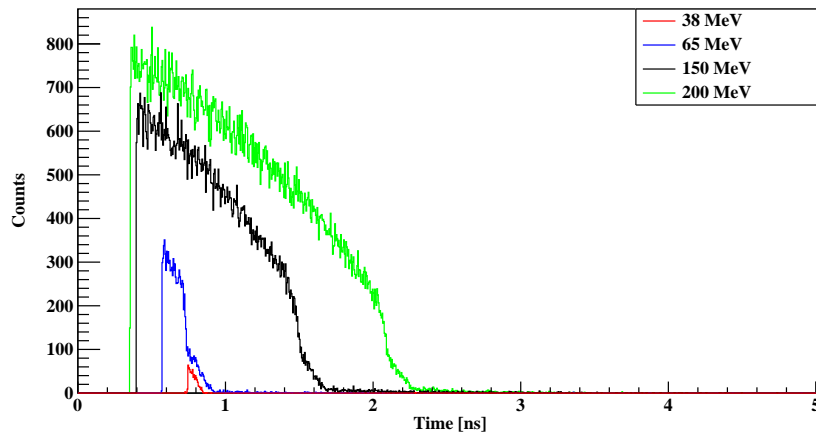


Figure. 4.11 A GEANT4 simulation of the timing spectra of neutrons produced in a water phantom irradiated with proton beams at various energies ranging from 38 to 200 MeV.

Table 4.1 The nuclear reactions of interest in water (H_2O) and the generated gamma-rays.

Target nuclei	Nuclear reaction	Gamma-ray energy [MeV]
O	$^{16}\text{O}(\text{p},\text{x})^{12}\text{C}^*$	4.44
	$^{16}\text{O}(\text{p},\text{x})^{15}\text{O}^*$	5.24
	$^{16}\text{O}(\text{p},\text{p}')^{16}\text{O}^*$	6.13

4.2.1 Statistics of specific gamma lines in the PGS

The three gamma lines of interest are the 4.44 , 5.24 and 6.13 MeV seen in Fig. 4.12, which shows the PG spectra obtained for various incident proton beam energies ranging from 38 to 200 MeV. Those gamma lines are produced from the de-excitation of nuclear-induced excited states in different isotopes as summarised in Tab. 4.1. From Fig. 4.12 the total emission of PGs is proportional to the incident energy of proton beams when the phantom was irradiated with the same number of incident protons (10^6 , number was chosen by considering both statistics and computing time), and the statistics of those three prominent gamma lines are summarised in Table. 4.2. It is noticeable that the peaks at 4.44 and 5.24 MeV are wider than that at 6.13 MeV, reflecting the production mechanism and lifetime of the populated states; the statistics at 4.44 MeV is the highest, while that at 6.13 MeV is the lowest for all proton beam energies, besides the 38 MeV. From those results, the expected gamma-ray yield at different beam energies can be estimated in experiments.

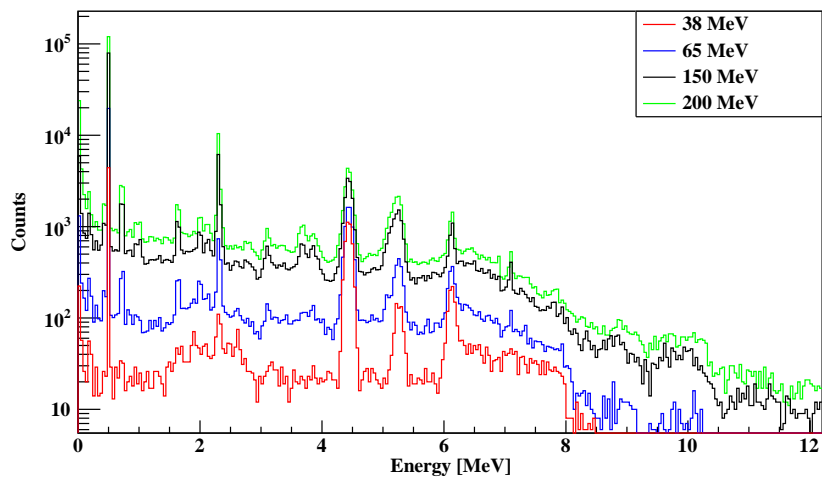


Figure. 4.12 A GEANT4 simulation of the energy spectra of PGs produced in a water phantom irradiated with proton beams at various energies ranging from 38 to 200 MeV.

Table 4.2 The statistics of generated gamma-rays in water for proton beam at various energies.

Proton Energy [MeV]	PG energy window [MeV]	Yield per proton
200	4.3-4.6	1.83×10^{-2}
	5.0-5.4	1.43×10^{-2}
	6.0-6.3	6.2×10^{-3}
150	4.3-4.6	1.4×10^{-2}
	5.0-5.4	9.8×10^{-3}
	6.0-6.3	4.5×10^{-3}
65	4.3-4.6	6.5×10^{-3}
	5.0-5.4	2.5×10^{-3}
	6.0-6.3	1.6×10^{-3}
38	4.3-4.6	4.1×10^{-3}
	5.0-5.4	7×10^{-4}
	6.0-6.3	9×10^{-4}

4.2.2 The retrieved PG intensity profile

The PG energy versus depth distribution is plotted in Fig. 4.13 for all PGs produced in the water phantom with incident beam energy of 150 MeV. As discussed earlier, the statistics of prominent gamma lines at 4.44 and 6.13 MeV increase as a function of depth, reaching the highest near the fall-off region (i.e. BP). Thus, it is desirable to retrieve the PG emission along the depth using those specific gamma lines for the range verification in PT. Fig. 4.14 shows the comparison of BP (dash line, scaled) and the PG profiles retrieved for selected PG peaks. It is obvious that the PG intensity profile retrieved from the 6.13 MeV is the most

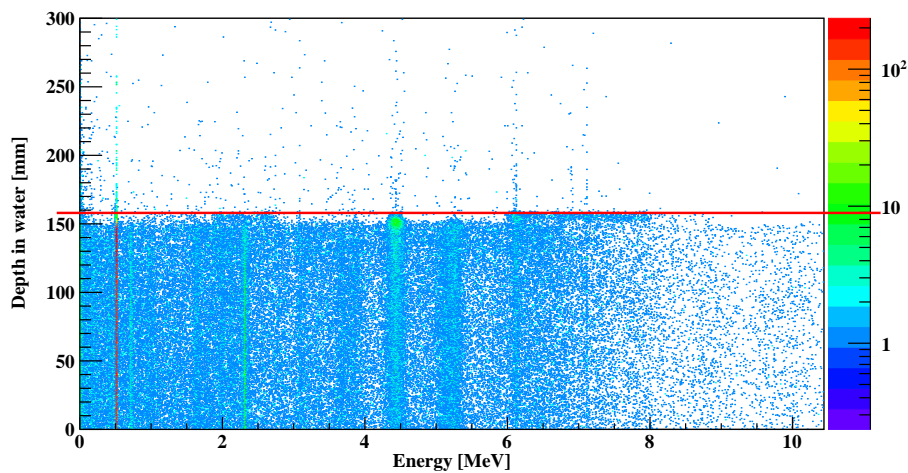


Figure. 4.13 A GEANT4 simulation of the energy versus depth distribution of PGs produced in a water phantom irradiated with a proton beam at 150 MeV. It is clear that the intensity of the 5.24 MeV gamma-ray spreads at a wide range of depth, while that of the 6.13 MeV peaks at depths near the BP (indicated with the horizontal line).

proximate to the BP while that from 5.24 MeV is far away from the BP. However, the total PG emission probability from 6.13 MeV (0.45 %) is the smallest compared with that from 4.44 MeV (1.40 %) or 5.24 MeV (0.98 %), as listed in Table. 4.2, so most often the total emission from all those three peaks is used to obtain the PG profile experimentally (i.e. the 3 - 7 MeV region is most often used).

4.2.3 PGS and PGT in various media

In this section, we focus on the statistics of PGS and PGT in different target media under the same beam conditions, since the heterogeneity of the target is commonly seen in clinical practice. Three target media were studied in Geant4 simulation for proton beams at 150 MeV, including water, PMMA and graphite. Water (H₂O) is the most common composition in

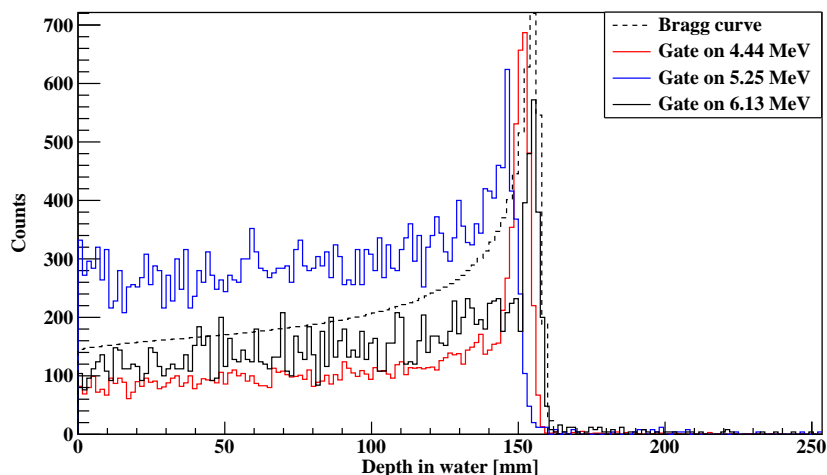


Figure. 4.14 A GEANT4 simulation of the statistics of PGs gated at specific energy peaks (4.44, 5.24, and 6.13 MeV) versus depth in a water phantom irradiated with proton beams at 150 MeV (the dash line was scaled).

Table 4.3 The interested nuclear reactions and the statistics of the corresponding PGs in various target media.

Material	nuclear reaction	gamma ray energy	statistics per proton
Water (H ₂ O)	$^{16}\text{O}(p,x)^{12}\text{C}^*$	4.44	1.4×10^{-2}
	$^{16}\text{O}(p,x)^{15}\text{N}^*$	5.24	9.8×10^{-3}
	$^{16}\text{O}(p,p')^{16}\text{O}^*$	6.13	4.5×10^{-3}
PMMA (C ₅ O ₂ H ₈)	$^{12}\text{C}(p,p')^{12}\text{C}^*$	4.44	
	$^{16}\text{O}(p,x)^{12}\text{C}^*$	4.44	9.6×10^{-3}
	$^{16}\text{O}(p,x)^{15}\text{N}^*$	5.24	5.0×10^{-3}
	$^{16}\text{O}(p,p')^{16}\text{O}^*$	6.13	2.6×10^{-3}
Graphite (C)	$^{12}\text{C}(p,p')^{12}\text{C}^*$	4.44	9.9×10^{-3}

human tissues; PMMA (C₅H₂O₈) has a density of 1.18 g/cm³ that is nearly water-equivalent and has the advantage that it is solid and it includes ¹²C, and graphite is the simplest material which only consists of naturally occurring Carbon, i.e. mostly ¹²C. Fig. 4.15 shows the energy spectra of PGs from these three media when irradiated with proton beams at 150 MeV. The PG yield from water is higher than that from the PMMA regarding all those three prominent peaks (4.44, 5.24 and 6.13 MeV), while there is only one strong peak at 4.44 MeV from the graphite medium. The summarised PG emission is illustrated in Table. 4.3, from which we can conclude that the PGS is closely related to the constitutions of the target media. In other words, it is possible to estimate the media via measuring the PG emission at certain gamma-ray energy peaks.

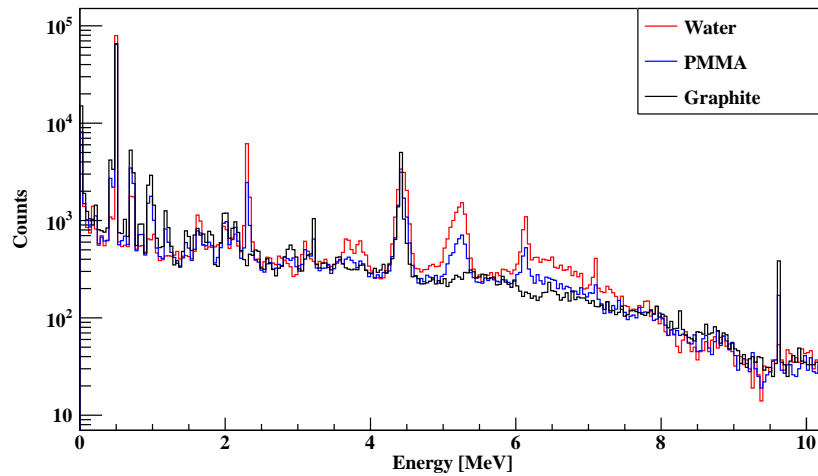


Figure. 4.15 A GEANT4 simulation of the energy spectra of PGs produced in various phantom (water, PMMA and Graphite) irradiated with a proton beam energy of 150 MeV.

Table 4.4 The simulated PGT and the corresponding statistics from various target media for a proton beams energy of 150 MeV.

Material	Timng cut [ns]	Statistics per proton
Water (H ₂ O)	0.2-2	8.9×10^{-2}
PMMA (C ₅ O ₂ H ₈)	0.2-2	6.7×10^{-2}
Graphite (C)	0.2-2	7.0×10^{-2}

Similarly, the PGT spectra for these three targets are plotted in Fig. 4.16, generated for a number of 10^6 incident protons at 150 MeV. The width of the PGT distribution is related to the composition of the material, giving a longest range (longest time) for water (i.e. lowest density). Moreover, the shape of the spectra is different, with an obvious fall-off peak for the graphite target generated by the large cross sections of specific nuclear reactions (e.g. $^{12}\text{C}(p,p' \gamma 4.44 \text{ MeV})^{12}\text{C}^*$) near the BP region. The statistics of those spectra is listed in Table. 4.4, which gives the total emission of PGs integrated along the x -axis (i.e. timing). Thus, it is also possible to quickly detect the heterogeneity of the target in the experiments via the measurement of PGT.

From this section, it is becoming evident that the heterogeneity of targets can be monitored quickly via both PGS and PGT, while it is also possible to deduce the composition of the target materials by the PG emission of specific gamma lines that were produced in characteristic nuclear reactions such as the ones shown in Table. 4.3. It is required that the detector has an excellent energy resolution for the spectroscopy analysis in PGS. On the other hand, a fast timing response of the detector is a necessity in PGT, which can be used to

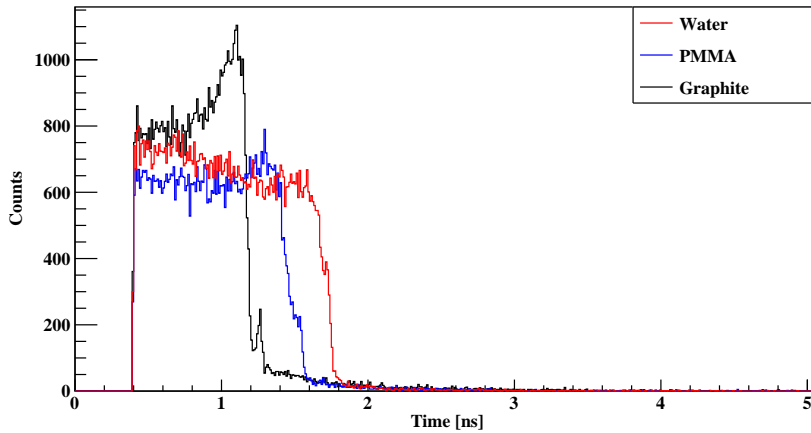


Figure. 4.16 A GEANT4 simulation of the timing spectra of PGs produced in water, PMMA and Graphite phantoms when irradiated with a proton beam of 150 MeV incident energy. The starting position of the proton beam is 6 cm upstream the phantom entrance window.

monitor the heterogeneity efficiently rather than retrieving the detailed material composition quantitatively.

4.3 Range errors using PG methods

In this section, we discuss the relative range uncertainties using different PG methods, including PGI, PGS and PGT that have been studied widely in PT. A cylindrical surface surrounds the water phantom, as seen in Fig. 4.17, which is placed 22 cm away from the centre of the beam line. The scoring surface acts like a perfect scoring “ring” detector that records the energy and timing of the coming PGs. In addition, the PGs were filtered by an energy cut at 1 MeV and an angular selection from 88.3 to 91.7 degree with respect to the beam direction to compare the sensitivity of those range verification methods. This is not a direct comparison of the range uncertainties for those three PG methods, as different analysis methods were applied for each of them.

4.3.1 PGI

The most straightforward method of range verification is PGI that monitors the emission of PGs along the depth of a phantom (i.e. 1D PG intensity profile). This method is validated for both the absolute and relative range verification and requires minimal data manipulation. The simulated 1D PG intensity profiles are plotted in Fig. 4.18 with various lengths of phantom shift (the movement of phantom upstream) ranging from 0 to 4 mm. A sigmoid function

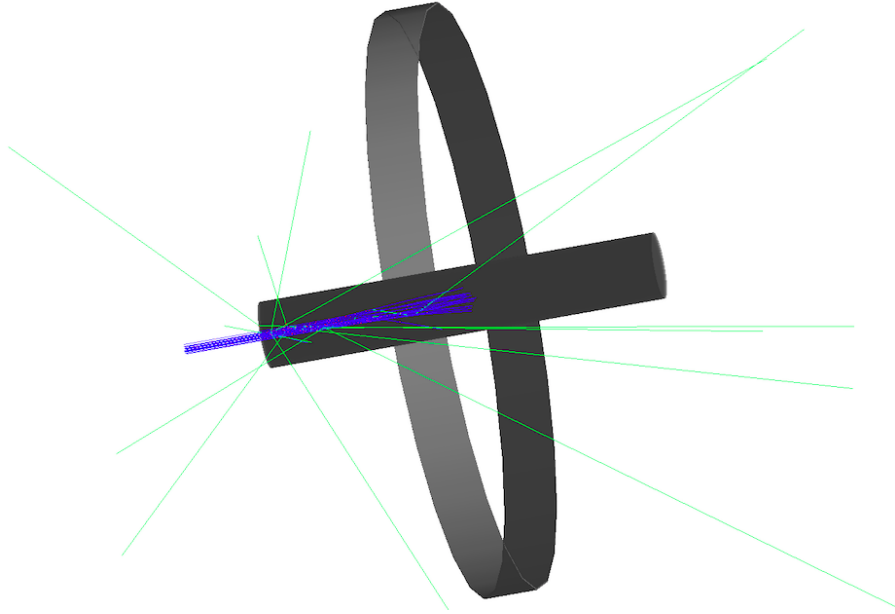


Figure. 4.17 A perfect ‘ring’ detector defined in Geant4 simulation.

Table 4.5 The simulated PG range with various lengths of phantom shift. A total of 10^8 protons (number was chosen when the statistical error is small and computing time is acceptable) were applied for each case.

Phantom shift [mm]	PG range [mm]	Error [mm]
0	157.20	0.09
1	158.10	0.08
2	159.07	0.09
4	161.14	0.09

was applied to fit the fall-off region of the profile, as illustrated in the figure. The function is basically an error function with four parameters:

$$\text{Sigmoid} = c \times \text{erfc}[a \times (z - b)] + d \quad (4.1)$$

where z is the target depth, erfc is the complementary error function with four parameters a , b , c and d ; b corresponds to inflection point of the error function which was confirmed to be close to the proton beam range [77], referred to ‘PG range’ in this thesis. The PG range (i.e. evaluated parameter b) and its uncertainty given by the fit is summarised in Table. 4.5. It is noticeable that the difference of PG ranges among those four cases is consistent with the corresponding length of phantom shift and even a 1 mm-shift is detectable with the given incident proton statistics (i.e. 10^8).

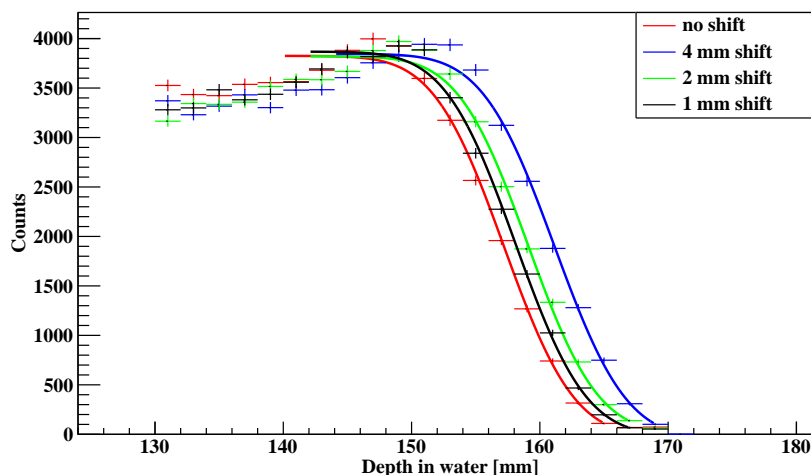


Figure. 4.18 A GEANT4 simulation of the PG profiles (i.e. selected gamma-ray energy more than 1 MeV) recorded in a perfect ‘ring’ surrounded a water phantom. The water phantom was shifted in the beam direction up to 4 mm and the applied incident beam energy was at 150 MeV.

Table 4.6 The simulated PG range errors and the corresponding statistics of incident protons for the no phantom shift case.

Proton numbers	Square root of proton numbers	PG range [mm]	Error [mm]
10^6	1000	154.86	1.56
5×10^6	2236	155.77	0.43
10^7	3162	157.23	0.30
5×10^7	7071	157.23	0.13
10^8	10000	157.20	0.09

To study the range uncertainty for various incident proton statistics, the PG intensity profiles were simulated for proton numbers ranging from 10^6 to 10^8 with no phantom shift. Table. 4.6 displays the PG range and the corresponding error for proton statistics. The range error is inversely proportional to the square root of the proton statistics, and is found to be around 1.56 mm when the simulated number of protons was 10^6 and 0.09 mm when that was 10^8 . The relationship between range errors and proton statistics is critical in experiment for the estimation of beam current and the configuration of detector prototype.

4.3.2 PGS

The energy spectra of PGs obtained by the simulation are plotted in Fig. 4.19 for various lengths of phantom shift, increasing from 0 to 4 mm. The prominent gamma lines at 4.44, 5.24 and 6.13 MeV are clearly identified and the statistics of those peaks shows small fluctuations in those four cases. To estimate the statistics of those spectra, we divided

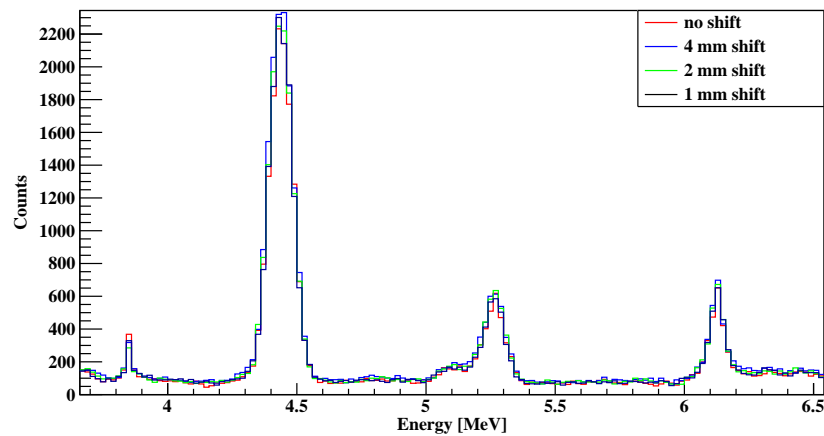


Figure. 4.19 A GEANT4 simulation of the PGS (i.e. selected gamma-ray energy higher than 1 MeV) scored in a perfect ‘ring’ surrounding the water phantom at various positions. The water phantom was shifted in the beam direction up to 4 mm and the applied incident beam energy was 150 MeV.

each of the histograms with phantom shift at 1, 2 and 4 mm to the histogram without a shift respectively. The ratios obtained from the division of the above three cases are displayed in Fig. 4.20, which gives the ratio distribution regarding energy with coarse binning. Those ratio distributions were fitted via a constant function (i.e. the mean) from 4 to 6 MeV, extracting the average value of the ratio within the energy window.

The average ratio and sigma were summarised in Table. 4.7. The mean of ratio increases with the length of phantom shift, giving the highest ratio at 4 mm (1.10) and is 0.08 higher than that with 1 mm shift. However, the 3σ of the ratio is around 0.13, making it challenging to detect a phantom shift less than 3 mm.

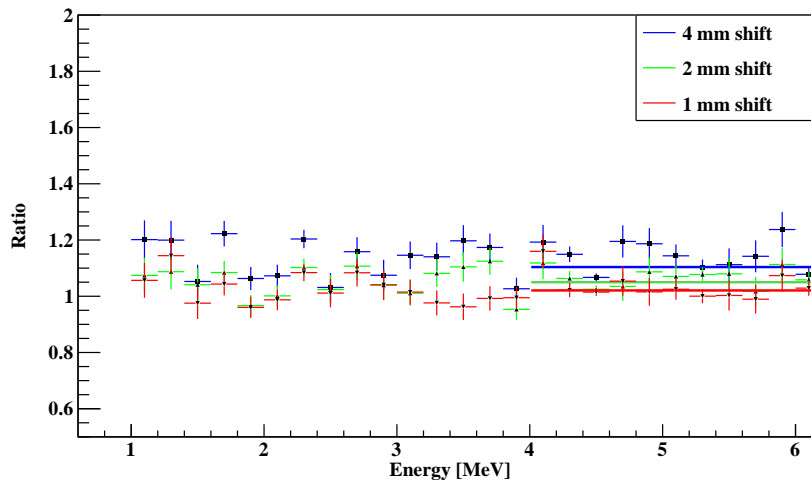


Figure. 4.20 A GEANT4 simulation of the ratio distribution of PGS detected in a perfect ‘ring’ surrounded a water phantom at various positions. The water phantom was shifted in the beam direction up to 4 mm and the applied incident beams was 150 MeV.

Table 4.7 The PGS ratios for each phantom shift. A total of 10^8 protons were applied for each case.

Phantom shift [mm]	Ratio of PGS	Sigma
0	NAN	NAN
1	1.02	0.04
2	1.05	0.04
4	1.10	0.05

Table 4.8 The PGT with various lengths of phantom shift. A total of 10^8 incident protons were applied for each case.

Phantom shift [mm]	Mean [ns]	Sigma [ns]	Mean error [ns]
0	2.340	0.100	0.004
1	2.346	0.100	0.003
2	2.353	0.097	0.004
4	2.380	0.094	0.003

4.3.3 PGT

Apart from the energy, the timing of the PGs can also be utilised for the relative range verification. Fig. 4.21 shows the timing spectra of PGs for various phantom shifts. There are peaks at the end of the range that were fitted with gaussian functions, displayed with solid lines. Those fitted parameters are summarised in Table. 4.8, including the mean, σ and the error of the mean. As noticed in Fig. 4.21, the mean value of those timing spectra shifts to the right side with increasing phantom shift. The timing difference (i.e. mean value) for a 1 mm-shift is less than 10 ps, and that for a 4 mm-shift is around 40 ps. However, the σ of the Gaussian fitted peak is around 100 ps due to the geometry of the detector (i.e. a 5 cm-length ‘ring’).

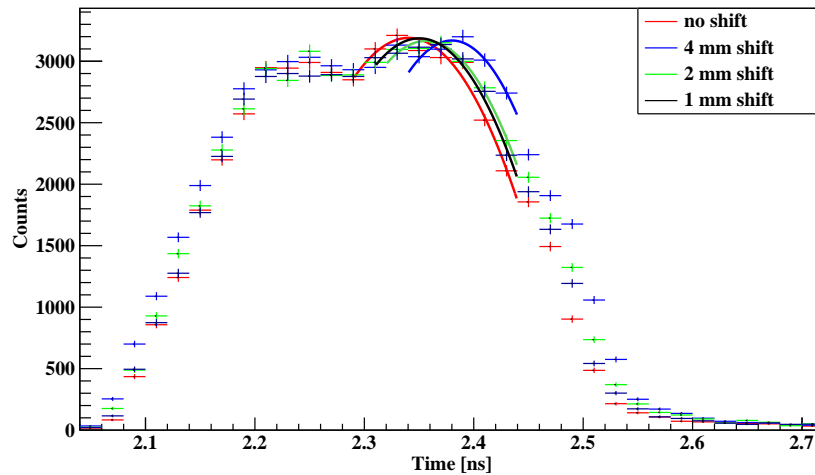


Figure. 4.21 A GEANT4 simulation of the PGT (i.e. selected gamma-ray energy higher than 1 MeV) scored in a perfect ‘ring’ detector surrounding a water phantom placed at various positions (shifts from 0 to 4 mm). The incident proton beam energy was 150 MeV.

4.4 Detector response for PGs

After the introduction of some methods for range verification via detecting PGs, the detector response of our detection prototypes are also simulated, including that in the CLLB detector, the LYSO arrays and the fibre probe. For simplicity and computational efficiency, the optical processes in the scintillators and the electronics readout components were not applied in the simulation. Moreover, the results presented here were extracted from the sensitive volumes (i.e. scintillating detectors) assuming perfect energy and timing resolution. The simulated geometry is presented in Fig. 4.22. For details on detector dimension and configuration see Chapter 3, section 3.1.

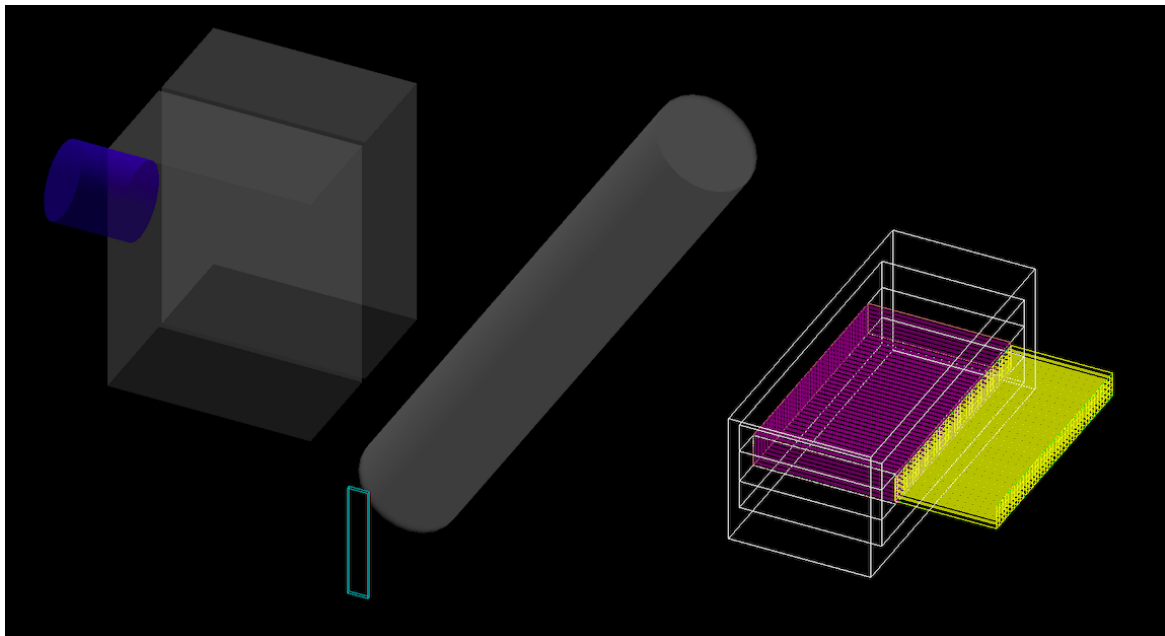


Figure. 4.22 The experimental setup defined in Geant4 simulation.

4.4.1 CLLB detector response

Fig. 4.23 gives the histograms of the total energy deposited in the CLLB, for a proton beam energy of 150 MeV impinging on a water phantom. The spectrum in blue was generated with a timing cut at less than 2.6 ns. The background noise reduces by nearly 10 times when the timing cut is applied, rejecting most of the neutron-induced signal from the phantom and collimators. Hence, the peak-to-noise ratio has been improved after the timing cut, showing the prominent peak at 4.44 MeV together with its double (d.e.) and single (s.e.) escape peaks, as labelled in Fig. 4.23. The s.e. and d.e. peaks are strong due to the small size of the detector

crystal (1.5 inch). Other interesting gamma lines at 5.24 and 6.13 MeV were not obvious due to the statistics of incident protons (10^{10} , a high number to have enough statistics in the detector) simulated in each run. As discussed in section 4.1.2, the yield of neutrons increases significantly with the incident proton beam energy, so that a timing cut is required for a clear PGS in PT when the incident proton energy is relatively high (i.e. more than 100 MeV).

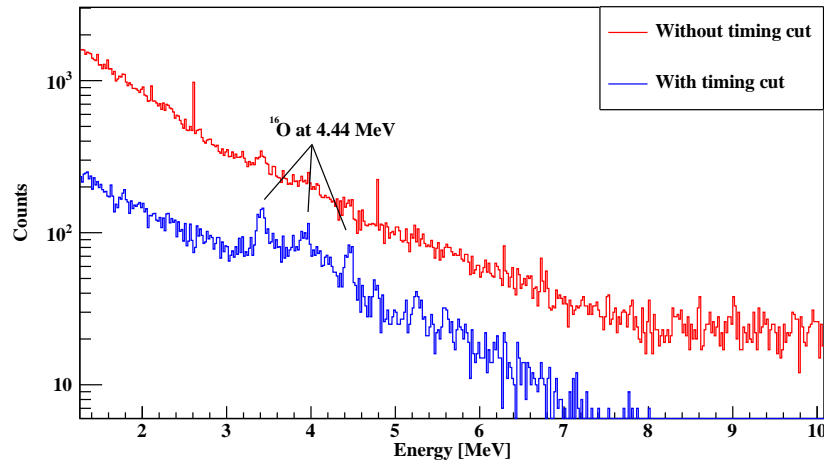


Figure. 4.23 A GEANT4 simulation of the simulated energy spectra of secondary radiation detected in the CLLB with and without a timing cut. The water phantom was irradiated with a proton beam energy of 150 MeV.

The timing spectra scored in the CLLB is shown in Fig. 4.24, presenting a sharp Gaussian peak at 2.4 ns and a broad peak and long tail after 2.6 ns. The Gaussian peak is the real timing spectrum of the PGs, while the broad peak and long tail are from the neutron-induced signal. Thus, the timing cut applied for the energy histogram was selected as 2.6 ns, which rejects most of the neutron-induced background noise. Even though the CLLB is simulated with perfect timing resolution, the FWHM for the timing peak is still around 235 ps due to the range straggling of the proton beam near the end of the BP and the gamma-ray interaction position in the CLLB crystal (i.e. 3 cm length corresponds to about 100 ps in time, depending on if the gamma-ray interacted at the front or the back of the crystal).

4.4.2 LYSO detector response

The 2D distribution of secondary radiation yield as scored in the LYSO arrays (i.e. 128 crystals) is shown in Fig. 4.25. An energy selection window from 1.3 to 6 MeV has been applied for each pixel to reject the gamma-rays at both low and high energy region which are not related to the range information. To visualise the statistics in beam direction (i.e.

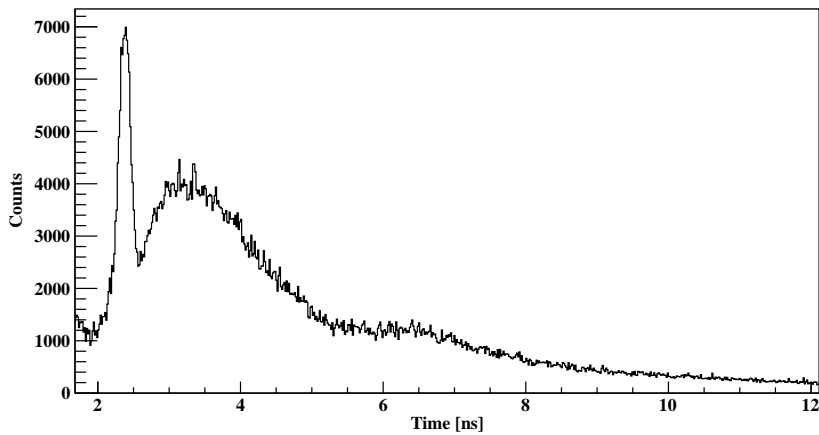


Figure. 4.24 A GEANT4 simulation of the timing spectrum of secondary radiation scored in the CLLB, for a proton beam energy of 150 MeV.

depth), we plotted the 1D projection of the 2D mapping on the x -axis (see Fig. 4.26). The PG intensity profile is displayed with 8 LYSO detectors behind the multi-slit tungsten collimator, in which case the statistics on each column (i.e. 4 crystals) of the detector has been summed up and presented in the y -axis. It is noticed that there are more statistics on the entrance part of the detecting window, due to the design of the collimation system (two pieces of lead sheet on the two sides), producing more neutron-induced background. Besides, some radiations were detected even after the fall-off region, which is also from the neutron-induced background inside the detecting window. A sigmoid function was fitted on the fall-off region in the PG intensity profile, giving the value of PG range to be around 157.4 mm which is consistent with that obtained in section 4.3.1 with a perfect ‘ring’ (see Tab. 4.5, i.e around 157.2 mm).

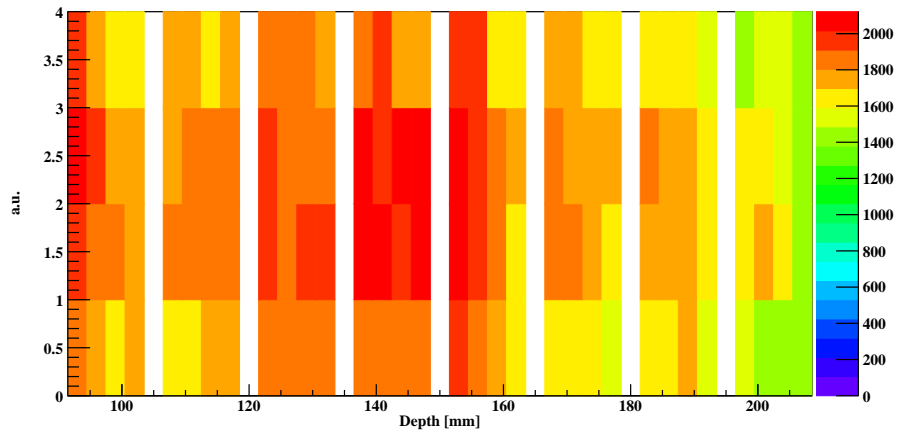


Figure. 4.25 A GEANT4 simulation of the spatial distribution of secondaries scored in the LYSO arrays for a proton beam energy of 150 MeV (10^{10} incident protons). The y-axis is just arbitrary unit representing the geometry of the crystal arrays.

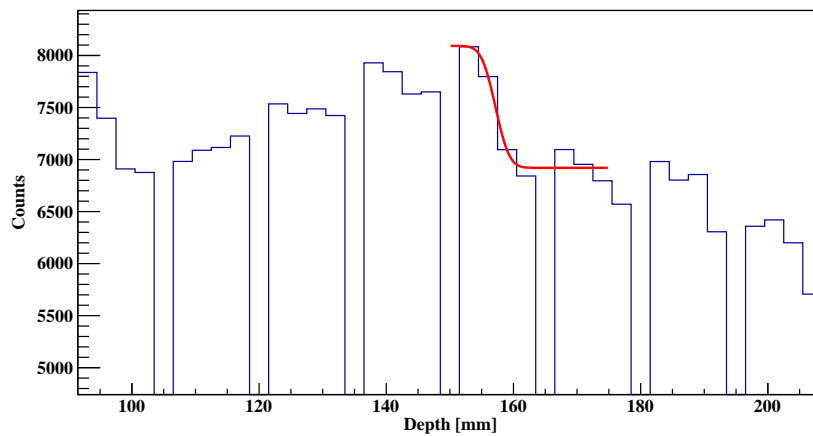


Figure. 4.26 A GEANT4 simulation of the PG intensity profile in the LYSO arrays along the depth of a water phantom irradiated with a proton beam energy of 150 MeV.

4.4.3 Fibre probe response

Last but not least, the fibre probe was inserted in the water phantom to record the energy and timing of proton beams. In Fig. 4.27 the results are shown when the fibre was placed at 150 mm-depth (i.e. approaching the BP) inside the water phantom. The energy spectrum has a peak at around 2.5 MeV, then it falls dramatically at around 4 MeV. On the other hand, the timing spectrum follows a Gaussian distribution, giving the mean at around 1.63 ns and FWHM at around 13 ps. The FWHM of the timing spectrum also arises from the energy straggling of protons approaching the BP.

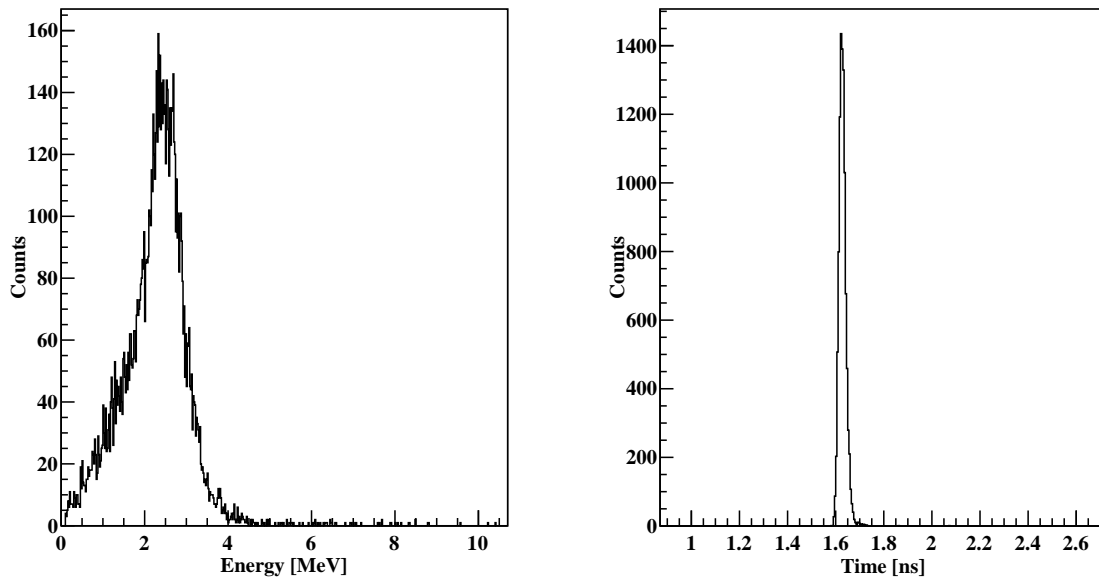


Figure. 4.27 A GEANT4 simulation of the energy (left) and timing (right) spectrum scored in the fibre probe inserted at 150 mm in a water phantom that is irradiated with a proton beam energy of 150 MeV. The starting position of the proton beam is 6 cm upstream to the entrance window of the phantom.

The fibre probe was also simulated at various depths inside the water phantom, sampling the whole range of the proton energies. Fig. 4.28 shows the normalised total energy deposited in the fibre (i.e. the area integral of energy spectrum divided by the number of incident protons). The normalised total energy deposited in the fibre was scaled by a factor of 8.2 to the first point of BP, giving a good agreement from 0 to around 100 mm, while showing an underestimation for the energy deposition approaching the BP to the end of range (from 100 to 166 mm). The small size of the fibre probe (1 mm in diameter) leads to 10 times lower energy deposition compared with the BP region. The range ($R_0 \cong d_{80}$) estimated from the

energy-depth curve recorded in the fibre probe is around (156.6 ± 1.0) mm, which agrees with the that estimated from the BP curve (157.7 ± 1.0) mm.

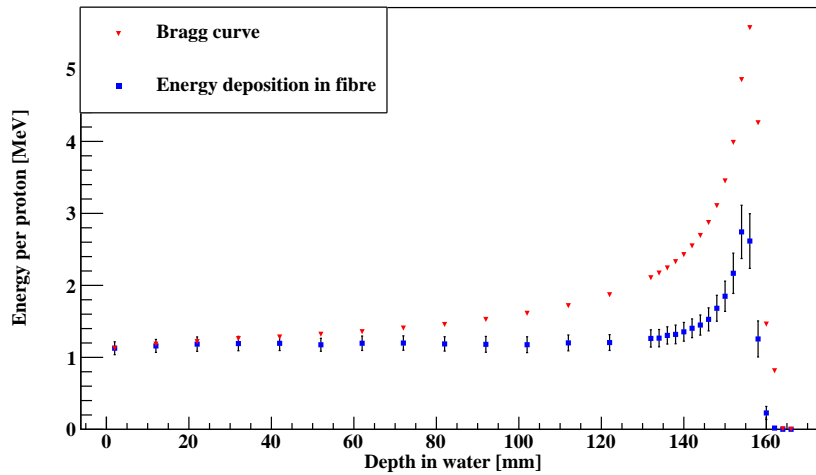


Figure. 4.28 A GEANT4 simulation of the comparison of BP and the integrated total energy deposited (scaled) in the fibre probe inserted at various positions in a water phantom that irradiated with a proton beam energy of 150 MeV. The error bar in the Bragg curve is too small to show, as 10^5 protons were used on each position.

The significant reduction of the proton statistics at the end of the range is due to the energy straggling of the protons as they slow down near the BP. This method still shows acceptable uncertainty to retrieve the range on the BP region, even the statistics recorded in the fibre dropped dramatically (i.e. beam divergence) causing critical energy straggling to dominate in this region.

Finally, the timing distribution of the proton beam, as measured by the fibre for various depths in the phantom is plotted in Fig. 4.29. The mean value of a Gaussian fit to the timing spectra is plotted as a function of depth. The time difference of proton beams recorded by moving the fibre for 2 mm inside the phantom near the BP region is around 25 ps.

4.5 Summary

In this chapter, we studied range verification in PT based on the detection of nuclear-induced secondaries using MC Geant4 toolkit. We firstly simulated the properties of three types of secondaries (protons, neutron and PGs) produced in a water phantom irradiated with various beam energies. Then, the energy, timing and statistics of PGs were scored in three target media (water, PMMA and graphite) to study the heterogeneity of tissues in PT. Those basic

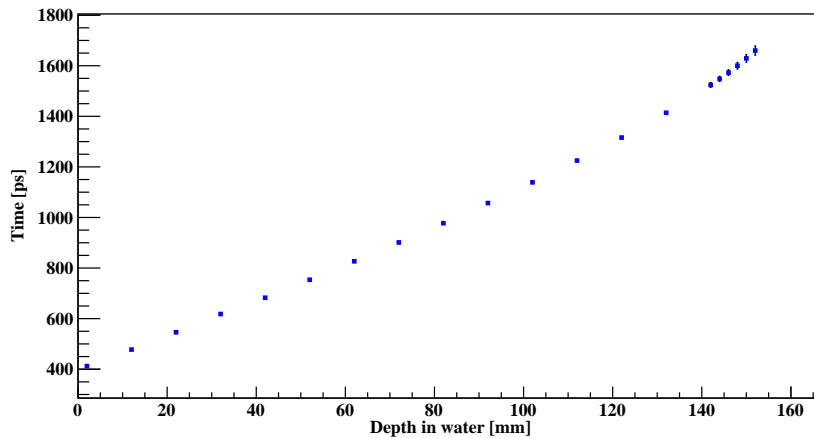


Figure. 4.29 A GEANT4 simulation of the timing scored in the fibre probe inserted at various positions in a water phantom irradiated with a 150 MeV proton beam.

results scored in a simple phantom demonstrated the correlation between the PG profile and the BP. We found that the PG profile retrieved from a specific gamma line (6.13 MeV) is the most proximate to the BP, since the cross section of $^{16}\text{O}(p,p' \gamma 6.13 \text{ MeV})^{16}\text{O}^*$ peaks in the BP region.

In the next part, we added a perfect ‘ring’ surrounding the water phantom to estimate the range errors using different methods based on the detection of PGs, including PGI, PGS and PGT. We found that the PGI detected a 1 mm phantom shift; PGT worked slightly less well (2 mm phantom shift), while PGS failed to detect a phantom shift up to 3 mm under the same detector geometry and statistics. Those range errors from different methods cannot be compared directly since different analysis methods were applied in each case, and the detector geometry were not optimised specifically (e.g. large detector “ring” is appealing for PGS and PGI but not for PGT). We demonstrated the possible analysis methods to estimate range errors here.

Finally, our detector prototypes were simulated to assess the detector response under clinical beam conditions (i.e. 150 MeV). Some interested information were scored in our sensitive volumes, specifically, the PGS and PGT in the CLLB, the PG intensity profile in LYSO arrays and the energy and timing of proton beams in the fibre probe, demonstrating the feasibility of using different types of scintillator for the range verification in PT. It was found that the neutron-induced background noise was rejected mostly as we applied a timing cut in the CLLB, improving the peak-to-noise ratio in the energy spectrum. Additionally, the PG range retrieved from the statistics recorded in LYSO pixels was around 157.4 mm via fitting a sigmoid function, which is consistent with that calculated inside the water phantom

by the fibre probe (around 156.6 mm). The energy and timing of proton beams were also scored in the fibre probe at various depths inside the phantom, from which the energy-depth curve were compared to the BP. The energy extracted from the integral of the energy spectra agrees with the BP in x -axis (depth), even though the normalised energy deposition (scaled) is lower than the BP in the fall-off region due to the severe beam divergence.

Chapter 5

In-beam experiment with the Birmingham MC40 cyclotron

In this chapter, we introduce first the specific experimental setup and methods that were used for the in-beam experiment at the MC40 cyclotron facility at the University of Birmingham, then the results using a proton beam of 38 MeV are presented. Even though this low energy beam is rarely applied in clinical practice, it is favourable to study the characteristics of PGs emitted from the proton-induced nuclear reactions, as most cross sections of interest peak at around 10 to 20 MeV and the neutron-induced background is lower than that for high energy proton beams. The experiment aims to understand and characterise the detector performance in detecting high energy PGs (4 - 6 MeV), and therefore prepare for the next experiment with high energy proton beams.

5.1 Methods

The proton beam was pulsed at a radio frequency (RF) of 26 MHz, corresponding to a period of around 38.5 ns, and the beam spot size was comparable with that applied in clinical treatment ($\sigma \approx 2$ mm). The beam intensity was limited by the count rate on the detectors to about 10^8 to 10^9 Protons/sec.

As shown in Fig. 5.1, three $5 \times 5 \times 5$ cm³ targets (water, PMMA and graphite) were irradiated with incident protons, emitting PGs that can be detected by both the single-slit collimated CLLB detector or the multi-slit collimated LFS arrays. Moreover, the photograph of the experimental setup is shown in Fig. 5.2. On one side of the water phantom there was a single-slit collimation system consisting of two lead blocks placed at 12.0 cm from the beam line (i.e. the distance from beam to the front surface of lead blocks) and the open slit

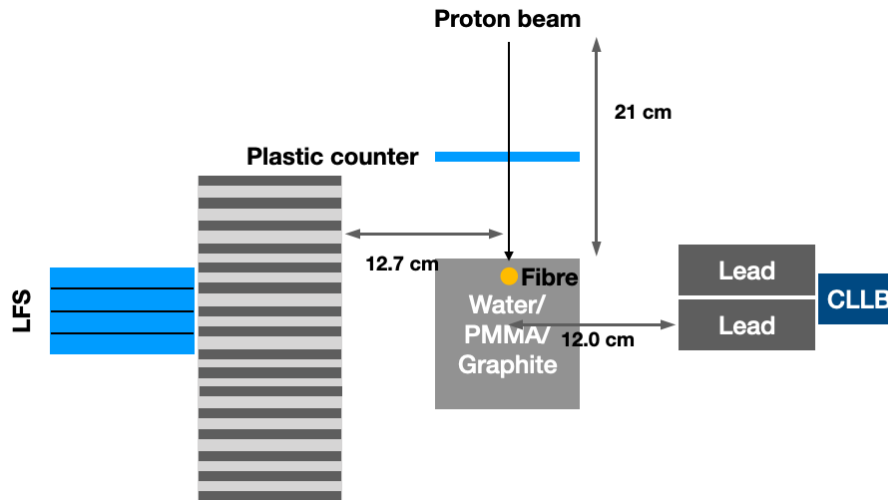


Figure. 5.1 The schematic drawing (top view) of the experimental setup in Birmingham. The fibre probe can only be used in the water phantom and not the solid PMMA and graphite.

width was (3.0 ± 0.5) mm. The CLLB was placed just behind the lead blocks to measure the PGs emitted in the direction perpendicular to the beam line. On the other side of the water phantom the array of LFS detectors was placed behind tungsten slits. The distance between the beam line and the front surface of slits was around 12.7 cm. The LFS array used in this experiment had a total of 16 crystals (i.e. 4 by 4 array) instead of the full 128-crystal array. Only 4 crystals in a row along the beam direction were connected to the digitiser due to the limited number of digitiser channels. The details of the configuration of these detectors and collimations were discussed in Chapter 3, Section 3.1.

The CLLB detector (1 inch and 1.5 inch) was firstly calibrated with two radioactive sources: ^{22}Na (γ decay at 0.511, 1.275 MeV) and ^{24}Na (γ decay at 1.368, 2.754 MeV). We then studied the prominent nuclear-induced gamma lines from different target media (water, PMMA and graphite) in the monolithic CLLB (1.5 inch). A smaller CLLB (1 inch) was coupled with the plastic counter in coincidence mode to measure the PGs from a water phantom, rejecting the neutron-induced noise. Furthermore, the water phantom was moved by the linear stage to scan the rate of PGs detection as a function of the position of the water phantom with both sizes of detectors. In the meantime, the emission of PGs from the water phantom were recorded in the 4 pixels of the LFS array. Finally, the energy and timing of protons were recorded in the fibre probe that was coupled with the plastic counter in coincidence mode to obtain the timing structure of the proton beams.

The DT5730 digitiser discussed in Chapter 3, section 3.2.2 was the only DAQ system used in this experiment, since the ASICs were not prepared at that time. A Geant4 simulation

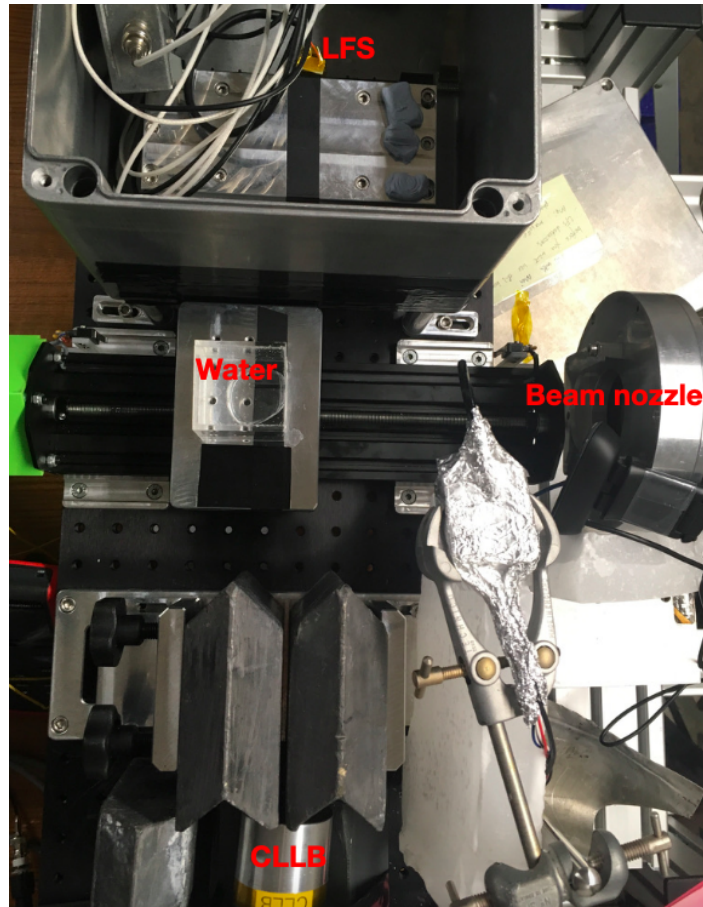


Figure. 5.2 The photograph of the experimental setup in Birmingham. The water phantom was placed on the top of the linear stage. Two PG detection systems were placed on the two sides of the phantom and there was a plastic start counter placed on the beam line

code was also developed for this experimental setup, tracking and scoring the produced secondaries in sensitive volumes and the physics lists applied were same as we discussed in Chapter 4, Section 4.1.1.

5.2 PGS in the CLLB

The calibrated energy histogram of the two radioactive sources measured in the CLLB (1.5 inch) is presented in Fig. 5.3 with peaks of interest labelled. A high threshold was applied to exclude the noise in the low energy region, giving a reduced peak at 0.511 MeV, which sat exactly on the threshold. The double escape (d.e.) and single escape (s.e) peaks are observed for the high energy gamma-ray from ^{24}Na (2.754 MeV). The energy resolution of the CLLB at 1.275 and 2.754 MeV was around $(5.4 \pm 0.3) \%$ and $(3.5 \pm 0.1) \%$ respectively, in the current setup.

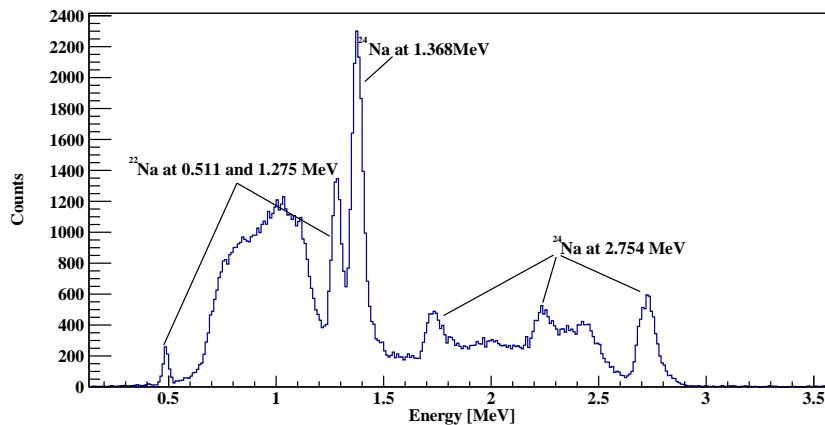


Figure. 5.3 The calibrated energy spectrum from ^{22}Na and ^{24}Na detected in the CLLB (1.5 inch).

As discussed previously, the CLLB is a dual gamma-neutron detector and the emitted thermal neutrons from the irradiated phantom were also detected. The signal pulse of a gamma ray differs from that of a thermal neutron regarding the decay time (illustrated in Chapter 3, section 3.2.2) so PSD was applied to distinguish those two types of radiation. The measured energy histograms of secondaries from a water phantom are shown in Fig. 5.4 with and without the PSD applied. The background noise was reduced considerably and the thermal neutron-induced peak at 3.2 MeV was removed once PSD analysis was applied. The gamma lines of interest from $^{16}\text{O}(p,x)^{12}\text{C}$ and $^{16}\text{O}(p,p')^{16}\text{O}$ at 4.44 and 6.13 MeV, respectively, are labelled in the figure together with their corresponding d.e. and s.e. peaks.

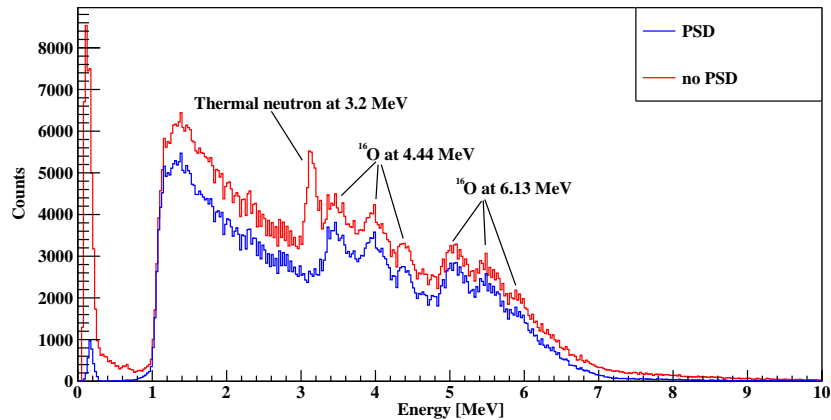


Figure. 5.4 The energy spectrum obtained from a water phantom run analysed with (red) and without PSD (blue), as detected in the CLLB (1.5 inch). A total of 7.6×10^{11} protons impinged on the water phantom in this run. The characteristic neutron absorption peak of the dual-mode CLLB scintillator is evident at 3.2 MeV when it is not excluded by the PSD analysis. The energy threshold is not the same as the that stated in Figure. 5.3 due to the increase of room temperate (SiPM noises increase with temperate).

The experimental and simulated energy spectra at relatively lower protons statistics (10^{10} protons) are also presented in Fig. 5.5 for comparison, which shows that the Geant4 simulation underestimates considerably the emission of d.e. and s.e peaks from the 6.13 MeV gamma line.

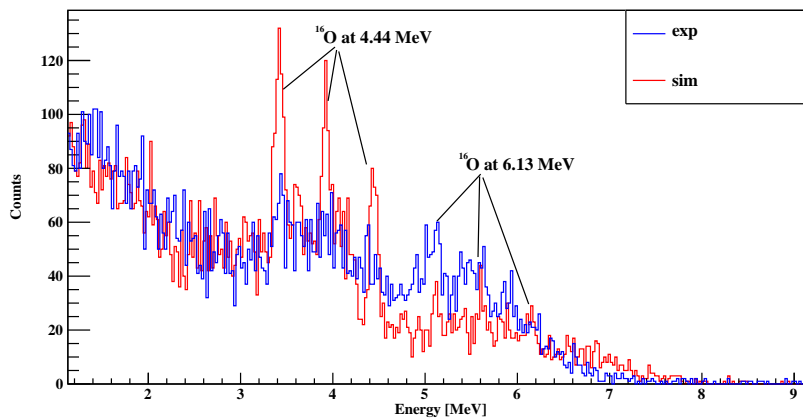


Figure. 5.5 The comparison of energy spectra from a water phantom in experiment and simulation detected in the CLLB (1.5 inch). A total of 10^{10} protons were applied for both cases. The simulation underestimates the production of d.e. and s.e. peaks from the 6.13 MeV gamma line.

Table 5.1 The nuclear reactions of interest in target media and the yield of generated gamma-rays.

Material	Nuclear channel	γ -ray energy [MeV]	Yield per proton
Water (H ₂ O)	$^{16}\text{O}(\text{p},\text{x})^{12}\text{C}^*$	4.44	2.2×10^{-7}
	$^{16}\text{O}(\text{p},\text{p}')^{16}\text{O}^*$	6.13	1.3×10^{-7}
PMMA (C ₅ O ₂ H ₈)	$^{16}\text{O}(\text{p},\text{x})^{12}\text{C}^*$	4.44	
	$^{12}\text{C}(\text{p},\text{p}')^{12}\text{C}^*$	4.44	2.3×10^{-7}
	$^{16}\text{O}(\text{p},\text{p}')^{16}\text{O}^*$	6.13	7.6×10^{-8}
Graphite (C)	$^{12}\text{C}(\text{p},\text{p}')^{12}\text{C}^*$	4.44	2.6×10^{-7}

The energy histograms of PGs from various target media are plotted in Fig. 5.6, illustrating the specific gamma lines from the reactions of interest. These nuclear reactions and the yield of generated PGs from different target media are summarised in Table. 5.1. It is obvious that the PG emission at 4.44 MeV is the highest in the graphite, while that at 6.13 MeV is the highest in water, as expected. The specific energy response form various target compositions indicate that the PGS detected in the CLLB quantitatively shows the BP position regarding the target materials.

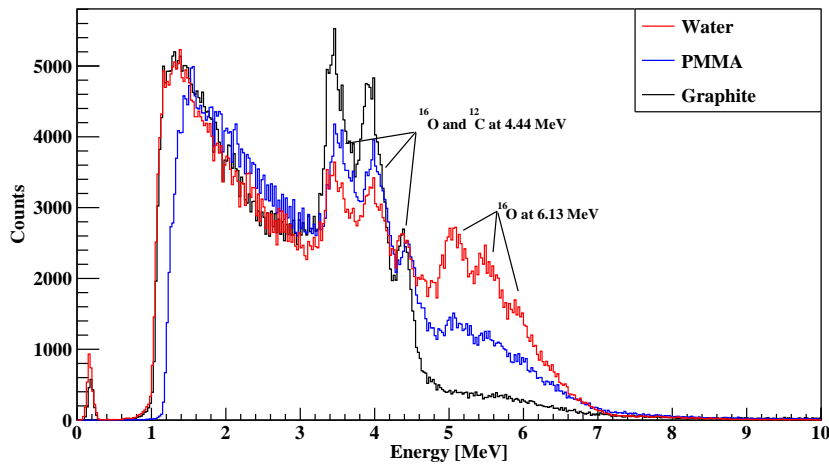


Figure. 5.6 The energy spectra from various target media (water, PMMA and graphite) in the CLLB (1.5 inch) placed near the BP position. A total of 7.6×10^{11} protons were applied for each of the three cases.

On the next part of the experiment, we combined the smaller CLLB (1 inch) with the plastic counter to select coincidence signals from both detectors arriving within a time window of 496 ns, which rejects most of the neutron-induced background. The incident beam current was reduced by a factor of 10 due to the restriction of count rate in the plastic counter. The energy spectrum detected in the CLLB (1 inch) is displayed in Fig. 5.7, giving a clearer histogram compared with that plotted in Fig. 5.4, since more gamma lines are resolved

(i.e. the 5.24 MeV from ^{15}O) and the peak-to-noise ratio for the d.e. of the 6.13 MeV gamma-ray is improved by around 12 %. There are primary two reasons leading to a clearer spectrum here: the coincidence mode rejects most of the neutron-induced noises and the energy resolution of the smaller CLLB is better ¹.

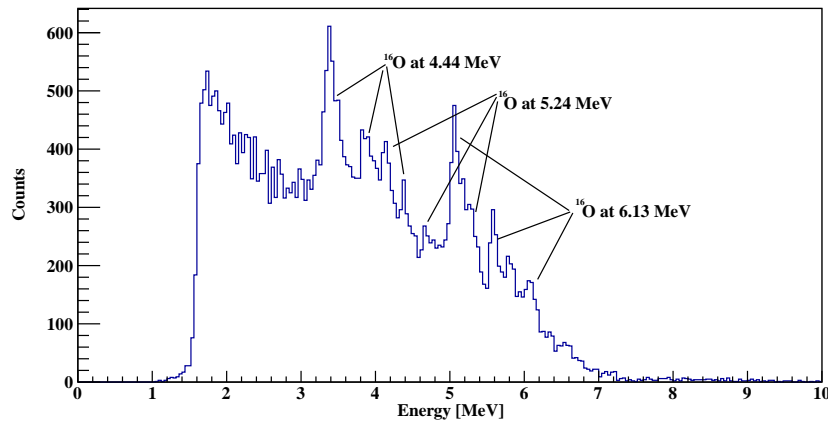


Figure. 5.7 The energy histogram of PGs from a water phantom detected in the CLLB (1 inch) that coupled with the plastic counter. A coincidence window of 496 ns was applied for the CLLB and the plastic counter. A total of 7.6×10^{10} protons were used at a relatively low beam current 10^8 p/s.

The coincidence timing distribution of those two detectors is shown in Fig. 5.8, where there are many Gaussian peaks ranging from -496 to 496 ns. The highest peak was fitted with a Gaussian function ($\sigma \approx 1.8$ ns), representing the coincidence prompt peak between the secondary gamma-rays and the incident proton bunches. The period of those peaks is around 38.4 ns that is consistent with the period of the MC40 cyclotron (i.e. around 38.5 ns).

We also simulated the timing spectrum in the CLLB for comparison shown in Fig. 5.9, considering an excellent timing response and with time spread only due to energy straggling ($\sigma \approx 75$ ps). The timing resolution of 2.1 ns during the experiment has contributions from the range straggling, the beam bunch distribution and the detection resolution, while the resolution from energy straggling is only about 75 ps as shown in the simulation. Thus, the coincidence timing resolution between the CLLB and plastic counter is mainly from the detection system and the beam bunch spread.

Finally, the PG profiles measured in the CLLB detectors with and without coincidence mode were retrieved from the energy histograms at various depths in the water phantom (see Fig. 5.10). The PG profile acquired with the coincidence mode shows a better signal-to-noise ratio (SNR) compared with the that acquired without coincidence mode even with

¹2.4 % in CLLB (1 inch) VS 3.5 % in CLLB (1.5 inch) at 2.75 MeV.

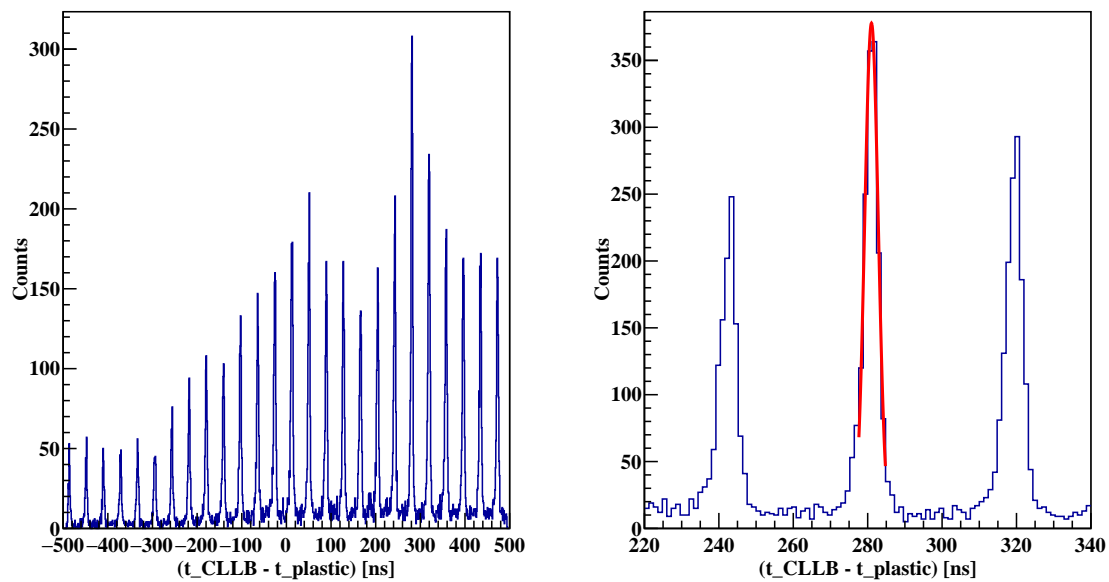


Figure. 5.8 The experimental timing spectrum (left) and that with x -axis zoomed in (right) detected in the CLLB. A coincidence window of 496 ns was used for the CLLB and plastic counter.

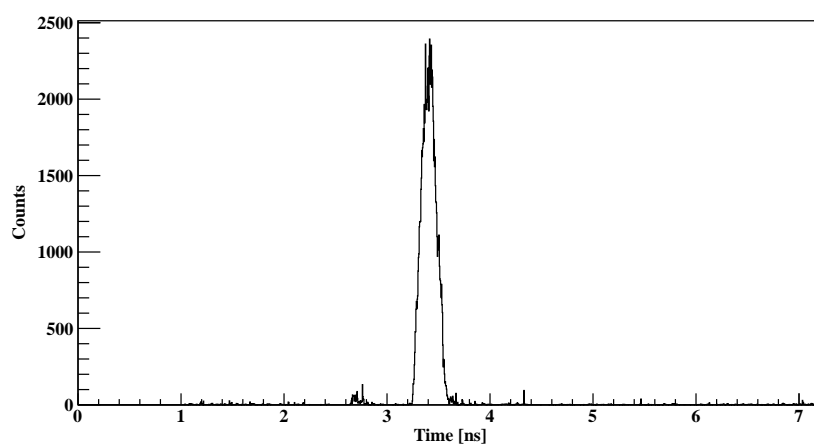


Figure. 5.9 The simulated timing spectrum scored in the CLLB.

10 times lower incident protons. In other words, the coincidence mode applied between the gamma-ray detector (CLLB) and the proton beam detector (plastic counter) rejects most of the neutron-induced noise in the energy spectra, improving the SNR for the 1D PG profile. The fall-off position for both cases locates at around 11 cm (dash line) and the statistics detected after the BP are neutron-induced background.

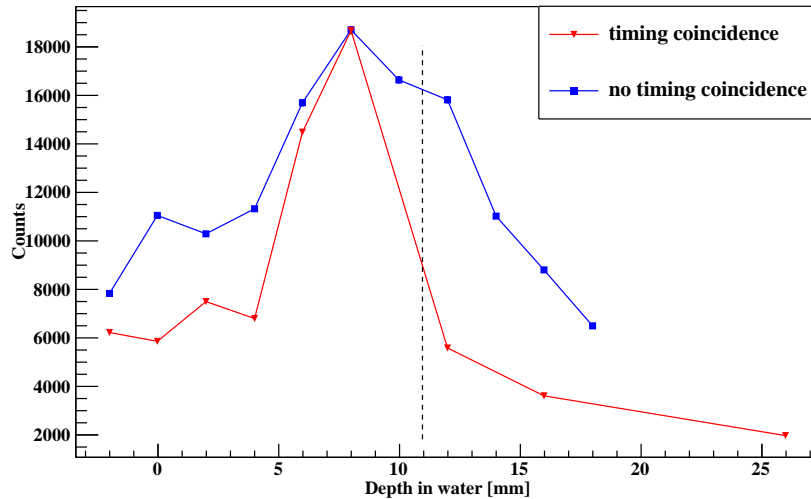


Figure. 5.10 The retrieved PG distributions along the depth in a water phantom detected in the CLLB with and without coincidence mode (PG intensity profile from coincidence mode was scaled by a factor of 15). The counts shown are selected from 3.2 to 4.5 MeV in the corresponding energy spectrum for each position. The error bar is too small to show.

5.3 PGS in the LFS array

The utilised 4 pixels in the LFS array were firstly calibrated with a ^{24}Na radioactive source: the energy spectra are shown in Fig. 5.11. The full energy peak at 2.75 MeV are the smallest, while that of the d.e. peak are the largest due to the small size of the crystal ($3 \times 3 \times 50 \text{ mm}^3$). The calibration parameters were then applied for the PGs from the water phantom and the energy spectra are presented in Fig. 5.12, where only d.e. peaks from 4.44 and 6.13 MeV were observed. It should be highlighted here that the calibration parameters obtained from the ^{24}Na source up to 2.75 MeV are not very accurate when extrapolated to the high-energy region required in the experiment (i.e. 4 - 6 MeV) due to the non-linearity of SiPMs coupled with the LFS as they become increasingly saturated for higher gamma-ray energies. The photosensor ($3 \times 3 \text{ mm}^2$, 14336 microcells) is saturated when a large number of photons are produced in the high energy range (i.e. approximately 120000 photons produced at 4 MeV).

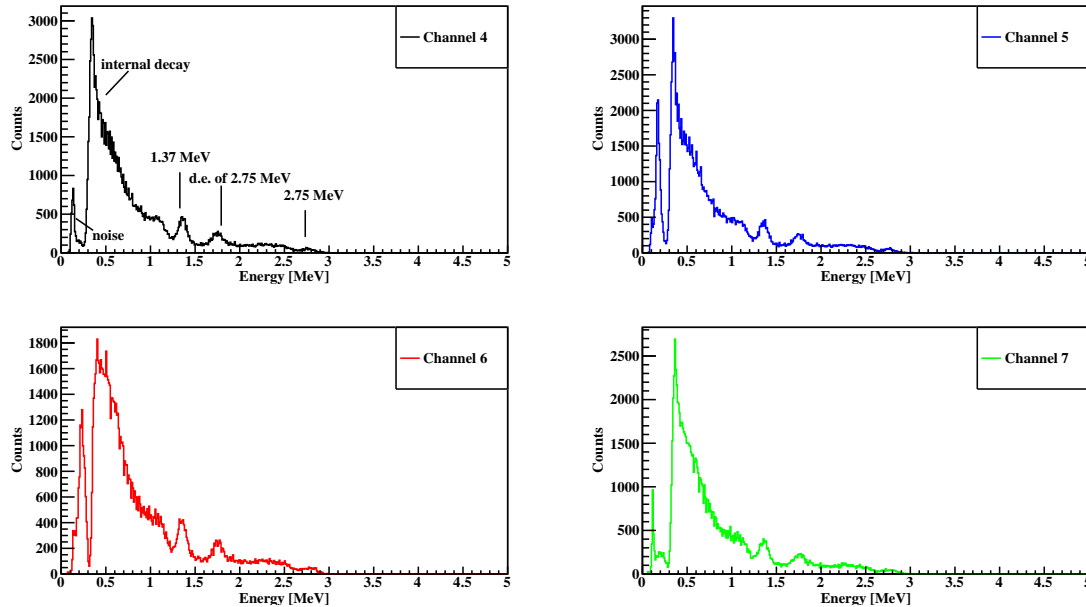


Figure. 5.11 The calibrated energy spectra from the ^{24}Na radioactive source detected in the LFS arrays. The gamma-rays from the ^{24}Na are expected at energies of 1.37 and 2.75 MeV; the peak structure at 1.73 MeV corresponds to the d.e. peak of 2.75 MeV.

The simulated energy histogram from two ‘hot’ pixels on the 5th LFS detector are displayed in Fig. 5.13 (bottom), which is consistent with corresponding experimental spectra (top) under the same proton statistics.

The simulated 2D spatial distribution (intensity profile) of the expected statistics of detected PGs from a water phantom in the LFS detectors behind the multi-slit collimator is shown in Fig. 5.14. There are around 600 events in the hot pixels on the 5th LFS detector when an energy cut of larger than 1.3 MeV was applied. The 1D PG profile is shown in Fig. 5.15 with a sigmoid function fitted to the fall-off region, giving the PG range of (14.5 ± 1.2) mm. The sigmoid fitted parameter b is (76.9 ± 1.2) mm and the phantom was aligned with the middle of the LFS detectors (pixel position at 62.4 mm), so the corrected PG range in water is 14.5 mm. The proton range estimated in the phantom is around (11.9 ± 0.3) mm (i.e. derived with the dose-depth curve scored in the phantom with $R_0 = d_{80}$). Since the range of 38 MeV beams is short and the pitch of each LFS pixel is 3.2 mm, it is still acceptable that the PG range derived from the LFS is 2.6 mm higher than the range of the beam in the phantom.

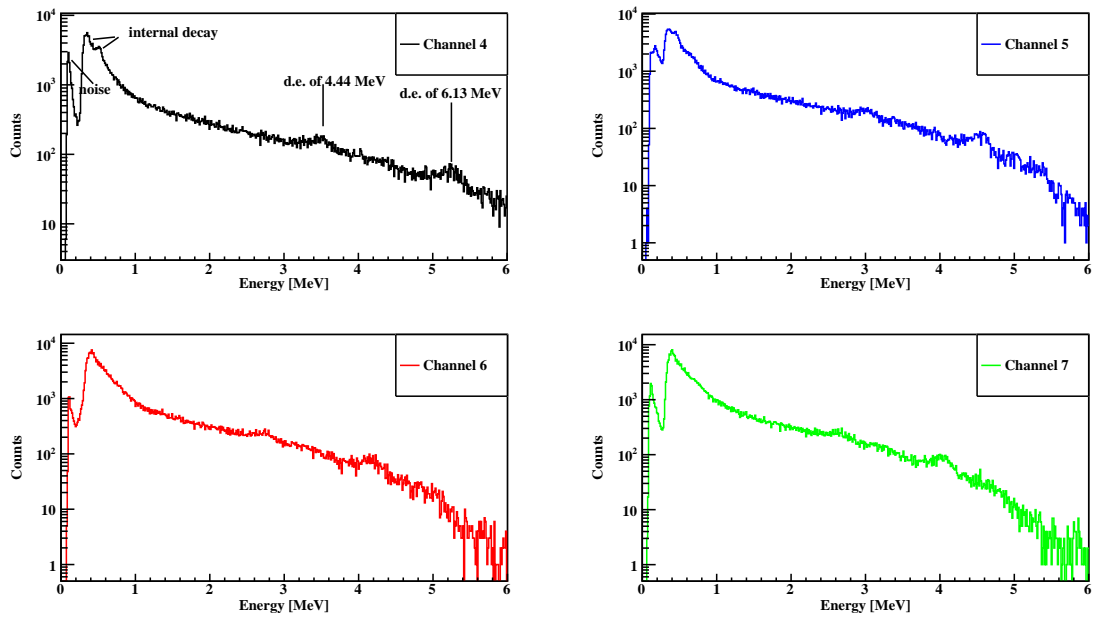


Figure 5.12 The energy spectra of secondaries detected in the LFS arrays. A total of 3×10^{11} protons were applied.

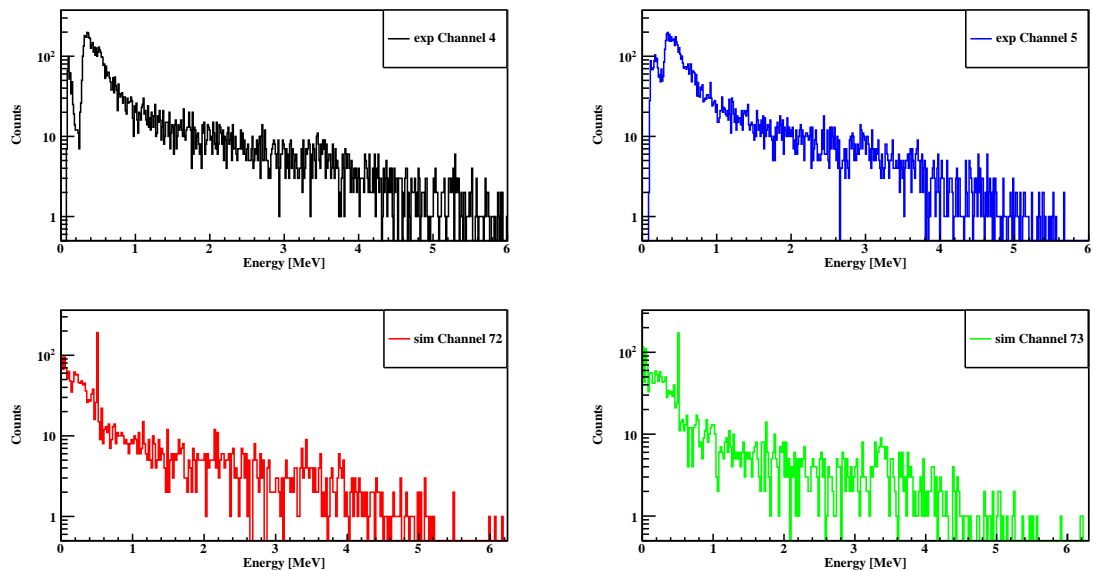


Figure 5.13 The comparison of experimental (top) and simulated (bottom) energy spectra of secondaries from a water phantom detected in the LFS arrays. A total of 10^{10} protons were applied in both cases.

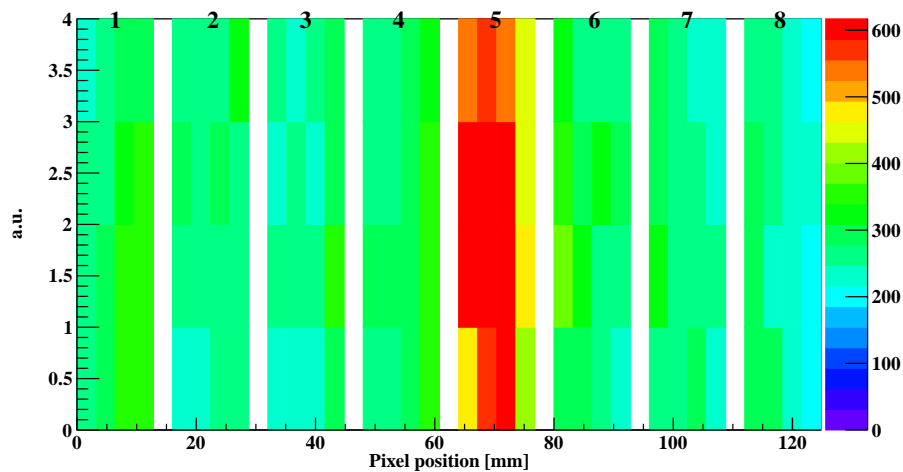


Figure. 5.14 The simulated spatial spectra of secondaries from a water phantom detected in the LFS pixels. A total of 10^{10} protons were applied in the simulation.

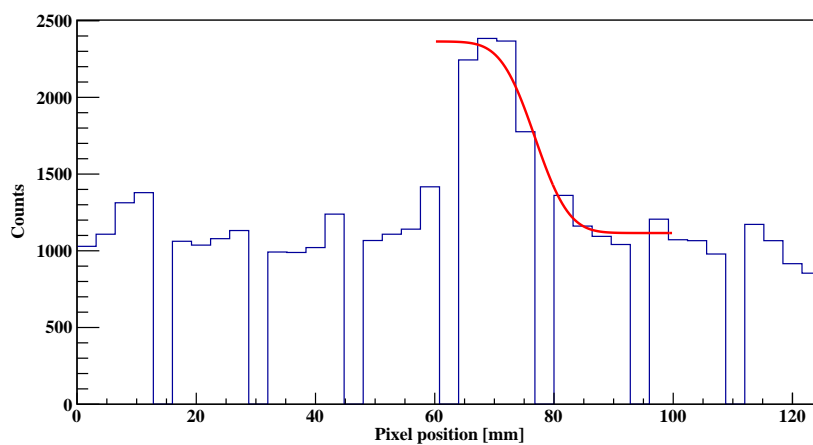


Figure. 5.15 The simulated statistics of secondaries scored in the LFS pixels along the depth in the water phantom (energy cut: higher than 1.3 MeV). The corresponding experimental results are not shown since only 4 pixels (totally 128 pixels) were extracted with the digitiser.

5.4 Fibre responses to proton beams

The fibre probe inserted in the water phantom was coupled with the plastic counter to acquire the coincidence events arriving within a timing window of 496 ns. It was kept at a fixed position and inserted in the phantom which could move along the beam direction to sample the proton energy deposition at various depths in water. Fig. 5.16 shows the comparison of experimental and simulated energy spectra measured in the fibre probe. The fibre probe was not calibrated, hence the x -axis is in channels rather than energy. Apart from the lack of absolute calibration, the shape of the spectrum is also different from that of the simulation, as the dark noise from the SiPM is high, while the true signal generated in the fibre is small.

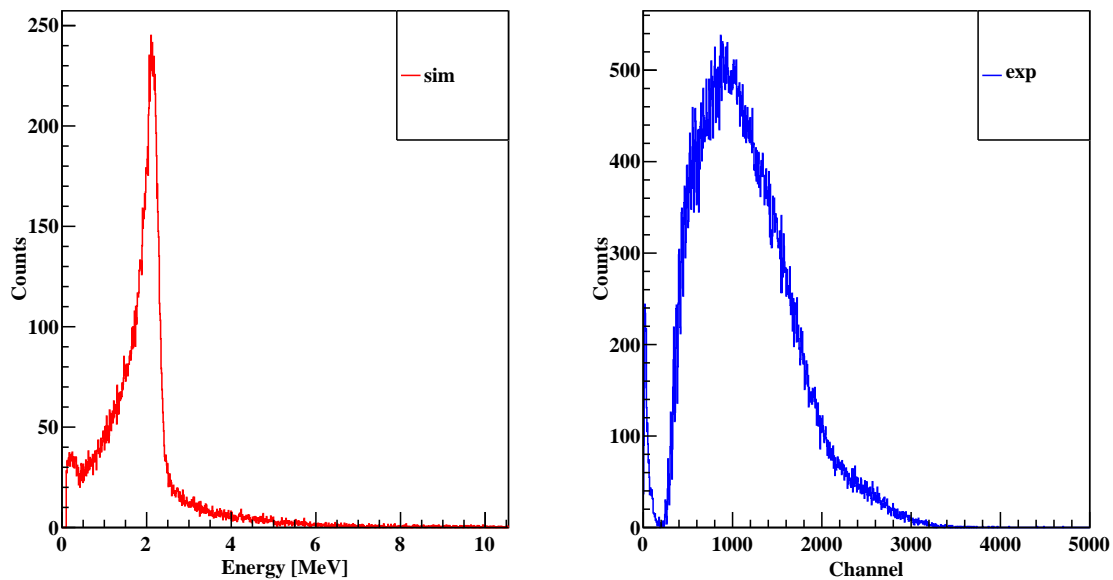


Figure. 5.16 The simulated (left) and experimental (right) energy spectra recorded in the fibre probe that was inserted at a depth of around 10.5 mm in the water phantom. A total of 3×10^9 protons were applied in both cases.

The energy-depth distributions in the fibre probe are plotted in Fig. 5.17, which shows an underestimation of measured energy deposition in the BP region, which can be attributed due to the quenching effect in the plastic scintillator. Since the fibre probe was not energy calibrated, the y -axis in the experiment curve of Fig. 5.17 does not represent the absolute normalised energy or dose. However, the range retrieved in the experiment is consistent with that calculated in the simulation, giving R_0 as (12.0 ± 0.3) mm in the experiment and (11.9 ± 0.3) mm in simulation.

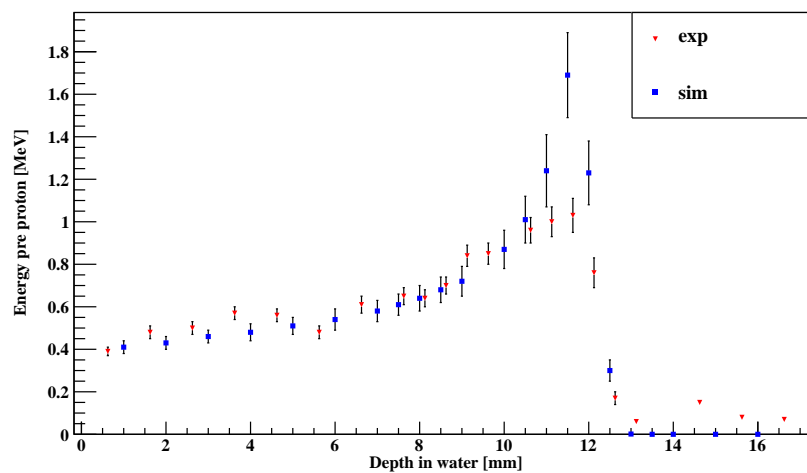


Figure. 5.17 The comparison of experimental and simulated curves of the normalised energy deposition at various depth in the water phantom.

The timing of protons were recorded in the fibre probe both in experiment and simulation. Fig. 5.18 indicates the coincidence timing differences between the fibre and the plastic counter obtained in the experiment. The coincidence timing spectrum ranges from -496 to 496 ns, and the highest peak in the middle of the spectrum represents the prompt timing peak ($\sigma \approx 1.9$ ns). The absolute proton timing shows a fairly sharp peak in Fig. 5.21 with a tail at larger times due to energy straggling ($\sigma \approx 9$ ps). It is also found that the detection system and the proton spread inside a beam bunch are the major contributions to the coincident timing resolution in the experiment.

In detail, the prompt timing peaks recorded in the fibre inserted at three different depths are shown in Fig. 5.20, where no obvious peak shift was observed due to the limitation of timing response in the experiment. The peak integral of those spectra increases with the depth, which does not agree with our expectation, i.e. the integral of timing peaks should decrease with the depth due to the beam divergence in water. The crude experimental setup for the fibre probe might explain the unexpected results (e.g. fibre might be aligned tilt regarding the iso-centre). On the other hand, the distribution of proton timing with depth in simulation is shown in Fig. 5.21. As noticed, the timing difference between the depth of 1 to 3 mm is only 1.8 ps and that between 8 to 10 mm is around 13 ps as the beam slowing down in the water. The small timing difference cannot be detected since the coincidence timing resolution between the fibre and plastic counter is around 4.5 ns (i.e. FWHM).

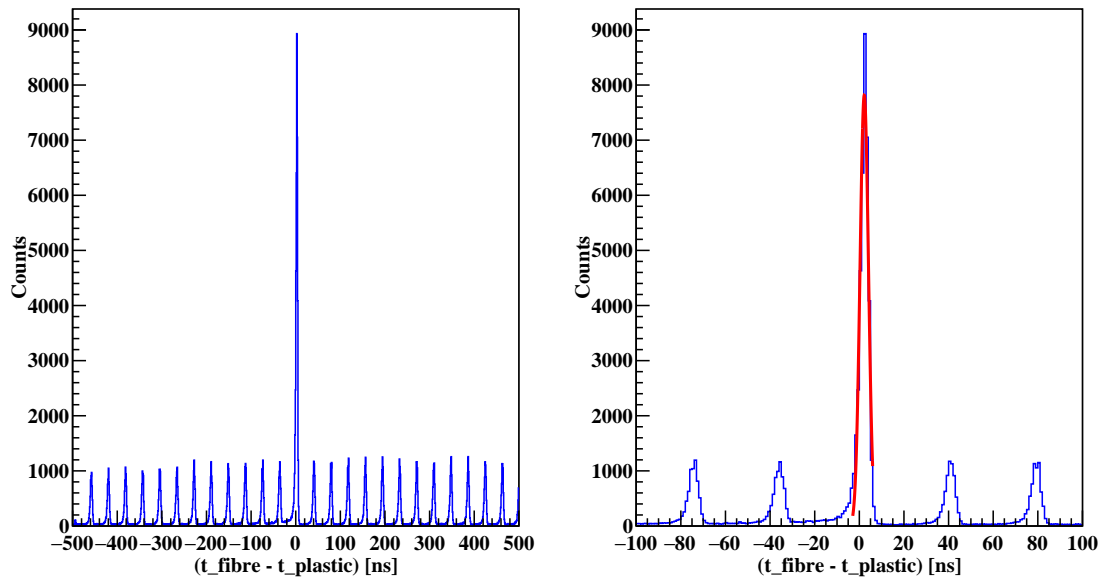


Figure. 5.18 The experimental timing spectrum (left) and that with x -axis zoomed in (right) detected in the fibre probe that was inserted at the depth of around 10.5 mm upstream of the water phantom.

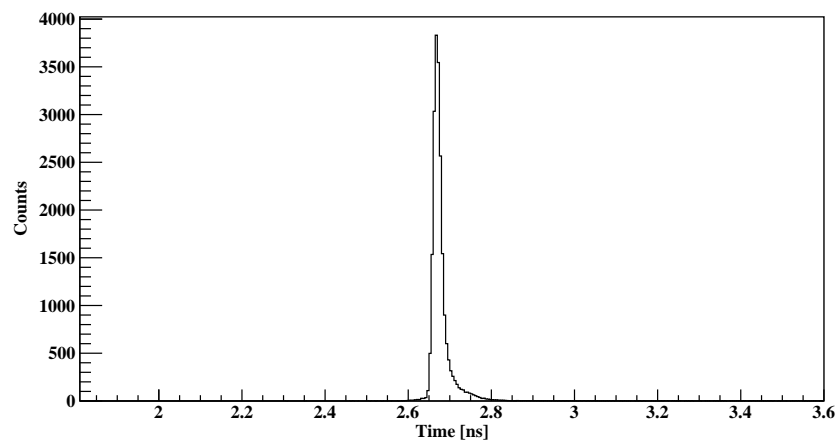


Figure. 5.19 The simulated timing spectrum scored in the fibre probe that was inserted at a depth of 10.5 mm upstream of the water phantom.

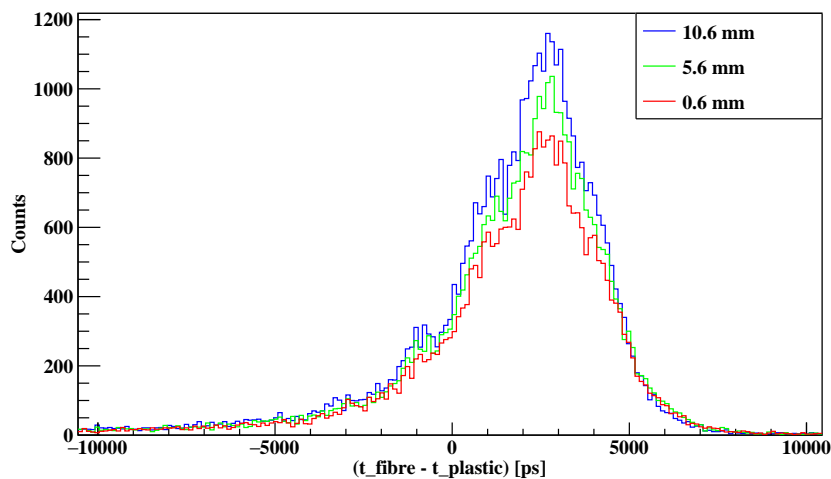


Figure. 5.20 The comparison of coincidence timing spectra recorded in the fibre probe inserted at various depth in the water phantom.

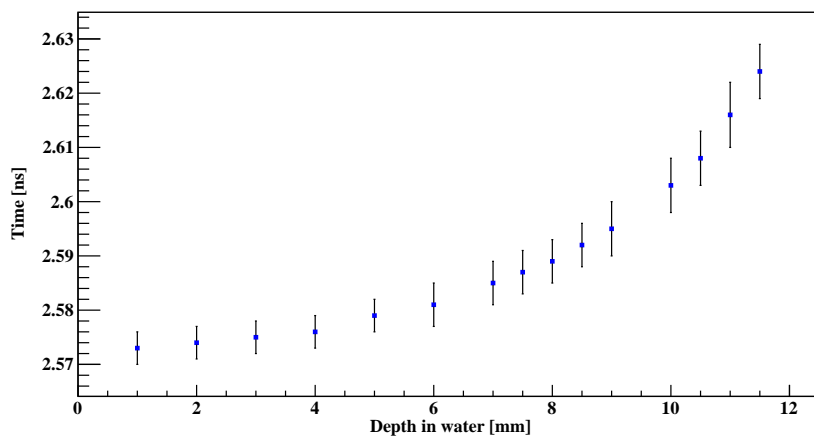


Figure. 5.21 The simulated timing of protons scored in the fibre at various depths inside the water phantom. A total of 10^5 incident protons were simulated at each depth.

5.5 Summary

We illustrated the experimental setup, methods and results for the in-beam experiment in Birmingham using proton beams at 38 MeV. Even though such low energy proton beams are not typically applied in clinical PT, it has been very suitable for testing the detector response of our detection system. The total production of nuclear-induced gamma-rays for various target media, among which water, PMMA and graphite were studied through the PG yield using a monolithic CLLB (1.5 inch). The emission of prominent gamma lines, such as 4.44 and 6.13 MeV can be used to identify the target compositions as well as the range of the protons. The timing coincidence mode applied between the CLLB (1 inch) and the plastic counter rejects most of the neutron-induced background, improving the peak-to-noise ratio by around 12 % for the d.e. peak of the 6.13 MeV gamma-ray.

The LFS arrays were firstly calibrated with gamma-rays up to 2.75 MeV produced by a ^{24}Na source, showing higher statistics for the d.e. peak than the full energy peak at 2.75 MeV due to the small size of the crystal. Similarly, only the d.e. peaks of 4.44 and 6.13 MeV were observed in the experimental energy spectra obtained in the beam. The non-linearity of the LFS crystals becomes critical when the gamma-ray energy is higher than 3 MeV, which hinders a reliable calibration of these crystals at high energies. However, the LFS detector was not chosen for its spectroscopy performance but for obtaining the 1D PG intensity profile. The PG range extracted from the simulation of the PG intensity profile is found to be about 2.2 mm higher than the actual R_0 in the phantom obtained directly from the energy deposition. This small discrepancy is, however, still acceptable given the crystal size and the short overall beam range.

The energy and timing of incident protons were recorded in the fibre probe that coupled with the plastic counter in coincidence mode. The energy histograms obtained were compared with that scored in the simulation. The range deduced in the experiment using the energy deposition in the fibre (12.0 mm) agrees very well with that calculated in the simulation (11.9 mm), even though the scaled ‘normalised energy deposition’ (i.e. not calibrated) in BP region is lower than that in the simulation due to the quenching effect. Furthermore, the simulation shows a timing difference up to 13 ps when the phantom was moved by 2 mm, while the measured coincidence timing spectra do not show the peak shift at various depths, as the timing performance of the fibre ($\sigma \approx 1.9$ ns) is not fast enough in the current setup to resolve such subtle time differences.

Chapter 6

In-beam experiment at the KVI centre

In this chapter, we discuss the experimental results from the KVI centre (Groningen, Netherlands) using a high energy proton beam up to 150 MeV. This experiment aims to explore the precision of range uncertainty in PT using different types of detector configurations. The concept is to detect the intensity profile of nuclear-induced PGs during the proton irradiation and compare it to the beam range deduced by the signals in the fibre probe. Besides the absolute range, the relative range verification was also studied via the PGS from various target media.

6.1 Methods

Proton beams of 66.5 and 150 MeV were utilised in the experiment. The beam current applied was similar to that applied in Birmingham (around 10^8 to 10^9 protons per second), and the beam was pulsed at radio-frequencies of 25 and 64 MHz depending on the beam energy. The beam spot profile has an FWHM of approximately 5 mm for the 150 MeV beam. The schematic drawing of the setup is shown in Fig. 6.1 and the corresponding photograph is displayed in Fig. 6.2.

The experiment setup is similar to that used in Birmingham, apart from the phantom configuration and the upgraded DAQ system (i.e. ASICs for multi-channel LYSO detector). Additionally, an in-house made calcium hydroxide ($\text{Ca}(\text{OH})_2$) cell that can be inserted into the water phantom was utilised to study the target heterogeneity in PT, as the cell approximates the dominant chemical composition of bone. The CLLB (1.5 inch) was used to perform PGS on different phantom configurations, covering BP locations in both the soft tissue (i.e. water) and bone (i.e. $\text{Ca}(\text{OH})_2$) equivalent regions of the phantom. The different beam energies and phantom configurations employed in the experiment are summarised in Table. 6.1.

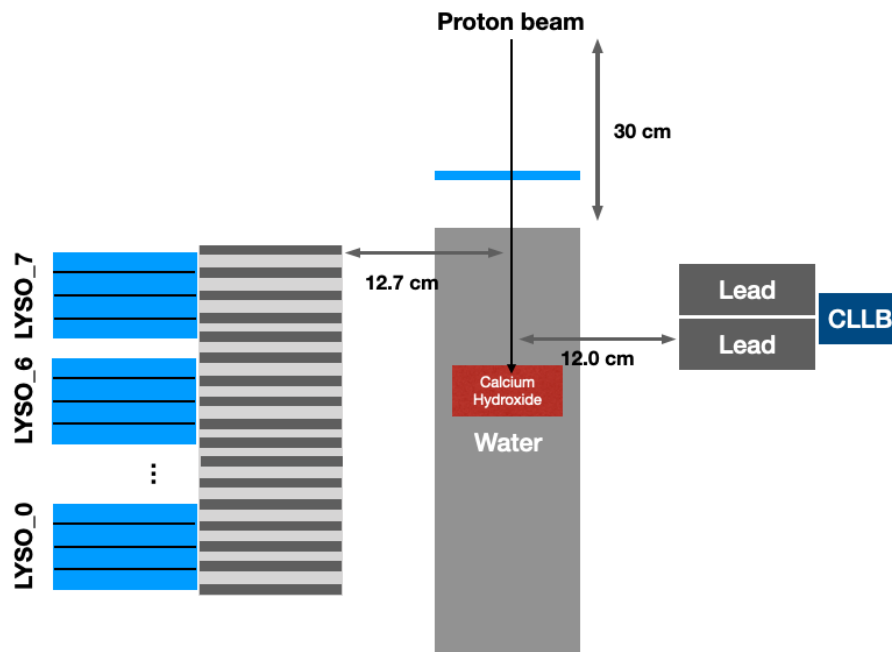


Figure. 6.1 A schematic drawing of the experimental setup at KVI (top view, not to scale). Eight LYSO detectors were placed behind the multi-slit tungsten collimator on the left side of the phantom, and the CLLB detection system was placed on the right side of the phantom. A calcium hydroxide cell was inserted inside the phantom.

Table 6.1 The different configurations of the CLLB detector position and the phantom setup used during the irradiation with the 66.5 MeV proton beam. The estimated range of a 66.5 MeV proton beam in water is around 37 mm (from NIST).

Config.	Prot. energy [MeV]	Ca(OH) ₂ position [mm]	Detector position [mm]
1	66.5	20	30 (near BP)
2	66.5	20	5 (near entrance)
3	66.5	Not inserted	30 (near BP)
4	66.5	Not inserted	5 (near entrance)

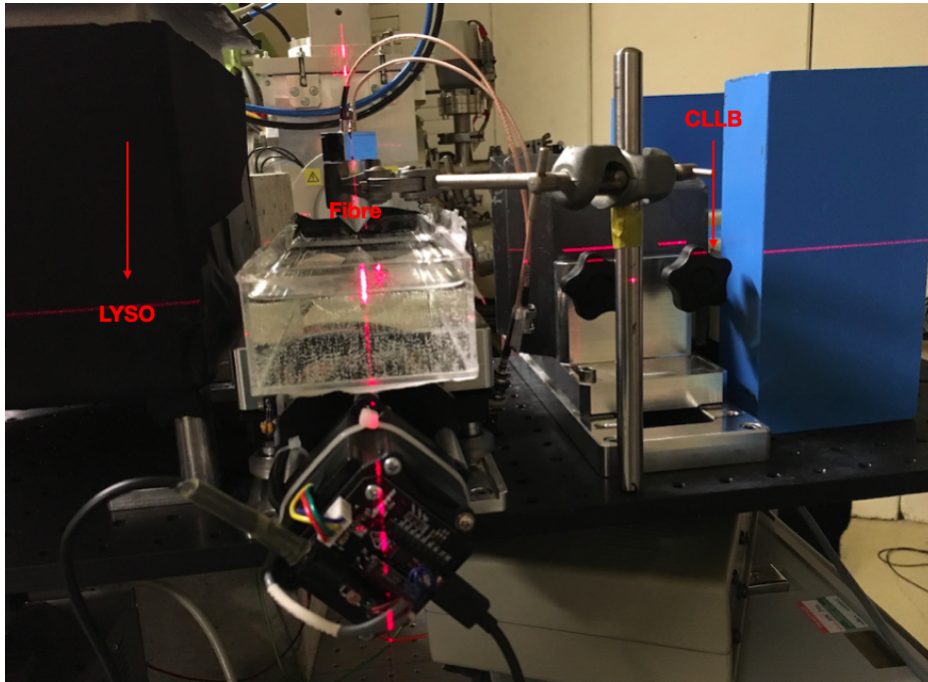


Figure. 6.2 A photograph of the experimental setup at KVI (looking upstream). On the left, there is a black box housing the LYSO arrays, ASICs and multi-slit collimator, and on the right, there is the CLLB detector behind the single-slit collimator.

The detection system consists of three types of scintillating detectors placed either on the two sides or inside the phantom for the measurements of PGs and incident protons. The detectors and their corresponding functionalities are summarised in Table. 6.2. A monolithic scintillator detector CLLB (1.5 inch) was used for the PGS, detecting the energy of the nuclear-induced particles from a water-only phantom and a Ca(OH)_2 cell inserted inside the same phantom for the study of target heterogeneity in PT. This is a simple method using a cost-effective detector for the relative range verification regarding the location of the BP in different target compositions. Furthermore, the CLLB (1 inch) and plastic counter were coupled to obtain the coincidence events from the water phantom, which gives not only the energy but also timing information of the PGs. In parallel, the absolute range is retrieved from the LYSO arrays standing behind the multi-slit collimator made by the tungsten slabs. The fibre probe and plastic counter were used for the same measurements as we did in Birmingham (i.e. energy loss and timing of incident protons).

The electronics DAQ system has been discussed in Chapter 3, section 3.2. The measured data were also compared to a Geant4 simulation: the details of the geometry defined and the physics lists used were discussed in Chapter 4, sections 4.1 and 4.4.

Table 6.2 The functionality of the different types of detector configurations that were employed in the KVI experiment.

Detector name	PGS	PGI	PGT	Proton energy loss and timing
CLLB (1.5 inch)	Y	N	N	N
CLLB (1 inch) & Plastic counter	Y	Y	N	N
LYSO arrays	N	Y	N	N
Fibre probe & Plastic counter	N	N	N	Y

6.2 PGS and PGI in the CLLB

6.2.1 PGS in CLLB (1.5 inch) with proton beams at 66.5 MeV

The experimental results that were obtained with different experimental configurations are shown in Table. 6.1 and compared with results from the Geant4 simulation. The CLLB was firstly calibrated with two radioactive sources (i.e. ^{137}Cs and ^{22}Na) and the energy resolution is around $(4.8 \pm 0.1) \%$ at 662 keV in the setup. The thermal neutrons were filtered via PSD to present the energy distribution of gamma-rays only.

Fig. 6.3 (upper) shows the measured PG spectra from regions near to the BP position. The red line shows the measured PG spectra for the case of the pure water (BP-Soft tissue), while the blue line represents spectra when the BP is within the $\text{Ca}(\text{OH})_2$ cell (BP-Bone) (i.e. corresponding to Confi. 1 and 3 respectively in Table. 6.1). For both data sets a total of 1.2×10^{11} protons irradiated the targets in 120 seconds. The main PG expected from the various isotopes present in both phantom configurations are summarised in Table. 6.3. For BP-Soft, the expected gamma-rays from the strongly populated states in ^{16}O are visible (and labelled) in the spectra together with their corresponding s.e. and d.e. peaks. These gamma-rays originate from the $^{16}\text{O}(\text{p},\text{p}')^{16}\text{O}^*$ reaction at 6.13 MeV and $^{16}\text{O}(\text{p},\text{x})^{12}\text{C}^*$ reaction at 4.44 MeV. For BP-Bone, the additional characteristic gamma-ray and escape peaks expected from the $^{40}\text{Ca}(\text{p},\text{p}')^{40}\text{Ca}^*$ reaction at 3.74 MeV are visible (also labelled in Fig. 6.3). There is, therefore, some differentiation accessible from identifying unique decay gamma-ray peaks for the ^{40}Ca .

Fig. 6.3 (lower) shows the simulated nuclear radiation spectra from the Geant4 simulation of the experimental setup. A total of 10^{10} protons have been simulated for each run of irradiating a water phantom with or without a $\text{Ca}(\text{OH})_2$ cell inserted at the BP region of the phantom. The simulation reproduces the general features of the experimental data, and it is clear that the modelling of the inelastic reactions of the protons with the ^{16}O and ^{40}Ca nuclei is reproduced by the simulation. The prominent peak at 3.74 MeV from the $\text{Ca}(\text{OH})_2$ cell is observed in the simulation predictions, together with its s.e. and d.e. peaks (labelled

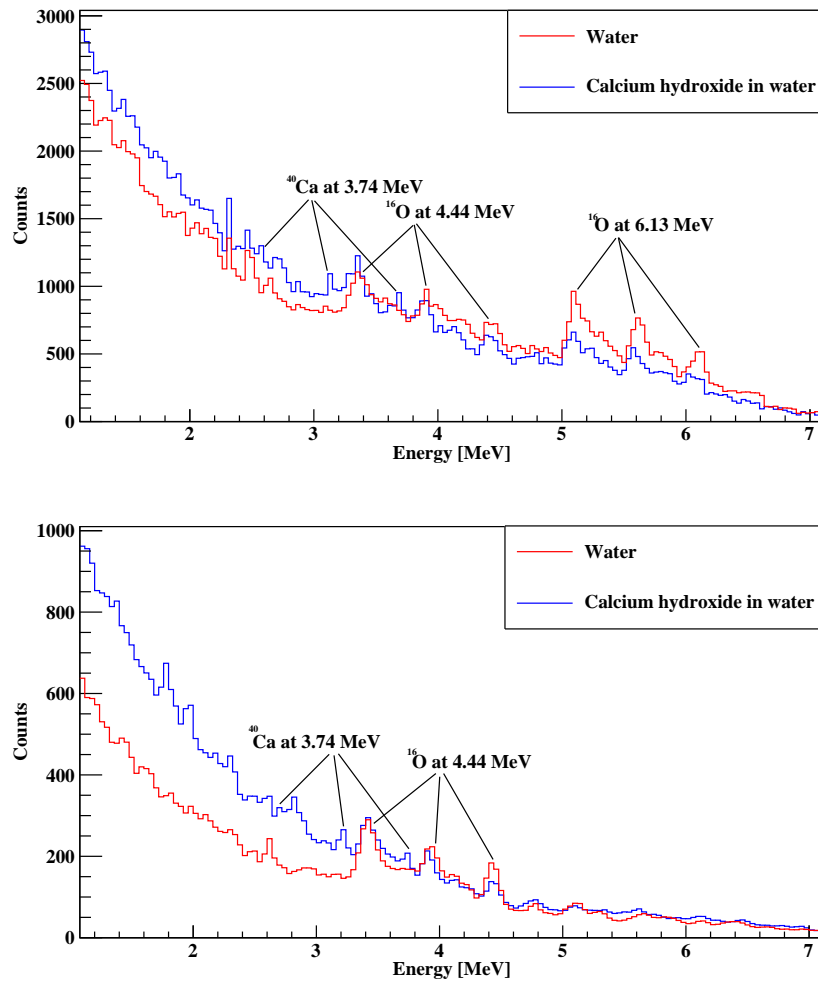


Figure. 6.3 The experimental PG transitions emitted from water and $\text{Ca}(\text{OH})_2$ when irradiated with 10^{11} protons at 66.5 MeV (upper). The simulated PG transitions emitted from water and $\text{Ca}(\text{OH})_2$ running with 10^{10} protons at 66.5 MeV (lower). The CLLB detector was placed near the BP position, corresponding to Confi. 1 and 3 listed in Table. 6.1.

Table 6.3 Nuclear reactions of interests and the corresponding prominent gamma-rays for the different isotopes in the composite phantom.

Material	Nuclear interactions	Gamma-ray energy [MeV]
Water (H ₂ O)	$^{16}\text{O}(p,x)^{12}\text{C}^*$	4.44
	$^{16}\text{O}(p,p')^{16}\text{O}^*$	6.13
Ca(OH) ₂	$^{40}\text{Ca}(p,p')^{40}\text{Ca}^*$	3.74
	$^{16}\text{O}(p,x)^{12}\text{C}^*$	4.44
	$^{16}\text{O}(p,p')^{16}\text{O}^*$	6.13

in Fig. 6.3). The main contrast is in the prediction of the contribution from the $^{16}\text{O}(p,p')\gamma$ 6.13 MeV $^{16}\text{O}^*$. This transition is exhibited clearly in the experimental data, while simulation underestimates the 6.13 MeV emission.

The simulation results show the same general features exhibited in the experiment; the PG emission at low energy below 3 MeV is enhanced when the BP is in bone rather than soft tissue. To explore this feature in more detail we present in Fig. 6.4 (left) the ratio of the PG energy spectra from a water-only phantom and when the Ca(OH)₂ cell was inserted in the same phantom. In detail, we applied the coarse division of the energy histograms (water/Ca(OH)₂) when the single-slit collimated CLLB detector was set to monitor the BP region (red points) and when it was set to monitor the entrance region of the phantom (black points).

The detected ratio at the entrance region of the phantom has been recorded as a reference data set since we do not expect any ratio fluctuation at this region for the two phantom configurations. Indeed, the ratio at the phantom-entrance region shows a stable value of around 1.0 across the entire energy region. This indicates that the gamma-ray intensity detected from both phantom configurations is the same at the entrance region, as expected since the Ca(OH)₂ cell was inserted 20 mm away from the front surface (entrance) of the phantom container and its gamma-rays should not be seen when we monitor the entrance region with the single-slit collimator.

It can be seen from the intensity ratio obtained near the BP region that at low gamma-ray energy (below 3 MeV), the ratio stays at around 0.88. Then, there is an obvious increase of the ratio between 3 to 4 MeV, reaching a value of about 1.2 at around 4.44 MeV and 1.4 in the region of 5 to 6 MeV. Since these gamma-ray spectra were obtained with high proton statistics (10^{11} , left), we also examine the sensitivity using only a subset (10 %) of the data set. We find that these features can still be identified with high statistical significance even with a 10 times lower dose, i.e. with 10^{10} protons impinging on the phantoms (see Fig. 6.4 (right)). We also note here that the solid angle coverage and detection efficiency of our detection system can be greatly improved when larger and multiple detectors surround the phantom area. The mean values of the ratio at different PGs energy regions for high and

Table 6.4 The mean values of ratio at different energy regions for PG detected near the entrance and BP position of the phantom.

Incident protons	PG energy [MeV]	Detector position	Ratio
10^{11}	0.5-3	BP	0.88 ± 0.01
	4.1-6	BP	1.25 ± 0.03
10^{10}	0.5-3	entrance	0.93 ± 0.01
	4.1-6	entrance	1.00 ± 0.02
	0.5-3	BP	0.83 ± 0.03
	4.1-6	BP	1.19 ± 0.09
	0.5-3	entrance	0.96 ± 0.04
	4.1-6	entrance	0.98 ± 0.06

low statistics were summarised in Table. 6.4. In the case of high statistics, the mean ratio of the two energy histograms at BP position is (0.88 ± 0.01) in the low energy region and (1.25 ± 0.03) in the high energy region, distinguishing from the homogeneous medium at the entrance part of the water phantom (i.e. ratio equals to around 1).

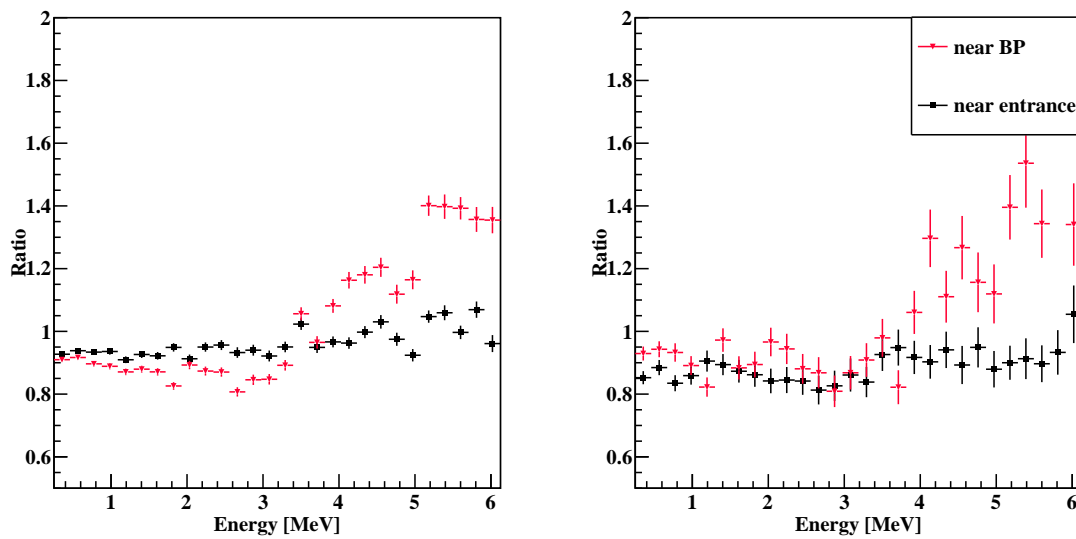


Figure. 6.4 The experimental PGs intensity ratio of two histograms (i.e. water divided by $\text{Ca}(\text{OH})_2$) presented with coarse energy binning at BP position (Confi. 1 and 3) and entrance part of the phantom (Confi. 2 and 4) when irradiated with 10^{11} (left) and 10^{10} (right) incident protons at 66.5 MeV.

Furthermore, the comparison of experimental and simulated PGs emission ratio for the water phantom divided by $\text{Ca}(\text{OH})_2$ cell in water can be seen in Fig. 6.5. The ratio at low energy region is roughly 0.62 which is lower than that from experimental data (around 0.83). The simulated ratio is also increased from 3 to 4 MeV, reaching a maximum value of

around 1.15 at around 4.5 MeV. The simulated ratio does not agree with the experimental results from 4.5 to 6 MeV due to the underestimation of the cross section for the $^{16}\text{O}(p,p'\gamma 6.13 \text{ MeV})^{16}\text{O}^*$ reaction in our simulated results. The statistics of PG lines is low (around 100 per bin) when the energy is above 5 MeV, which also adds uncertainties to the ratio at the high energy region. Overall, there is a good agreement between the experimental water/ $\text{Ca}(\text{OH})_2$ ratio curve and the prediction of the Geant4 simulation for both the BP-Soft tissue and BP-Bone scenarios.

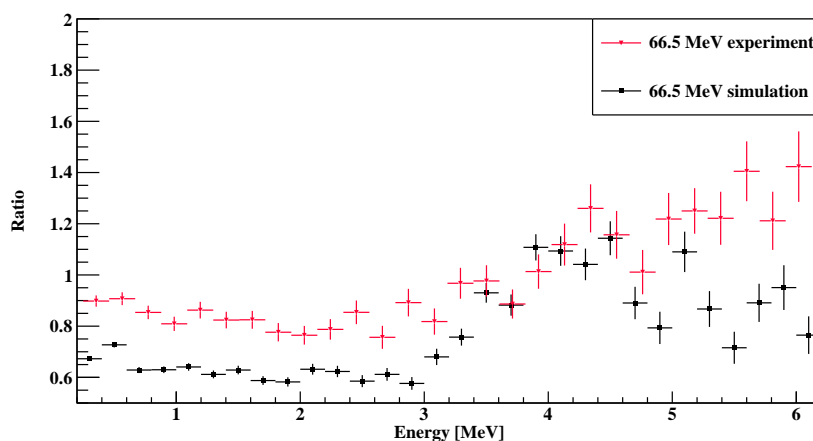


Figure. 6.5 The PGs intensity ratio of two histograms water/ $\text{Ca}(\text{OH})_2$ near BP position (Conf. 1 and 3) presented with coarse energy binning from experiment and simulation, when irradiated with proton beams at 66.5 MeV.

Based on the current findings, we suggest that this method can be used for range verification in PT in the sense that different tissues quickly result in significant coarse variations in actual energy histograms. This is feasible for the real-time beam monitoring during the treatment, stopping the proton beams automatically when the PG emission from ^{16}O at 4.44 and 6.13 MeV is lower or higher than that expected from a target tumour, indicating that the BP is located in critical organs (i.e. determining over-shoot of the proton beams when the critical organ is different from the target organ). Besides, the PGs yield at low energy region (0.5 - 3 MeV) can also be used to detect the heterogeneity of media in the phantom, giving a ratio much less than 1 when there is a dense medium in the beam line, such as bone. To qualitatively determine the dose in bone, we need to focus on the PG emission from 4 to 6 MeV generated via the nuclear interactions between ^{16}O and protons.

Table 6.5 The simulated mean values of ratio for PG detected near the BP of the phantom irradiated with 10^{10} protons for each run at 150 MeV.

Beam energy [MeV]	PG energy [MeV]	Detector position	ratio
150	0.5-3	<3.2	0.59 ± 0.02
	3.9-4.5	< 3.2	1.10 ± 0.06
	0.5-3	No	0.89 ± 0.01
	3.9-4.5	No	1.02 ± 0.04

6.2.2 PGS in CLLB (1.5 inch) with proton beams at 150 MeV

We have also simulated 150 MeV proton beams with setup illustrated in Table. 6.1. Only simulation results are presented and discussed here, since there were some technical problems during the experiment. It is interesting to note that there is substantial neutron-induced background detected with 150 MeV proton beams when there is no timing cut, causing almost 10 times higher background noise, and consequently, the peak to background ratio at prominent PG peaks is also much poorer compared with those detected with a timing cut (see Fig. 6.6 (upper)). The timing cut has been applied in the simulation to reject neutron-induced noise, as the PG signals are detected immediately after nuclear interactions, while the neutron-induced background will come later. We chose the timing cut window to be 3.2 ns based on the simulated timing spectra acquired in the detector, as illustrated in Fig. 6.6 (lower). We notice a tail after 3.2 ns, which represents the neutron-induced background when the beam energy is at 150 MeV, however, the background for beams at 66.5 MeV is fairly low. The selection of the timing window should be based on the specific detector timing resolution, beam-to-target distance and the accelerator timing structure in the experiment.

We also plotted the simulated ratio of PGs intensity versus energy for BP-Soft tissue divided by BP-Bone at 150 MeV with timing cut and without timing cut in Fig. 6.7. The simulated ratios at different PGs energy region were summarised in Table. 6.5, which excludes the high energy region from 5 to 6 MeV due to the underestimation of the cross section of $^{16}\text{O}(p,p')^{16}\text{O}^*$ in Geant4. The ratio detected with timing cut gives (0.59 ± 0.02) at the low energy region and (1.10 ± 0.06) from 3.9 to 4.5 MeV for proton beams at 150 MeV, which is compatible with the ratio (1.10 ± 0.06) detected with proton beam at 66.5 MeV (i.e. no timing cut applied at 66.5 MeV).

It can be summarised here that high energy proton beams, such as 150 MeV (i.e. commonly used in PT treatment), lead to substantial neutron-induced noise along the beam path in a phantom so that the peak-to-noise ratio for prominent gamma lines at 4.44 and 6.13 MeV is not as good as that from low energy proton beams. However, the timing selection technique provides a promising future by applying this ratio method for relative range verification in clinical energy range (75 to 250 MeV). The PG yield from specific nuclear interactions

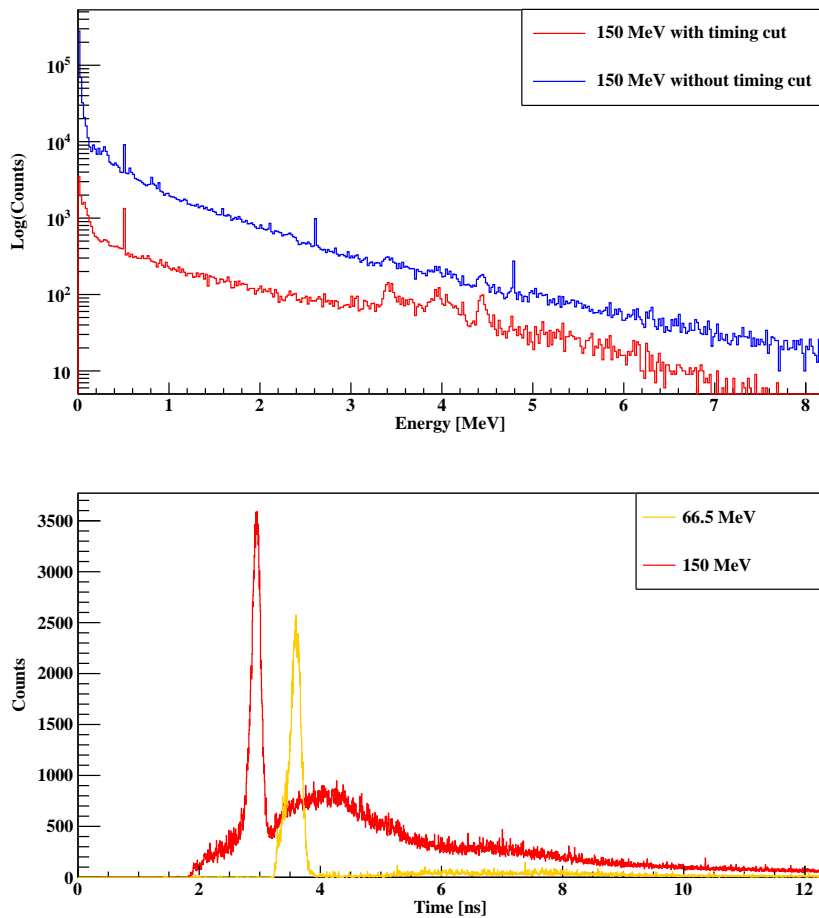


Figure. 6.6 The simulated PG energy spectra near the BP position of a water-only phantom irradiated with proton beams at 150 MeV, with and without the timing cut (< 3.2 ns) applied (upper). The simulated PG timing spectra near the BP position of a water-only phantom irradiated with proton beams at 66.5 and 150 MeV (lower).

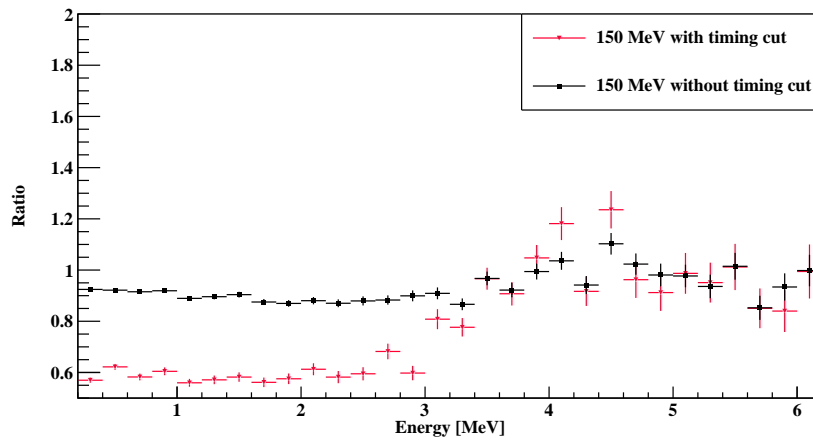


Figure. 6.7 The simulated PGs intensity ratio from two histograms water/ $\text{Ca}(\text{OH})_2$ near BP position of the phantom irradiated with proton beams at 150 MeV, when applied with and without timing cut (< 3.2 ns).

at 4.44 and 6.13 MeV can also be calibrated for the relative dose verification in clinical scenarios.

6.2.3 PGI in the CLLB (1 inch) with proton beams at 150 MeV

The 1D PG intensity profile from the water phantom was retrieved with the energy spectra recorded in the CLLB (1 inch) that was coupled with the plastic start counter in coincidence with a time window of 496 ns. A total of 21 energy spectra were collected with the single-slit collimated CLLB at a fixed position and the phantom was moving with the linear stage. The total number of protons irradiated at each position was around 3×10^9 .

The coincidence timing structure of the CLLB and plastic counter is shown in Fig. 6.8 (upper), where the prompt peak was fitted with a Gaussian function ($\sigma \approx 4.6$ ns) and the time difference between the two Gaussian peaks next to each other is around 17.6 ns (i.e. about 4 sigma separation). Fig. 6.8 (lower, blue line) gives an example of the energy spectrum measured when the corresponding depth in water was at around 147 mm (i.e. the range of 150 MeV proton beam is around 157 mm in water). Gamma-ray peaks from ^{16}O were observed even with 100 times lower proton statistics when the coincidence mode was applied. Even though the timing resolution of the CLLB detector is insufficient for PGT analysis, the background noise can be further reduced when the events gated by each of the narrow peaks are summed up, giving the comparison of energy spectra with and without gating in Fig. 6.8 (lower, red line). It is noticed that the events in the low energy region (less than 3 MeV) were reduced after the timing gating for all peaks. The neutron-induced gamma-ray background

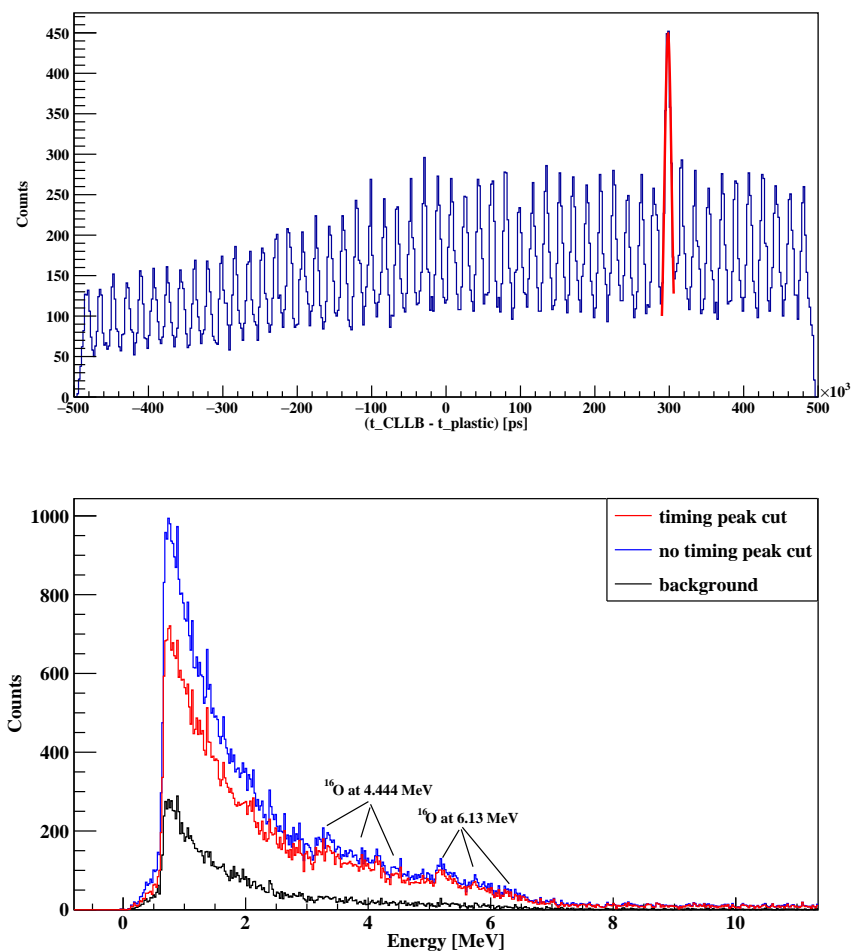


Figure. 6.8 The coincidence timing spectrum of the CLLB (1 inch) and plastic counter, which was recorded only when the two signals from both detectors arrived within the time window of 496 ns (upper). The three energy spectra measured in the CLLB (1 inch) before timing peak cut (blue), after timing peak cut (red, i.e. cut on the individual Gaussian peak in the above timing spectrum) and background of timing peak cut (black) for further background suppression (lower). A total of 3×10^9 protons were incident on the water phantom.

(plotted in Fig. 6.8 (lower, black line)) is much stronger at lower energies, and thus the energy spectrum gets reduced significantly below 3 MeV after the time gate is applied.

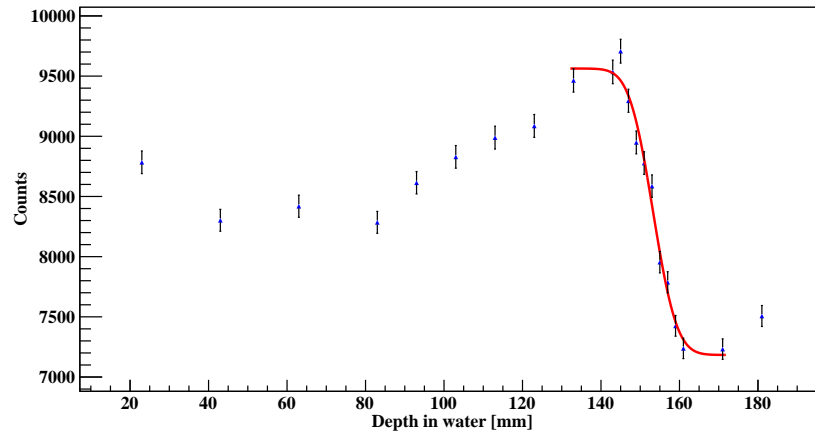


Figure. 6.9 The sigmoid fitted PG intensity profile detected in the CLLB (1 inch) along the beamline for 21 positions. The statistics were selected for an energy range of 3.2 to 6.2 MeV in the PG energy spectra for each of the position.

Finally, the retrieved PG profile from the water phantom is shown in Fig. 6.9 and a sigmoid function was applied to the fall-off region of the 1D profile. Each of the points represents the number of events in the energy spectrum within an energy selection of 3.2 to 6.2 MeV. The estimated range of the PG profile was given by the inflection point of the sigmoid function at $(152.9 \pm 0.6$ (stats error) ± 4.0 (sys error)) mm, which agrees well with the proton range calculated in the Geant4 simulation (156.3 mm).

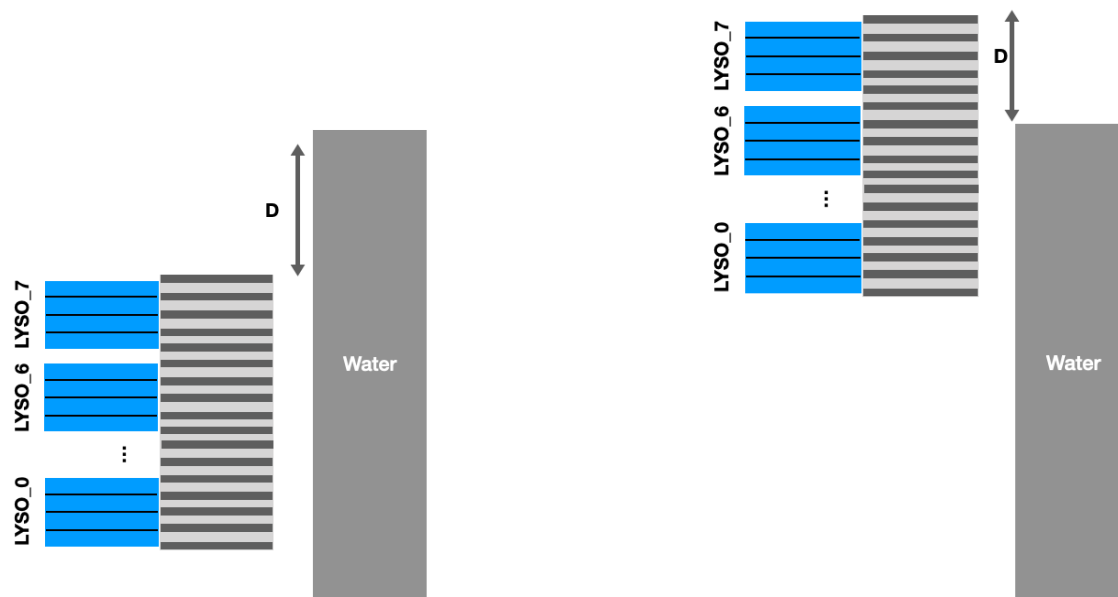


Figure. 6.10 A schematic drawing of the water phantom and LYSO detectors showing the relative position (D) of the phantom with respect to the start of the collimator with an incident proton beam energy of 150 MeV (left) and 66.5 MeV (right). The position D can be adjusted by moving the phantom on the linear stage.

6.3 The PGI in the LYSO arrays

The LYSO detector was firstly calibrated with two radioactive sources (i.e. ^{22}Na and ^{137}Cs) and the energy resolution at 662 keV is approximately 8.1 % (not corrected for non-linearity) for a single crystal in the current setup. The water phantom was moved via the linear stage during the experiment, while the detectors were placed in fixed positions. The LYSO detectors have a detecting window of around 130 mm, while the phantom has a length of around 300 mm. Thus, the distance between the phantom entrance and starting position of the detecting window (labelled in the Figs. 6.10 as D) was varied for different beam energies to cover the fall-off region of the BP in each case (i.e. range ≈ 40 mm for 66.5 MeV case and ≈ 157 mm for the 150 MeV case). During the experiment, the phantom was moved upstream to scan the BP position when the incident beam energy was 150 MeV.

6.3.1 The PGI for proton beams at 66.5 MeV

Fig. 6.11 (upper) presents the energy spectrum from two radioactive sources detected in one of the LYSO crystals. The calibrated function was then applied to obtain the PGs from a proton-irradiated water phantom measured in the same pixel, as shown in Fig. 6.11 (lower). The non-linearity of the SiPM in the LYSO crystal becomes significant in the high energy

region (> 1.3 MeV) so it is necessary to apply a high-energy gate. The 2D PG distribution regarding the pixel position on the x -axis is shown Fig. 6.12. Only events with energy higher than 1.3 MeV were selected to reject neutron-induced background and rejects the region where the internal activity is the strongest. As noticed, even though some pixels on the last

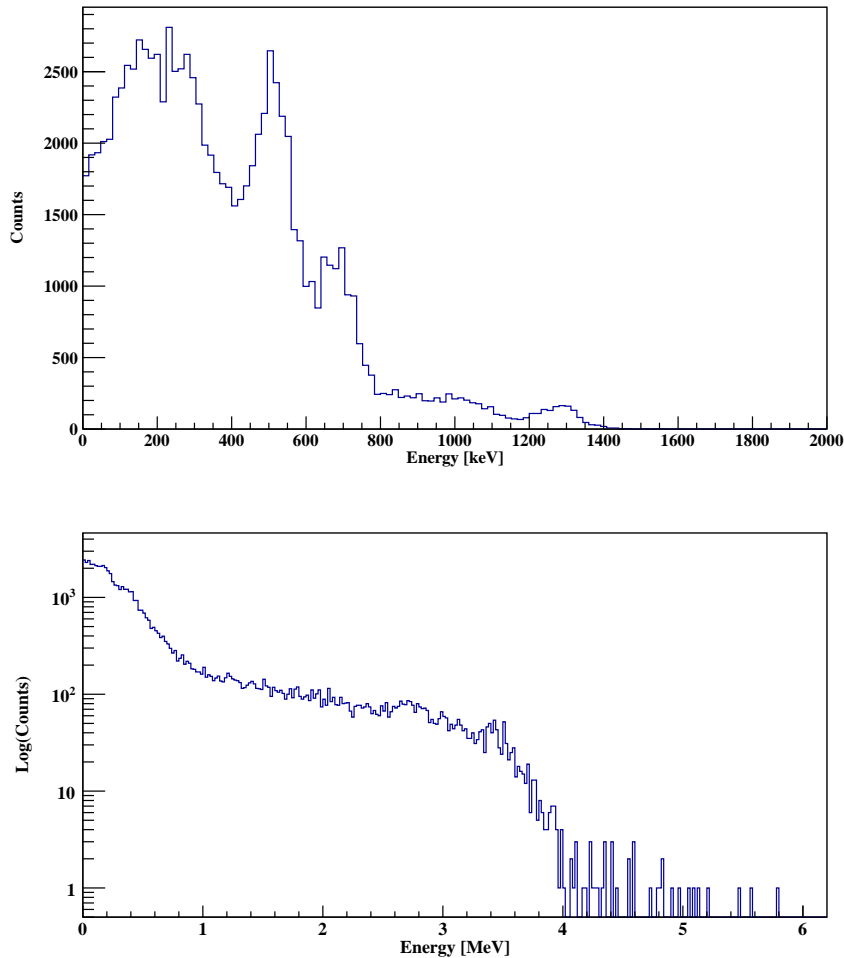


Figure. 6.11 The calibrated energy spectrum for a ^{22}Na and ^{137}Cs sources detected in one of the LYSO pixels (channel 120) (upper). The energy spectrum of PGs from the water phantom detected in the pixel (lower). A total of 3×10^{11} protons were used.

row are not displayed properly due to an electronics problem, most of the pixels (more than 90 %) were working properly during the experiment. The statistics of PGs in the 2D map were summed up for each column excluding the last row of pixels with problematic channels, retrieving the 1D PG intensity profile in Fig. 6.13. The experimental PG range in water is estimated using the sigmoid function and found to be $(33.3 \pm 2.3$ (stats error) ± 2.0 (sys

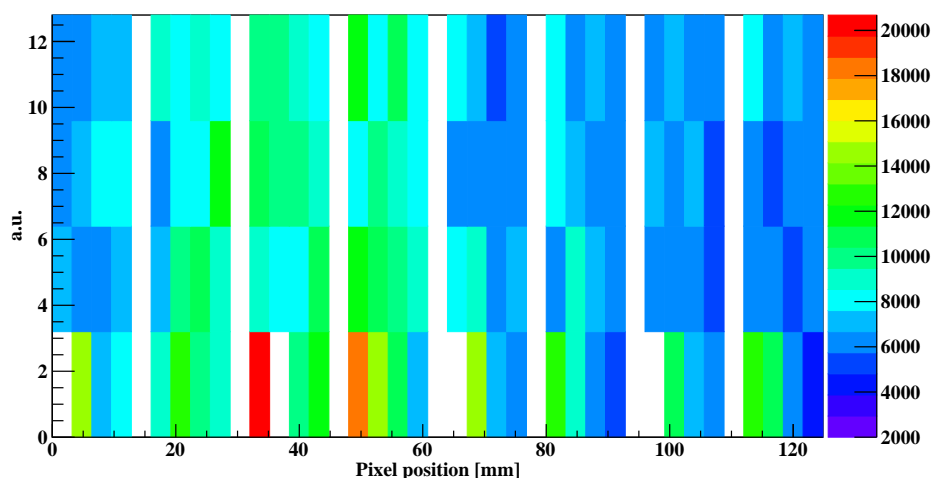


Figure. 6.12 The experimental 2D spatial distribution of PGs detected in the LYSO pixels (i.e. energy cut at 1.3 MeV). A total of 3×10^{11} protons were applied.

error)) mm¹. The estimated PG range in the experiment was around 2 mm lower than that calculated in simulation. However, the systematical error in the experimental value could be around 2 mm due to the rough setup using a laser pen. The experimental results are still acceptable considering the systematic error.

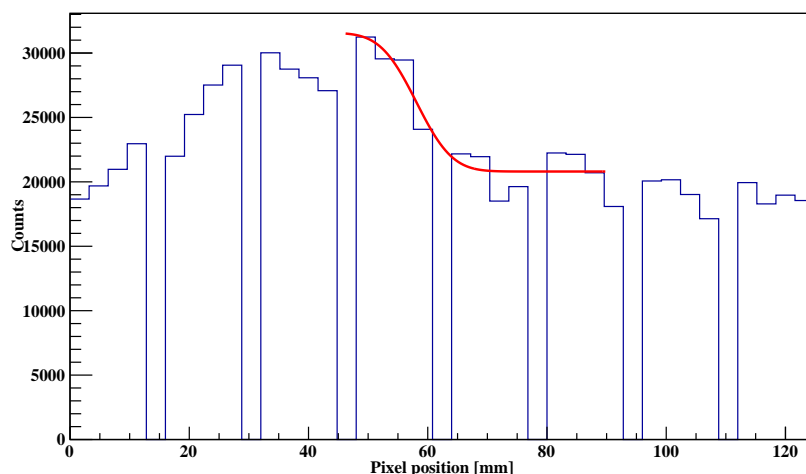


Figure. 6.13 The experimental PG intensity profile detected in the LYSO detectors along the depth in a water phantom.

¹The sigmoid fitted parameter b is (58.1 ± 2.3) mm and the phantom entrance was aligned with the LYSO detecting window at (24.8 ± 2.0) mm, so the corrected PG range is (33.3 ± 2.3) mm adding 2 mm as the systematic error.

Similarly, the simulated 2D map of secondary gamma-ray radiation and the corresponding 1D intensity profile are displayed in Figs. 6.14 and 6.15, respectively. The same analysis method was applied and the PG range is estimated to be $(35.7 \pm 0.9) \text{ mm}^2$ in reasonable agreement with the experimental results. It is noted, however, that the total proton number applied in the experiment was 30 times higher than that applied in the simulation, due to the computing time required to simulate a large number of protons (i.e. more than 12 hours for 10^{10} protons on the Viking clusters, a supercomputer).

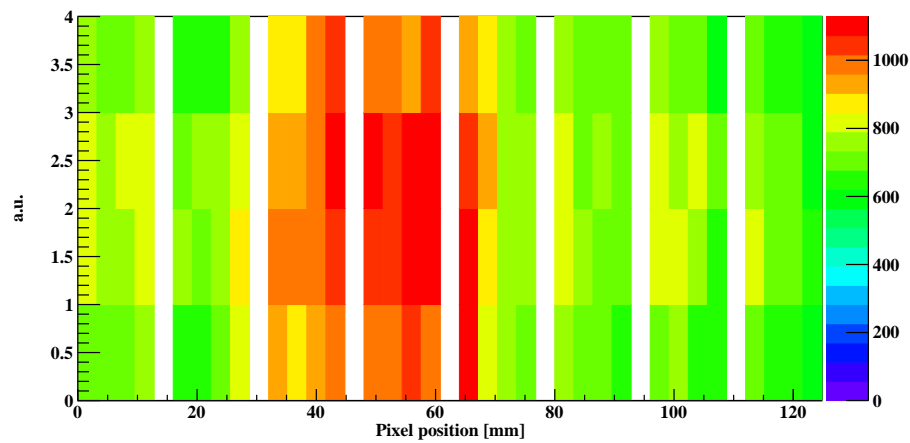


Figure. 6.14 The simulated 2D spatial distribution of PGs detected in the LYSO detectors along the depth in a water phantom with an energy selection of larger than 1.3 MeV). A total of 10^{10} protons were used.

²The sigmoid fitted parameter b is $(68.1 \pm 0.9) \text{ mm}$ and the phantom entrance was aligned with the LYSO detecting window at 32.4 mm, so the corrected PG range in water is $(35.7 \pm 0.9) \text{ mm}$.

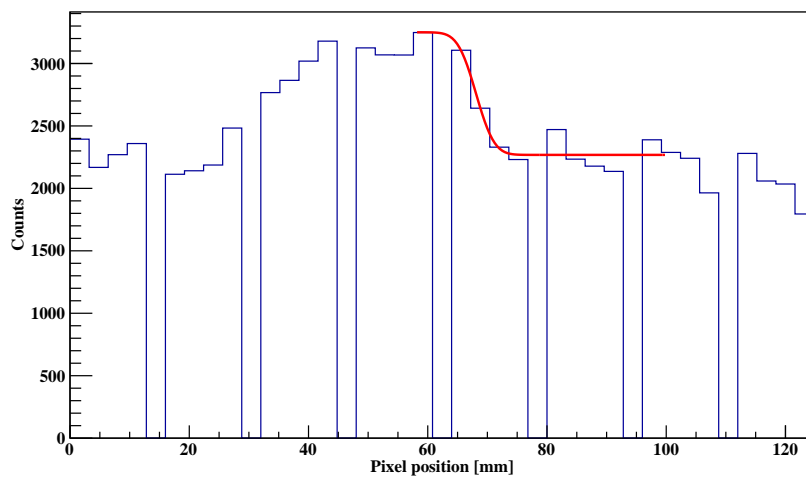


Figure. 6.15 The simulated PG intensity profile scored in the LYSO detectors along the depth in a water phantom.

6.3.2 PGI for proton beams at 150 MeV

For high energy proton beams, the background is much higher than that detected with proton beams at 66.5 MeV, as shown in Fig. 6.16. Similar to the energy spectra measured in the Birmingham experiment, only three d.e. peaks from gamma lines of interest are visible. Fig. 6.17 shows the spatial mapping of PGs along the beam direction measured in the LYSO detector for the 150 MeV proton energy case. It is hard to recognise the ‘hot’ pixels (i.e. pixels with more statistics) due to the high background noise, compared with that measured in Fig. 6.12 with low energy beams. Thus, the 1D intensity profile histogram was retrieved by the subtraction of a second data set (shown in Fig. 6.18), which was obtained when the water phantom was moved upstream by 1 cm. The 1D histogram following the subtraction of the histograms of Fig. 6.18 is shown in Fig. 6.19. In this way, the common background in the two data sets was cancelled out. The ‘hot’ pixels are clearly identified in the 6th LYSO array. A sigmoid function was then fitted to obtain the PG range at $(157.2 \pm 1.4 \pm 2)$ mm³.

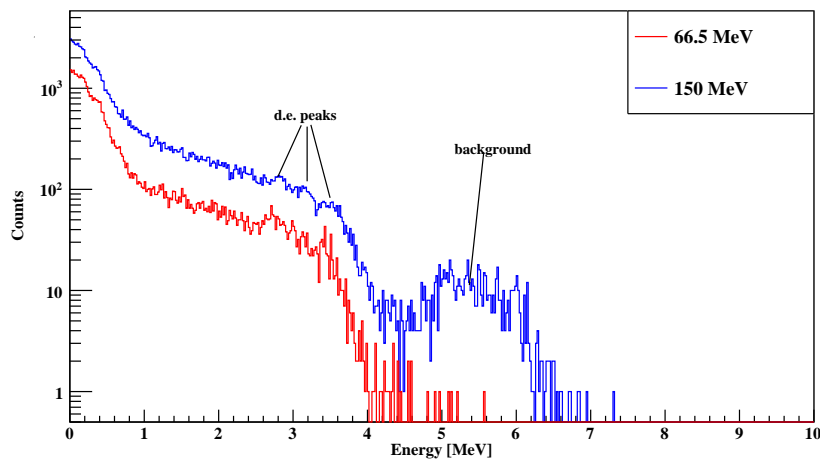


Figure. 6.16 The comparison of energy spectra measured in one of the LYSO pixels (channel 120) under different proton beam energies. The number of incident protons was around 2×10^{11} for both cases.

The simulated 2D distribution of PGs and the corresponding 1D PG intensity histogram are shown in Figs. 6.20 and 6.21, respectively. A sigmoid fitting function was applied directly for the simulated 1D histogram without any further subtraction. The PG range extracted in

³The sigmoid fitted parameter b is (88.8 ± 1.4) mm and the phantom surface was moved upstream aligning with the LYSO detecting window at 68.4 mm in run 08, so the corrected PG range is (157.2 ± 1.4) mm adding 2 mm as the systematic error during setup.

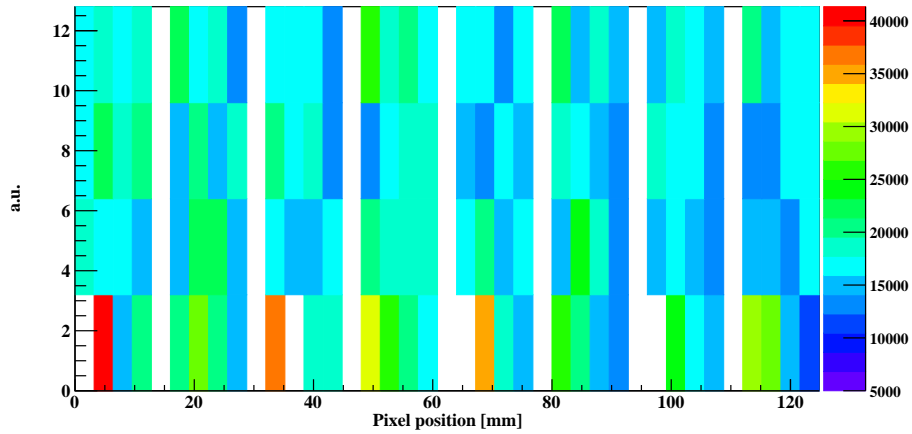


Figure. 6.17 The experimental 2D spatial distribution of PGs detected in the LYSO pixels (i.e. energy cut at 1.3 MeV). A total of 2×10^{11} protons were applied in this beam run.

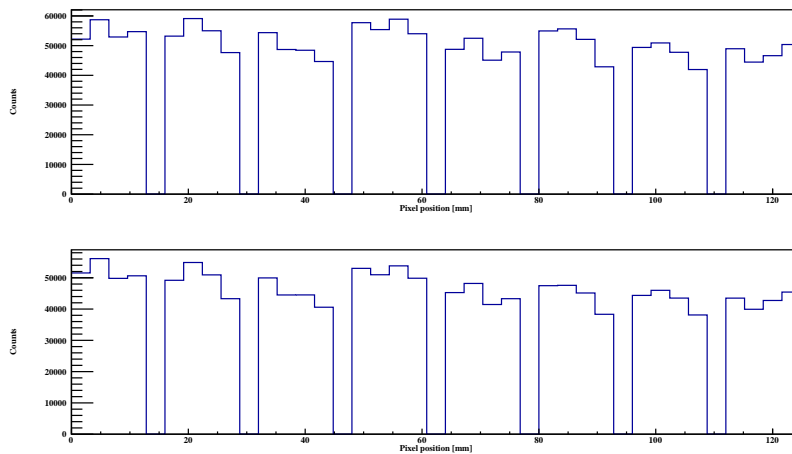


Figure. 6.18 The experimental intensity profile of PGs detected in the LYSO pixels in the first data set (upper). The experimental spatial distribution of secondaries detected in the LYSO pixels in the second data set obtained 1 cm upstream (lower).

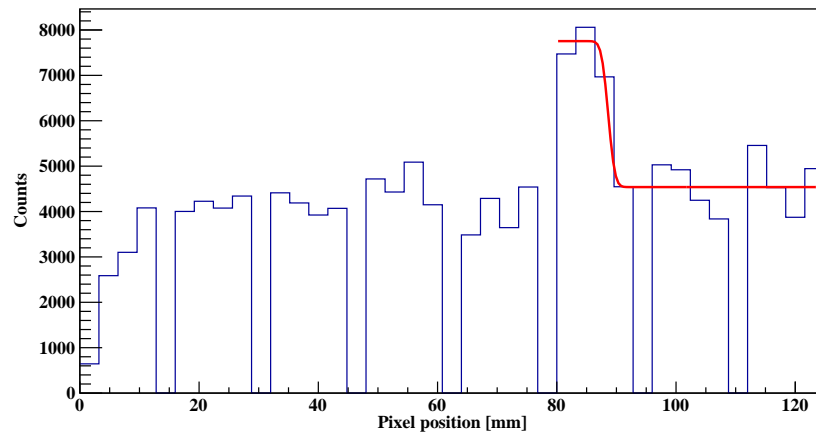


Figure. 6.19 The subtraction of the two histograms showing in Fig. 6.18 of PGs detected in the LYSO pixels along the depth of the water phantom.

simulation is $(158.1 \pm 1.7) \text{ mm}^4$. The simulated 2D spatial distribution is much clearer than that detected in the experiment since the background noise is lower and the energy resolution of LYSO pixels are perfect in the simulation.

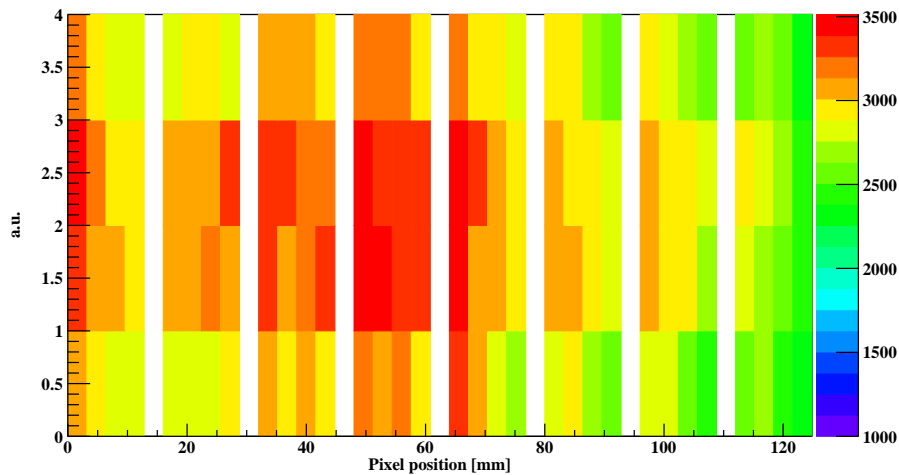


Figure. 6.20 The simulated 2D spatial distribution of secondaries detected in the LYSO arrays from a water phantom (i.e. energy cut at 1.3 MeV). A total of 10^{10} protons were applied.

⁴The sigmoid fitted parameter b is $(70.5 \pm 1.7) \text{ mm}$ and the phantom surface was moved upstream aligning with the LYSO detecting window at 87.6 mm, so the corrected PG range is $(158.1 \pm 1.7) \text{ mm}$.

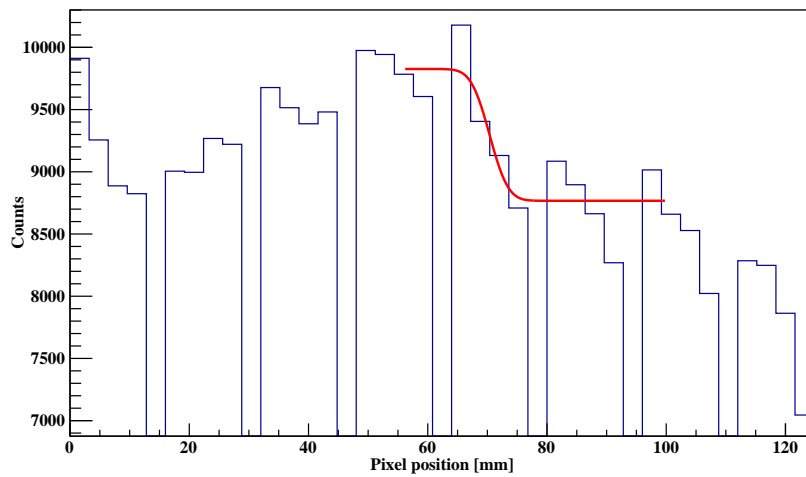


Figure. 6.21 The simulated 1D intensity profile of PGs of secondaries detected in the LYSO pixels along the depth in a water phantom.

6.4 In-beam measurements with the fibre probe

6.4.1 Fibre response for proton beam at 66.5 MeV

The fibre probe was coupled with the plastic counter in coincidence mode to record the energy and timing of protons for the two proton beam energies. The measured and simulated energy-depth curves in the fibre probe are presented in Fig. 6.22. It is noted that the measured energy curve on the entrance part of the phantom is much flatter than that in the simulation since the sensitivity of the fibre in the experiment was restricted by the detector and the electronics readout system. As discussed previously, the normalised energy deposition on

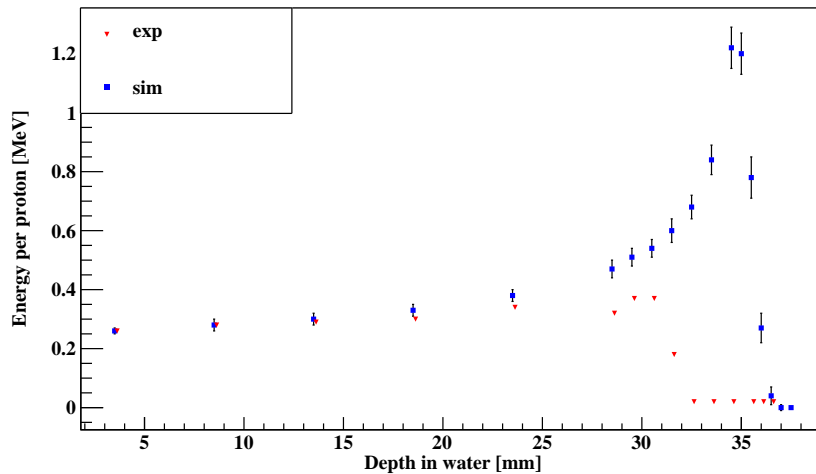


Figure. 6.22 The comparison of experimental (scaled) and simulated results of the normalised energy deposition in the fibre probe with proton beams at 66.5 MeV. The error bar in the experimental data set is too small to show. A total of 2×10^9 and 10^5 protons were used in experiment and simulation, respectively, for each position.

the y -axis does not represent the actual energy or dose. Thus, only the range on the x -axis is deduced from the curve, giving the R_0 in the experiment by $(31.0 \pm 0.5 \text{ (stats error)} \pm 4 \text{ (sys error)}) \text{ mm}^5$ and that in simulation by $(35.2 \pm 0.5) \text{ mm}$. There is a few millimetres deviation between the fall-off position determined in the experimental and the simulation, which might arise from the setup of the fibre during the measurements. The fibre was visually aligned with the iso-centre of the phantom and an inevitable systematic error was introduced by this method.

⁵ $(31.5 \pm 0.5) \text{ mm}$ was deduced from d_{80} of the curve, adding 4 mm as the systematic error during the setup. The fibre was inserted in the water phantom without any support, giving a larger systematic error than that in the Birmingham experiment (i.e. there is an open-slit lid on the top of water phantom 1 used in Birmingham).

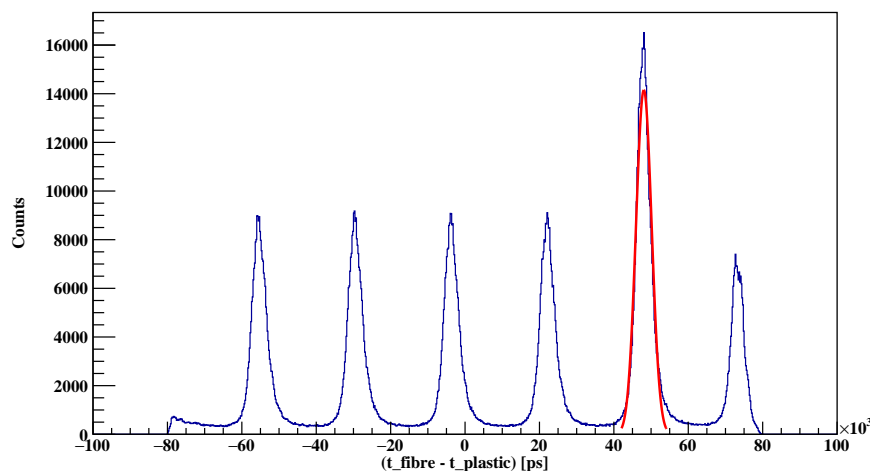


Figure. 6.23 The coincidence timing spectrum of the fibre and plastic counter, which is recorded only when the two signals from both detectors arrive within the time window of 80 ns. The fibre was placed at a depth of 21 mm inside the water phantom.

Fig. 6.23 shows the coincidence timing spectrum between the fibre and the plastic start counter of events where both signals arrived within a time window of 80 ns. A much smaller coincidence window was applied compared to the 496 ns that was applied in the previous measurements in order to reduce the total count rate accepted by the digitiser. The highest peak in Fig. 6.23 represents the real coincidence peak ($\sigma \approx 1.8$ ns), and the period of those peaks is around 25.8 ns, corresponding to the cyclotron frequency for this beam energy. Furthermore, the coincidence timing spectra from three depths are displayed in Fig. 6.24, which shows a decline of the count rate with the increase of depth due to the proton beam divergence in water. It is also noticed that the centroid of those timing spectra is shifted to the right with the increase of depth. However, the centroid of timing spectra cannot be obtained when the fibre was approaching the BP due to the significant beam broadening in the fall-off region (i.e. the statistics recorded in the BP region were too low).

The timing centroids against the depth is summarised in Table. 6.6 and the corresponding time-depth curves are presented in Fig. 6.25 for both the experimental and simulated data sets. The trend of those two curves is similar, showing an increase of the timing differences with depth as one expects due to the slowing down of protons, however, it is interesting that the timing differences between two subsequent points in simulation are significantly smaller than that observed in the corresponding experimental curve. For example, the time difference Δt is found to be around 22 ps when moving from 23.6 mm to 28.6 mm in the simulation, while it is around 509 ps in the experiment. The coincidence timing resolution (FWHM) between the fibre probe and plastic counter is around 4.2 ns in our current setup. Even though

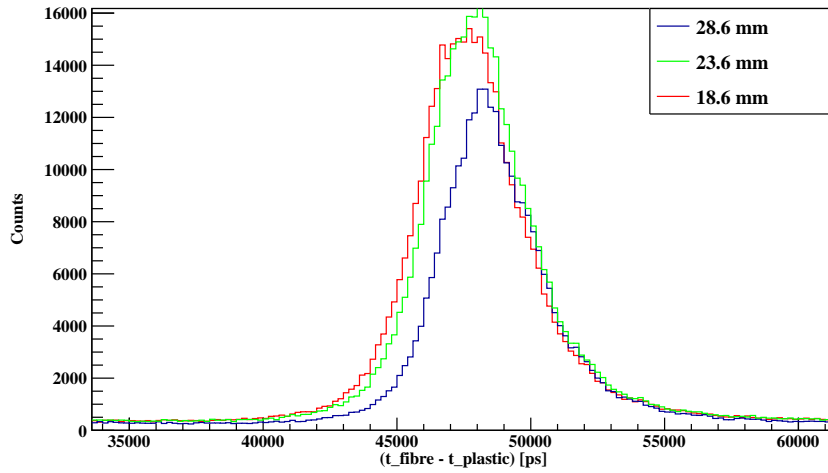


Figure. 6.24 The comparison of coincidence timing spectra at various depth in the water phantom. The centroid of the timing peak is shifted to the right side with the increase of depth in the water phantom.

Table 6.6 The centroid of the timing spectrum at various depths in the water phantom.

Depth [mm]	Timing [ps]	
	exp	sim
3.6	47138	1419
8.6	47329	1422
13.6	47500	1427
18.6	47664	1436
23.6	48035	1448
28.6	48544	1470
29.6	48715	1475
30.6	48813	1482

we are looking at centroid shifts here, this resolution is not sufficiently accurate to determine timing differences corresponding to a 5-mm phantom shift which is of the order of 10 ps. Here, we just show that it is feasible to do the relative range verification using proton timing method.

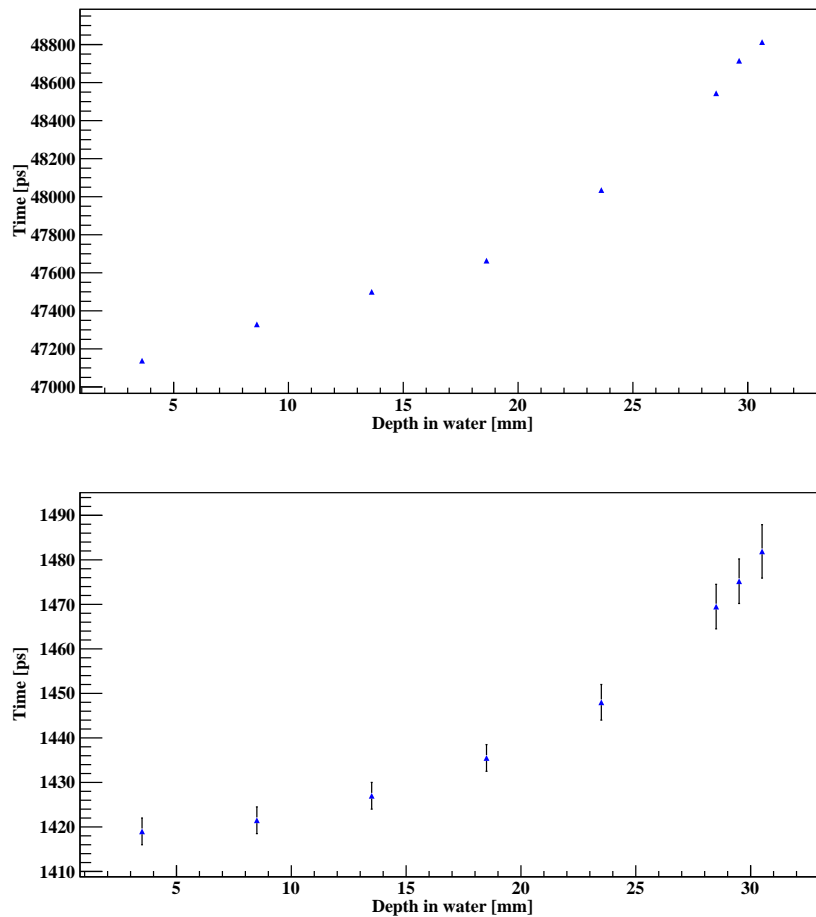


Figure. 6.25 The comparison of experimental (upper) and simulated (lower) proton timing in the fibre probe with proton beams at 66.5 MeV as a function of depth in the phantom. Both the experiment and the simulation show the same trend but the experimental points suggest a larger time difference compared to the simulation. The experimental timing curve is not as smoothing as the simulated one, since the timing resolution of the two coincidence detectors is less satisfactory.

6.4.2 Fibre response for proton beams at 150 MeV

For the measurements of the 150 MeV proton beam, we used the same fibre probe that had already been heavily used in Birmingham with 38 MeV proton beams and hence the efficiency of the probe was reduced (i.e. noise increased due to radiation damage). As discussed previously, we do not focus on the detailed energy deposition measurements but mainly on the determination of the fall-off position. The fall-off position in the experiment (155.5 ± 1.0 (stats) ± 4 (sys)) mm agrees well with the simulation (156.3 ± 0.5) mm as shown in Fig. 6.26.

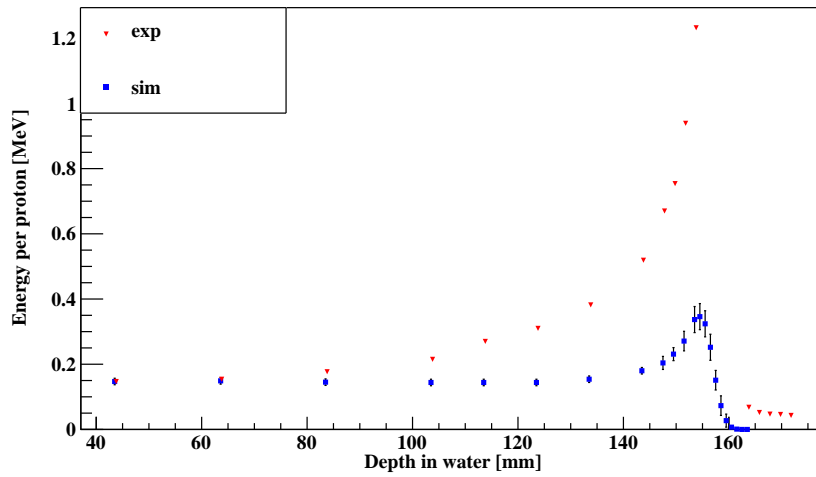


Figure. 6.26 The comparison of experimental (scaled) and simulated results of the normalised energy deposition in the fibre probe for the proton beam at 150 MeV. Good agreement is found in the location of the BP, while the absolute energy deposition comparison is less accurate due to the response of the fibre (threshold and quenching effects) and the lack of a reliable energy calibration. The error bar in the experimental data set is too small to show. A total of 4×10^9 and 10^5 protons were used in experiment and simulation, respectively, for each position.

Also, the coincidence timing spectra for signals extracted from fibre probe and plastic counter within 496 ns is displayed in Fig. 6.27. A Gaussian fitting function was applied for the prompt peak ($\sigma \cong 1.7$ ns) and the period of those timing peaks is around 18.1 ns, consistent with the cyclotron frequency for this beam energy. Similarly, the comparison of experimental and simulated timing-depth distributions in the water phantom are presented in Fig. 6.28. The error bar in the experimental data is largely due to the low statistics recorded in the coincidence timing spectrum, while the trend of the dots does agree with the simulated data. The timing difference between two subsequent positions (e.g. from 133.8 to 143.8 mm) is around 47 ps in simulation while in the experiment is around 56 ps with an error of around

20 ps, as summarised in Table. 6.7. Thus, the timing response of the protons is sensitive to determine the phantom shift in the current setup but a higher sensitivity should be reached to serve as a reliable range verification method.

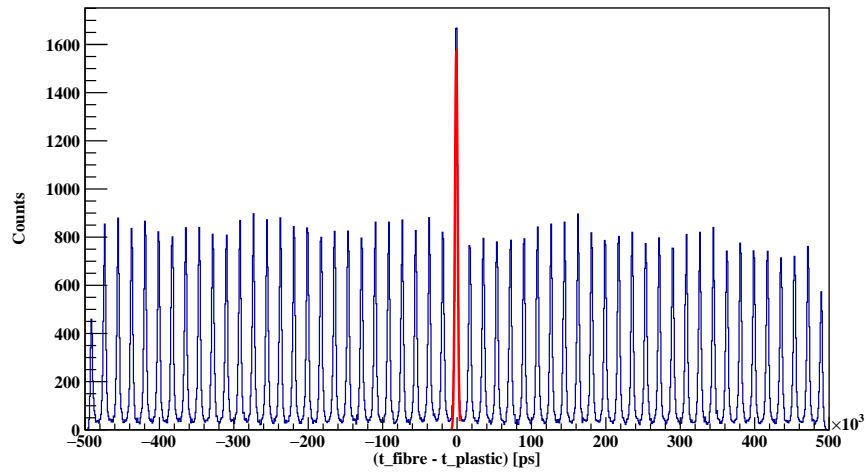


Figure. 6.27 The coincidence timing spectrum between the fibre and plastic counter recorded when signals from both detectors arriving within the time window of 496 ns.

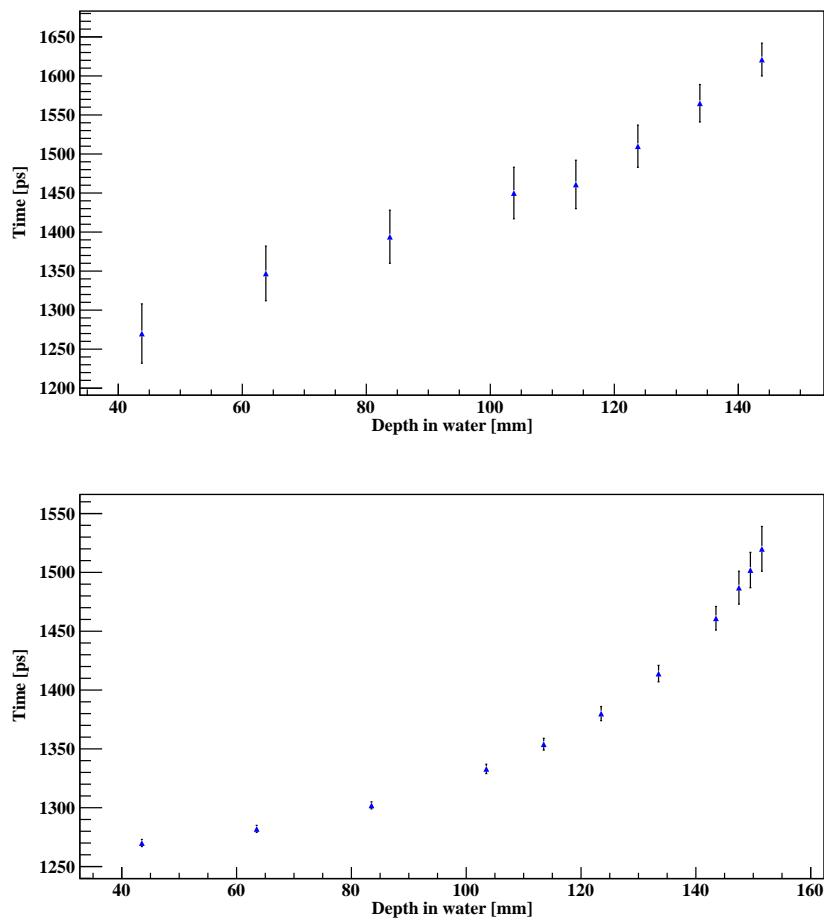


Figure. 6.28 The comparison of experimental (upper) and simulated (lower) proton timing in the fibre probe with proton beams at 150 MeV. The centroid of the time difference distribution is plotted on the y -axis versus the depth in the water phantom on the x -axis.

Table 6.7 The centroid position of the prompt-peak proton timing (150 MeV) at various depths in the water phantom as determined experimentally and by Geant4 simulation. The experimental timing values are negative since they are the coincident timing differences between two detectors, however, the simulated timing values represent the absolute time. Here, we have added an offset (2519 ps) to correct the experimental values to be comparable with the simulated ones.

Depth [mm]	Timing [ps]	
	exp	sim
43.8	1270	1270
63.8	1347	1282
83.8	1394	1302
103.8	1450	1333
113.8	1461	1354
123.8	1510	1380
133.8	1565	1414
143.8	1621	1461

6.5 Summary

Both experimental and simulated results for different types of detectors were discussed in this chapter and show a promising future for real-time beam monitoring in PT. Our current detector system allows the estimation of proton range via the PGI recorded in the LYSO detector and the relative range verification via the PGS in the monolithic CLLB detector. The PGT measured using the CLLB proves challenging due to the modest timing resolution of the detector. Moreover, a fibre probe has been utilised for the direct energy and timing measurements of incident protons, from which the absolute range was estimated and can be compared with that retrieved with PGI.

The comparison of range in a water phantom estimated via the fibre probe and LYSO detector is presented in Table. 6.8. It is noted from this table that the experimentally determined ranges suffer from a somewhat large systematic error due to experimental setup (4 mm for the fibre and 2 mm for the LYSO detectors), while it is also noted that the experimental results are in very good agreement with the simulated results for both the fibre and LYSO detectors. The ranges extracted via PGI with the LYSO detectors are also consistent with that measured directly with protons in the fibre probe, within their experimental errors. In summary, the absolute range can be retrieved by the LYSO detector reliably with statistical errors of 2.3 and 1.4 mm for beam energies at 66.5 and 150 MeV, respectively, given the total incident protons of 3×10^{11} .

On the other hand, we developed a new, complementary-method to realise relative range verification based on PGS in PT; in particular, to determine whether the BP position lies in soft tissue or bone. The high energy resolution CLLB detector was used to detect the PGS from a water-only phantom and a $\text{Ca}(\text{OH})_2$ cell inserted in the same water phantom near the BP region, showing quantitative evidence regarding the target compositions. The other key feature from the BP-Bone and BP-Soft tissue data relies on the irradiated total mass of oxygen in the media. The production of PG from ^{16}O -proton nuclear interactions at 4.44 and 6.13 MeV increases with the total irradiated mass of oxygen in the material. Moreover, in the low energy region of the PG emission (below 3 MeV), the yield increases with the density/atomic number of the medium. This method could show quickly what medium the BP resides in, and is promising for a hospital-based facility for the relative range verification between inter-fraction treatment.

As for the fibre probe, the relative range verification regarding the phantom shift can also be retrieved from the coincidence timing spectra in the phantom, which detects the phantom shift up to 5 mm for low energy proton beams and 10 mm for high energy proton beams with our current setup. A fast detector and electronics readout system are required for the quantitative range verification, while our current setup cannot meet an accurate timing

Table 6.8 Comparison of retrieved absolute range via fibre and LYSO detectors in experiment and simulation.

Energy [MeV], Range [mm]	Fibre [mm]		LYSO array [mm]	
	exp	sim	exp	sim
66.5, (35.2 ± 0.5)	31.0 ± 0.5 ± 4.0	35.2 ± 0.5	33.3 ± 2.3 ± 2.0	35.7 ± 0.9
150, (156.3 ± 0.5)	155.5 ± 1.0 ± 4.0	156.3 ± 0.5	157.2 ± 1.4 ± 2.0	158.1 ± 1.7

analysis due to the limitation of timing resolution (i.e. FWHM = 4.2 ns). Even though the absolute dose measurements using fibre still require further energy calibration, this tissue-equivalent micro-probe has the potential to be an alternative dosimeter for the Marcus chamber for the range measurements.

Chapter 7

Discussion and conclusions

PT provides localised dose peaks (i.e. BP) in the target volume, which spares doses to normal tissues compared with the conventional X-ray therapy. Specifically, the IMPT using active beam scanning techniques has been applied clinically and shown excellent dose distribution uniformity in the irregular shaped tumour volumes. It is believed more patients would benefit from the ion irradiation if the cost of PT could be reduced to be comparable with X-ray therapy. However, there are many sources of range uncertainties in clinical practice. The real-time range monitoring during the treatment is highly demanded to fully exploit the advantages of PT.

We have discussed some widely studied range verification methods via detecting beta emitters or PGs. Each of those methods has its merits and drawbacks considering the detection sensitivity and the cost-effectiveness. In this research project, a dedicated detection system was developed and tested at different proton beam energies up to 150 MeV in two different institutes, to evaluate its performance in different conditions and with different targets. The detection system consists of different types of scintillating detectors: a single-slit collimated CLLB detector for PGS, multi-slit collimated LYSO arrays for the 1D PG intensity profile, a fibre probe for measuring directly the energy deposition and timing of incident protons in a water phantom and a plastic start counter for time-of-flight measurements. This multi-modality in the detection approach, the heterogeneous phantoms, the wide range of beam energies used as well as the different laboratory environments are some of the aspects that distinguish this project. In parallel, a bespoke Geant4 simulation code was developed for this project that included all detection systems and collimator materials and the results were compared to the experimental measurements. The Geant4 simulation was also used to study and compare the different methods (PGS, PGI and PGT) assuming an ideal perfect-detector ring for gamma-ray detection.

The Geant4 simulation results confirmed that the yield of certain PGs is maximum near the BP validating the PGI as one of the most promising methods, while that of neutrons monotonically declines with the slowing down of incident beams and approaches zero before the BP is reached. The emission of some prominent gamma lines (i.e. $^{12}\text{C}(\text{p},\text{p}' \gamma 4.44 \text{ MeV})^{12}\text{C}^*$ and $^{16}\text{O}(\text{p},\text{p}' \gamma 6.13 \text{ MeV})^{16}\text{O}^*$) is particularly correlated with the range, since the cross section of those interactions peaks when protons slow down to around 20 MeV. For different target media, the yield of those prominent gamma lines is sensitive to the target composition. From the simulation results it was confirmed that it is possible to qualitatively determine the range or dose in heterogeneous targets via detecting PGS, but it is also highlighted that the neutron-induced background becomes significant as the energy of the beam increases, something that was shown to be mitigated through a time-of-flight measurement to suppress the off prompt background. Moreover, with the help of the developed simulation the PGT spectra are related to the incident beam energy and the target media, were examined as a method for the relative range verification at a low cost. From the comparative simulation study with the specific perfect-detector ring and 10^8 simulated protons of 150 MeV energy, it is found that:

- The PGI method enables the detection of a 1 mm phantom shift via applying a sigmoid function to the 1D PG profile; the range error is found to be inversely proportional to the square root of proton statistics.
- The PGS method and the suggested spectra division was used to obtain the ratio-energy distribution of the PG emission, and the mean value of ratio increases with the length of phantom shift. However, it is challenging to detect a phantom shift of less than 3 mm using this method alone.
- A Gaussian distribution was applied to the PGT spectra as the centroid was shifted with the phantom shift so that a 2 mm phantom shift was detectable.

In-beam experiments were conducted at two different institutes. Initially, the detection system was tested in the Birmingham MC40 cyclotron with low energy proton beams (38 MeV), so that the performance of the detectors regarding high energy PGs was assessed with lower neutron-induced background compared to the higher beam energies. Then, the range uncertainties and more complete characterisation of our detection system were deduced with the higher energy proton beams that were available at KVI-centre (66.5 and 150 MeV). We discuss the results and findings by different range verification methods in the following.

First of all, a monolithic CLLB detector was used in the measurements of PGS from different phantom configurations. The emission of prominent gamma lines (i.e. 4.44 and

6.13 MeV) from some interesting nuclear interactions is sensitive to various target media, depending on the target composition. It is found that the energy resolution of about 5 % at 662 keV is sufficient to perform tissue-composition sensitive measurements since we propose to use the coarse binning method which is more robust and depends less on detector resolutions. In particular, we conclude that for the ratio-energy plots even a two times worse energy resolution would still be sufficient which opens up the way for a much wider range of scintillators and with significant reduced cost. Specifically, the PG spectra from a water-only phantom and calcium hydroxide cell that inserted in the same phantom were measured, and the division of those two histograms was analysed to determine the position of BP in terms of materials.

While writing these conclusions a recent work [78] was published which reported consistent results. The authors studied the PGS for *in vivo* measurements of oxygen, carbon and calcium concentrations in the human body and they found that element contraction change of 1 % for calcium and 2 % for oxygen in various tissues were clearly identified by a monolithic CeBr3 detector. This paper suggested this technique should have an impact on the assessment of tumour hypoxia and the tracking of calcifications in brain metastases. However, the beam energies they conducted in this paper is relatively low (e.g. 90.7 MeV proton beam), so that effect of the neutron-induced background at higher energies is not obvious. In this thesis, experimental and simulation results at three different energies have nicely demonstrated how the overall background level changes as a function of beam energy. Both our experimental and Geant4 simulated results show that the neutron-induced background could hinder these measurements at higher beam energies (e.g. at 150 MeV studied in this project). Our simulation results show that up to 80 % neutron-induced background was rejected when a timing selection window was applied for a 150 MeV proton beam.

It is also found that the cross section data set of $^{16}\text{O}(p,p'\gamma 6.13\text{ MeV})^{16}\text{O}^*$ utilised in Geant4 simulation is lower than we obtained in the experiment. There is previous work at higher energies by J. M. Verburg *et al* [6] showing similar underestimation of the strength of this 6.13 MeV gamma-ray emission with Geant4. These comparisons suggest that further work is necessary for the modelling of the detailed contributing transitions produced by proton inelastic scattering.

As for the PGI method using the LYSO arrays, MC simulations and experimental results support that the specific design of the multi-slit collimator (parameters and properties) are well suited for mm accuracy measurement and the choice of the scintillating material and dimension are suited for this purpose. The total incident number of protons used in the experiment was on the order of 10^{11} . In a typical PT treatment with high beam current at 2 nA, the information would, therefore, be available within 10s of the scan starting with the present

setup. However, for a typical pencil beam spot, totally around 10^{10} protons are delivered per fraction (i.e. 2 Gy) [35]. Our simulation results also show that an acceptable range uncertainty was achieved when the data were processed with 10 times lower statistics (10^{10}), meeting the statistics requirements in the clinical scenario. For contrast-to-noise ratios, the precision is proportional to the inverse of the square root of the number of incident protons [34]. Thus, in the situation of a distal spot, typically around 10^8 protons per fraction [39], the precision would be improved by enlarging the detecting window, employing time-of-flight (ToF) technique or reducing the distance between the detectors and the phantom. J. H. Park *et al* [79] have studied a similar PGI detection system based on 36 CsI(Tl) detectors (size: $3 \times 30 \times 100 \text{ mm}^3$) and a multi-slit collimator. Their experimental results for the absolute PG range is excellent (2 - 3 mm error) for the spots which are composed 3.8×10^8 protons under high energy proton beam conditions (up to 186.3 MeV). Thus, it is possible to improve the detection efficiency of our PGI system by just enlarging the detection window to be sensitive for a realistic number of protons.

The fibre probe is also interesting as it is water-equivalent and its diameter is small enough that could be used in a laparoscopic type of real-time monitoring during irradiation. In this project, MC simulations and experimental results support that a thin scintillating fibre probe is a suitable instrument for determining the range, while for dose estimation a more quantitative analysis is required. L. Archambault *et al* [80] characterise the response of a scintillator fibre detector with proton beams by MC simulation. They have found that the quenching effect results in dose underestimation by 15 % around at the BP for beams of 150 MeV or more, which is consistent with the experimental results obtained in the Birmingham experiment. More research work is needed to characterise the energy response in the fibre detector, especially experimental database should be built for the calibration of dose measurement in PT. Moreover, in the current project the timing of the incident protons is also explored in terms of in-beam detection (time between plastic start detector and scintillating fibre). Experimental results are compared to the simulation. It is found that even though the general trend is reproduced by the simulation the absolute slowing down time of the protons in the phantom may be somewhat underestimated in the simulation. This may have implications on PGT methods based on simulations. The timing resolution of the fibre probe is also expected that it can be improved in the future for relative range verification.

In general, the experimental results agree with our expectations. First of all, it is suggested that a fast scintillating detector with adequate energy resolution can replace the HPGe detector in the measurements of PGS at a hospital-based PT institute as ratio of coarse energy regions are found to be sensitive to the tissue composition. This method is simple, efficient and low-cost for the relative range and dose verification during the treatment, which is also

feasible to monitor the heterogeneity of targets in the clinical environment. Furthermore, the PG profile measured in the LYSO detector provides a straightforward method to retrieve the absolute PG range by applying a sigmoid fitting function to the PG intensity profile. Even though the incident proton statistics are quite high to obtain the acceptable range error in this project, it is possible to improve the detector efficiency by extending the size of the detecting window. To reduce the neutron-induced background and improve the SNR, the timing and energy selection can be applied in those scintillating detectors. Last but not least, the fibre probe has the potential to be an alternative to the ion chamber for the range measurements, which is also promising to measure the exact dose in a small target volume in PT with proper energy calibration and quenching correction. Overall, It is suggested that a combination of different complementary methods and detection systems may be the best way forward to achieve reliable PG range and dose verification during PT.

Even though the readiness of the current system is far from a clinical device, it is suggested that it has reached the readiness level of serving as a complementary instrument in PT research rooms, where it can be used to correlate measurements performed in different ways and provide, for example, an absolute PG intensity profile, a good spectroscopic tool and an independent range measurement with the fibre probe. In the future, a larger detection efficiency would be beneficial for both the PGS and PGI system. The data analysis of the PGI system can be extended to add the spectrum of individual crystal to reconstruct higher energy peaks but for this, a photosensor and ADC with better linearity would be needed.

References

- [1] H. Paganetti, *Proton beam therapy*. IOP Publishing Bristol, 2017.
- [2] H.-M. Lu and H. Kooy, “Optimization of current modulation function for proton spread-out bragg peak fields,” *Medical physics*, vol. 33, no. 5, pp. 1281–1287, 2006.
- [3] B. Marchand, D. Prieels, B. Bauvir, R. S epulchre, and M. G erard, “Iba proton pencil beam scanning: an innovative solution for cancer treatment,” in *Proceedings of EPAC*, pp. 2539–2541, 2000.
- [4] W. D. Newhauser and R. Zhang, “The physics of proton therapy,” *Physics in Medicine & Biology*, vol. 60, no. 8, p. R155, 2015.
- [5] H. Paganetti, *Proton therapy physics*. CRC press, 2012.
- [6] J. M. Verburg, H. A. Shih, and J. Seco, “Simulation of prompt gamma-ray emission during proton radiotherapy,” *Physics in Medicine & Biology*, vol. 57, no. 17, p. 5459, 2012.
- [7] G. F. Knoll, *Radiation detection and measurement*. John Wiley & Sons, 2010.
- [8] “Introduction to sipm,” April 2020. [online] <https://www.sensl.com/downloads/ds/TN%20-%20Intro%20to%20SPM%20Tech.pdf>.
- [9] “Dt5730 - caen - tools for discovery,” April 2020. [online] <https://www.caen.it/products/dt5730/>.
- [10] S. Espa na, X. Zhu, J. Daartz, G. El Fakhri, T. Bortfeld, and H. Paganetti, “The reliability of proton-nuclear interaction cross-section data to predict proton-induced pet images in proton therapy,” *Physics in Medicine & Biology*, vol. 56, no. 9, p. 2687, 2011.
- [11] “Cllb scintillation material,” April 2020. [online] <https://www.crystals.saint-gobain.com/sites/imdf.crystals.com/files/documents/cllb-material-data-sheet.pdf>.
- [12] “Lyso scintillation material,” April 2020. [online] <https://www.crystals.saint-gobain.com/sites/imdf.crystals.com/files/documents/lyso-material-data-sheet.pdf>.
- [13] “Lanthanum bromide and enhanced lanthanum bromide,” April 2020. [online] <https://www.crystals.saint-gobain.com/sites/imdf.crystals.com/files/documents/lanthanum-material-data-sheet.pdf>.

- [14] “Sodium iodide scintillation material,” April 2020. [online] https://www.crystals.saint-gobain.com/sites/imdf.crystals.com/files/documents/sodium-iodide-material-data-sheet_0.pdf.
- [15] A. J. Lomax, T. Böhringer, A. Bolsi, D. Coray, F. Emert, G. Goitein, M. Jermann, S. Lin, E. Pedroni, H. Rutz, *et al.*, “Treatment planning and verification of proton therapy using spot scanning: initial experiences,” *Medical physics*, vol. 31, no. 11, pp. 3150–3157, 2004.
- [16] A. R. Smith, “Proton therapy,” *Physics in Medicine & Biology*, vol. 51, no. 13, p. R491, 2006.
- [17] E. Pedroni, T. Böhringer, A. Coray, E. Egger, M. Grossmann, S. Lin, A. Lomax, G. Goitein, W. Roser, and B. Schaffner, “Initial experience of using an active beam delivery technique at psi,” *Strahlentherapie und Onkologie*, vol. 175, no. 2, pp. 18–20, 1999.
- [18] T. Haberer, J. Debus, H. Eickhoff, O. Jäkel, D. Schulz-Ertner, and U. Weber, “The heidelberg ion therapy center,” *Radiotherapy and Oncology*, vol. 73, pp. S186–S190, 2004.
- [19] H. Paganetti, “Range uncertainties in proton therapy and the role of monte carlo simulations,” *Physics in Medicine & Biology*, vol. 57, no. 11, p. R99, 2012.
- [20] B. Arjomandy, N. Sahoo, X. Ding, and M. Gillin, “Use of a two-dimensional ionization chamber array for proton therapy beam quality assurance,” *Medical physics*, vol. 35, no. 9, pp. 3889–3894, 2008.
- [21] C.-H. Min, C. H. Kim, M.-Y. Youn, and J.-W. Kim, “Prompt gamma measurements for locating the dose falloff region in the proton therapy,” *Applied physics letters*, vol. 89, no. 18, p. 183517, 2006.
- [22] X. Zhu and G. El Fakhri, “Proton therapy verification with pet imaging,” *Theranostics*, vol. 3, no. 10, p. 731, 2013.
- [23] M. Moteabbed, S. España, and H. Paganetti, “Monte carlo patient study on the comparison of prompt gamma and pet imaging for range verification in proton therapy,” *Physics in Medicine & Biology*, vol. 56, no. 4, p. 1063, 2011.
- [24] K. Parodi, H. Paganetti, E. Cascio, J. B. Flanz, A. A. Bonab, N. M. Alpert, K. Lohmann, and T. Bortfeld, “Pet/ct imaging for treatment verification after proton therapy: a study with plastic phantoms and metallic implants,” *Medical physics*, vol. 34, no. 2, pp. 419–435, 2007.
- [25] K. Parodi, H. Paganetti, H. A. Shih, S. Michaud, J. S. Loeffler, T. F. DeLaney, N. J. Liebsch, J. E. Munzenrider, A. J. Fischman, A. Knopf, *et al.*, “Patient study of in vivo verification of beam delivery and range, using positron emission tomography and computed tomography imaging after proton therapy,” *International Journal of Radiation Oncology* Biology* Physics*, vol. 68, no. 3, pp. 920–934, 2007.

- [26] A. Knopf, K. Parodi, T. Bortfeld, H. Shih, and H. Paganetti, "Systematic analysis of biological and physical limitations of proton beam range verification with offline pet/ct scans," *Physics in Medicine & Biology*, vol. 54, no. 14, p. 4477, 2009.
- [27] C. H. Min, X. Zhu, B. A. Winey, K. Grogg, M. Testa, G. El Fakhri, T. R. Bortfeld, H. Paganetti, and H. A. Shih, "Clinical application of in-room positron emission tomography for in vivo treatment monitoring in proton radiation therapy," *International Journal of Radiation Oncology* Biology* Physics*, vol. 86, no. 1, pp. 183–189, 2013.
- [28] X. Zhu, S. España, J. Daartz, N. Liebsch, J. Ouyang, H. Paganetti, T. R. Bortfeld, and G. El Fakhri, "Monitoring proton radiation therapy with in-room pet imaging," *Physics in Medicine & Biology*, vol. 56, no. 13, p. 4041, 2011.
- [29] K. Parodi, W. Enghardt, and T. Haberer, "In-beam pet measurements of β^+ radioactivity induced by proton beams," *Physics in Medicine & Biology*, vol. 47, no. 1, p. 21, 2001.
- [30] K. Parodi, F. Ponisch, and W. Enghardt, "Experimental study on the feasibility of in-beam pet for accurate monitoring of proton therapy," *IEEE Transactions on nuclear science*, vol. 52, no. 3, pp. 778–786, 2005.
- [31] G. Sportelli, N. Belcari, N. Camarlinghi, G. Cirrone, G. Cuttone, S. Ferretti, A. Kraan, J. Ortuño, F. Romano, A. Santos, *et al.*, "First full-beam pet acquisitions in proton therapy with a modular dual-head dedicated system," *Physics in Medicine & Biology*, vol. 59, no. 1, p. 43, 2013.
- [32] S. Vecchio, F. Attanasi, N. Belcari, M. Camarda, G. P. Cirrone, G. Cuttone, F. Di Rosa, N. Lanconelli, S. Moehrs, V. Rosso, *et al.*, "A pet prototype for "in-beam" monitoring of proton therapy," *IEEE Transactions on Nuclear Science*, vol. 56, no. 1, pp. 51–56, 2009.
- [33] P. Crespo, G. Shakirin, F. Fiedler, W. Enghardt, and A. Wagner, "Direct time-of-flight for quantitative, real-time in-beam pet: a concept and feasibility study," *Physics in Medicine & Biology*, vol. 52, no. 23, p. 6795, 2007.
- [34] F. Roellinghoff, A. Benilov, D. Dauvergne, G. Dedes, N. Freud, G. Janssens, J. Krimmer, J. M. Létang, M. Pinto, D. Prieels, *et al.*, "Real-time proton beam range monitoring by means of prompt-gamma detection with a collimated camera," *Physics in Medicine & Biology*, vol. 59, no. 5, p. 1327, 2014.
- [35] I. Perali, A. Celani, L. Bombelli, C. Fiorini, F. Camera, E. Clementel, S. Henrotin, G. Janssens, D. Prieels, F. Roellinghoff, *et al.*, "Prompt gamma imaging of proton pencil beams at clinical dose rate," *Physics in Medicine & Biology*, vol. 59, no. 19, p. 5849, 2014.
- [36] M. Priegnitz, S. Helmbrecht, G. Janssens, I. Perali, J. Smeets, F. Vander Stappen, E. Sterpin, and F. Fiedler, "Measurement of prompt gamma profiles in inhomogeneous targets with a knife-edge slit camera during proton irradiation," *Physics in Medicine & Biology*, vol. 60, no. 12, p. 4849, 2015.

- [37] M. Priegnitz, S. Helmbrecht, G. Janssens, I. Perali, J. Smeets, F. Vander Stappen, E. Sterpin, and F. Fiedler, "Detection of mixed-range proton pencil beams with a prompt gamma slit camera," *Physics in Medicine & Biology*, vol. 61, no. 2, p. 855, 2016.
- [38] C. Richter, G. Pausch, S. Barczyk, M. Priegnitz, I. Keitz, J. Thiele, J. Smeets, F. Vander Stappen, L. Bombelli, C. Fiorini, *et al.*, "First clinical application of a prompt gamma based in vivo proton range verification system," *Radiotherapy and Oncology*, vol. 118, no. 2, pp. 232–237, 2016.
- [39] J. Smeets, F. Roellinghoff, D. Prieels, F. Stichelbaut, A. Benilov, C. Fiorini, R. Peloso, M. Basilavecchia, T. Frizzi, J. Dehaes, *et al.*, "Prompt gamma imaging with a slit camera for real-time range control in proton therapy," *Physics in Medicine & Biology*, vol. 57, no. 11, p. 3371, 2012.
- [40] Y. Xie, E. H. Bentefour, G. Janssens, J. Smeets, F. Vander Stappen, L. Hotoiu, L. Yin, D. Dolney, S. Avery, F. O'Grady, *et al.*, "Prompt gamma imaging for in vivo range verification of pencil beam scanning proton therapy," *International Journal of Radiation Oncology* Biology* Physics*, vol. 99, no. 1, pp. 210–218, 2017.
- [41] M.-H. Richard, M. Chevallier, D. Dauvergne, N. Freud, P. Henriquet, F. Le Foulher, J. Letang, G. Montarou, C. Ray, F. Roellinghoff, *et al.*, "Design guidelines for a double scattering compton camera for prompt- γ imaging during ion beam therapy: A monte carlo simulation study," *IEEE Transactions on Nuclear Science*, vol. 58, no. 1, pp. 87–94, 2010.
- [42] S. Peterson, D. Robertson, and J. Polf, "Optimizing a three-stage compton camera for measuring prompt gamma rays emitted during proton radiotherapy," *Physics in Medicine & Biology*, vol. 55, no. 22, p. 6841, 2010.
- [43] J. C. Polf, S. Avery, D. S. Mackin, and S. Beddar, "Imaging of prompt gamma rays emitted during delivery of clinical proton beams with a compton camera: feasibility studies for range verification," *Physics in Medicine & Biology*, vol. 60, no. 18, p. 7085, 2015.
- [44] D. Robertson, J. C. Polf, S. W. Peterson, M. T. Gillin, and S. Beddar, "Material efficiency studies for a compton camera designed to measure characteristic prompt gamma rays emitted during proton beam radiotherapy," *Physics in Medicine & Biology*, vol. 56, no. 10, p. 3047, 2011.
- [45] F. Roellinghoff, M.-H. Richard, M. Chevallier, J. Constanzo, D. Dauvergne, N. Freud, P. Henriquet, F. Le Foulher, J. Létang, G. Montarou, *et al.*, "Design of a compton camera for 3d prompt- γ imaging during ion beam therapy," *Nuclear Instruments and Methods in Physics Research Section A: Accelerators, Spectrometers, Detectors and Associated Equipment*, vol. 648, pp. S20–S23, 2011.
- [46] F. Hueso-González, F. Fiedler, C. Golnik, T. Kormoll, G. Pausch, J. Petzoldt, K. E. Römer, and W. Enghardt, "Compton camera and prompt gamma ray timing: two methods for in vivo range assessment in proton therapy," *Frontiers in oncology*, vol. 6, p. 80, 2016.

- [47] A. Koide, J. Kataoka, T. Masuda, S. Mochizuki, T. Taya, K. Sueoka, L. Tagawa, K. Fujieda, T. Maruhashi, T. Kurihara, *et al.*, “Precision imaging of 4.4 mev gamma rays using a 3-d position sensitive compton camera,” *Scientific reports*, vol. 8, no. 1, p. 8116, 2018.
- [48] C. Golnik, F. Hueso-González, A. Müller, P. Dendooven, W. Enghardt, F. Fiedler, T. Kormoll, K. Roemer, J. Petzoldt, A. Wagner, *et al.*, “Range assessment in particle therapy based on prompt γ -ray timing measurements,” *Physics in Medicine & Biology*, vol. 59, no. 18, p. 5399, 2014.
- [49] J. Petzoldt, K. Roemer, W. Enghardt, F. Fiedler, C. Golnik, F. Hueso-Gonzalez, S. Helmbrecht, T. Kormoll, H. Rohling, J. Smeets, *et al.*, “Characterization of the microbunch time structure of proton pencil beams at a clinical treatment facility,” *Physics in Medicine & Biology*, vol. 61, no. 6, p. 2432, 2016.
- [50] G. Pausch, J. Petzoldt, M. Berthel, W. Enghardt, F. Fiedler, C. Golnik, F. Hueso-González, R. Lentering, K. Römer, K. Ruhnau, *et al.*, “Scintillator-based high-throughput fast timing spectroscopy for real-time range verification in particle therapy,” *Ieee Transactions on Nuclear Science*, vol. 63, no. 2, pp. 664–672, 2016.
- [51] F. Hueso-González, W. Enghardt, F. Fiedler, C. Golnik, G. Janssens, J. Petzoldt, D. Prieels, M. Priegnitz, K. E. Römer, J. Smeets, *et al.*, “First test of the prompt gamma ray timing method with heterogeneous targets at a clinical proton therapy facility,” *Physics in Medicine & Biology*, vol. 60, no. 16, p. 6247, 2015.
- [52] J. Krimmer, G. Angellier, L. Balleyguier, D. Dauvergne, N. Freud, J. Hérault, J. M. Létang, H. Mathez, M. Pinto, E. Testa, *et al.*, “A cost-effective monitoring technique in particle therapy via uncollimated prompt gamma peak integration,” *Applied Physics Letters*, vol. 110, no. 15, p. 154102, 2017.
- [53] J. C. Polf, R. Panthi, D. S. Mackin, M. McCleskey, A. Saastamoinen, B. T. Roeder, and S. Beddar, “Measurement of characteristic prompt gamma rays emitted from oxygen and carbon in tissue-equivalent samples during proton beam irradiation,” *Physics in Medicine & Biology*, vol. 58, no. 17, p. 5821, 2013.
- [54] J. M. Verburg, K. Riley, T. Bortfeld, and J. Seco, “Energy-and time-resolved detection of prompt gamma-rays for proton range verification,” *Physics in Medicine & Biology*, vol. 58, no. 20, p. L37, 2013.
- [55] J. M. Verburg and J. Seco, “Proton range verification through prompt gamma-ray spectroscopy,” *Physics in Medicine & Biology*, vol. 59, no. 23, p. 7089, 2014.
- [56] F. H. Attix, *Introduction to radiological physics and radiation dosimetry*. John Wiley & Sons, 1986.
- [57] H. Suit, D. Phil, M. Goitein, J. Munzenrider, L. Verhey, P. Blitzer, E. Gragoudas, A. Koehler, M. Urie, R. Gentry, *et al.*, “Evaluation of the clinical applicability of proton beams in definitive fractionated radiation therapy,” *International Journal of Radiation Oncology• Biology• Physics*, vol. 8, no. 12, pp. 2199–2205, 1982.
- [58] P. Rinard, “Neutron interactions with matter,” *Passive nondestructive assay of nuclear materials*, pp. 375–377, 1991.

- [59] G. V. Santurio, M. Pinto, and C. E. Andersen, “Evaluation of the ionization quenching effect in an organic plastic scintillator using kv x-rays and a modified birks model with explicit account of secondary electrons,” *Radiation Measurements*, vol. 131, p. 106222, 2020.
- [60] S. Surti, A. Kuhn, M. E. Werner, A. E. Perkins, J. Kolthammer, and J. S. Karp, “Performance of philips gemini tf pet/ct scanner with special consideration for its time-of-flight imaging capabilities,” *Journal of Nuclear Medicine*, vol. 48, no. 3, pp. 471–480, 2007.
- [61] M. Ito, J. P. Lee, and J. S. Lee, “Timing performance study of new fast pmts with lyso for time-of-flight pet,” *IEEE Transactions on Nuclear Science*, vol. 60, no. 1, pp. 30–37, 2012.
- [62] G. Borghi, B. J. Peet, V. Tabacchini, and D. R. Schaart, “A 32 mm × 32 mm × 22 mm monolithic lyso: Ce detector with dual-sided digital photon counter readout for ultrahigh-performance tof-pet and tof-pet/mri,” *Physics in Medicine & Biology*, vol. 61, no. 13, p. 4929, 2016.
- [63] “Hamamatsu mppc (multi-pixel photon counter) arrays,” April 2020. [online] https://www.hamamatsu.com/resources/pdf/ssd/s13361-3050_series_kapd1054e.pdf.
- [64] M. Grodzicka, M. Moszyński, T. Szcześniak, A. Syntfeld-Każuch, A. Zerrouk, J. Owczarczyk, *et al.*, “Characterization of lfs-3 scintillator in comparison with lso,” *Nuclear Instruments and Methods in Physics Research Section A: Accelerators, Spectrometers, Detectors and Associated Equipment*, vol. 652, no. 1, pp. 226–230, 2011.
- [65] R. Yusoff, *Development of Radiation Counting System Based on Plastic Scintillator for Medical Applications*. PhD thesis, University of York, Department of Physics, Physics, Nuclear physics, 2019.
- [66] “Plastic scintillating fibers,” April 2020. [online] <https://www.crystals.saint-gobain.com/sites/imdf.crystals.com/files/documents/fiber-product-sheet.pdf>.
- [67] “Micro-pmt hamamatsu,” April 2020. [online] https://www.hamamatsu.com/resources/pdf/etd/MicroPMT_TPMZ1019E.pdf.
- [68] “Root a data analysis framework,” April 2020. [online] <https://root.cern.ch>.
- [69] D. Schug, V. Nadig, B. Weissler, P. Gebhardt, and V. Schulz, “Initial measurements with the petsys tofpet2 asic evaluation kit and a characterization of the asic tdc,” *IEEE Transactions on Radiation and Plasma Medical Sciences*, vol. 3, no. 4, pp. 444–453, 2018.
- [70] P. Andreo, “Monte carlo techniques in medical radiation physics,” *Physics in Medicine & Biology*, vol. 36, no. 7, p. 861, 1991.
- [71] S. Agostinelli, J. Allison, K. a. Amako, J. Apostolakis, H. Araujo, P. Arce, M. Asai, D. Axen, S. Banerjee, G. . Barrand, *et al.*, “Geant4—a simulation toolkit,” *Nuclear instruments and methods in physics research section A: Accelerators, Spectrometers, Detectors and Associated Equipment*, vol. 506, no. 3, pp. 250–303, 2003.
- [72] “Reference physics lists,” April 2020. [online] <https://geant4.web.cern.ch/node/155>.

- [73] “Em opt4,” April 2020. [online] <http://geant4-userdoc.web.cern.ch/geant4-userdoc/UsersGuides/PhysicsListGuide/html/electromagnetic/Opt4.html>.
- [74] M. Pinto, M. Bajard, S. Brons, M. Chevallier, D. Dauvergne, G. Dedes, M. De Rydt, N. Freud, J. Krimmer, C. La Tessa, *et al.*, “Absolute prompt-gamma yield measurements for ion beam therapy monitoring,” *Physics in Medicine & Biology*, vol. 60, no. 2, p. 565, 2014.
- [75] M. Zarifi, S. Guatelli, D. Bolst, B. Hutton, A. Rosenfeld, and Y. Qi, “Characterization of prompt gamma-ray emission with respect to the bragg peak for proton beam range verification: A monte carlo study,” *Physica Medica*, vol. 33, pp. 197–206, 2017.
- [76] J. Krimmer, M. Chevallier, J. Constanzo, D. Dauvergne, M. De Rydt, G. Dedes, N. Freud, P. Henriquet, C. La Tessa, J. M. Létang, *et al.*, “Collimated prompt gamma tof measurements with multi-slit multi-detector configurations,” *Journal of Instrumentation*, vol. 10, no. 01, p. P01011, 2015.
- [77] P. Henriquet, E. Testa, M. Chevallier, D. Dauvergne, G. Dedes, N. Freud, J. Krimmer, J. Létang, C. Ray, M. Richard, *et al.*, “Interaction vertex imaging (ivi) for carbon ion therapy monitoring: a feasibility study,” *Physics in Medicine & Biology*, vol. 57, no. 14, p. 4655, 2012.
- [78] P. M. Martins, R. Dal Bello, B. Ackermann, S. Brons, G. Hermann, T. Kihm, and J. Seco, “Pibs: Proton and ion beam spectroscopy for in vivo measurements of oxygen, carbon, and calcium concentrations in the human body,” *Scientific Reports*, vol. 10, no. 1, pp. 1–14, 2020.
- [79] J. H. Park, S. H. Kim, Y. Ku, C. H. Kim, H. R. Lee, J. H. Jeong, S. B. Lee, and D. H. Shin, “Multi-slit prompt-gamma camera for locating of distal dose falloff in proton therapy,” *Nuclear Engineering and Technology*, vol. 51, no. 5, pp. 1406–1416, 2019.
- [80] L. Archambault, J. C. Polf, L. Beaulieu, and S. Beddar, “Characterizing the response of miniature scintillation detectors when irradiated with proton beams,” *Physics in Medicine & Biology*, vol. 53, no. 7, p. 1865, 2008.

Appendix A

Data sheet of Scintillating materials

Table A.1 Data sheet of scintillating crystals [11–14].

Typical data	CLLB	LYSO	LaBr ₃	NaI(Tl)
Energy resolution at 662 keV [%]	4	10.9	2.6	8
Density [g/cc]	4.2	7.1	5.08	3.67
Light output [ph/MeV]	40000	29000	62700	38000
Hygroscopic	Yes	No	Yes	Yes
Wavelength of emission max [nm]	420	420	380	415
Decay time [ns]	7:180 (61 %), 1080 (39 %); n:180 (50 %), 1080 (50 %)	42	16	250

Appendix B

Functional description of electronics readout systems

B.1 Digital pile processing in DT5730

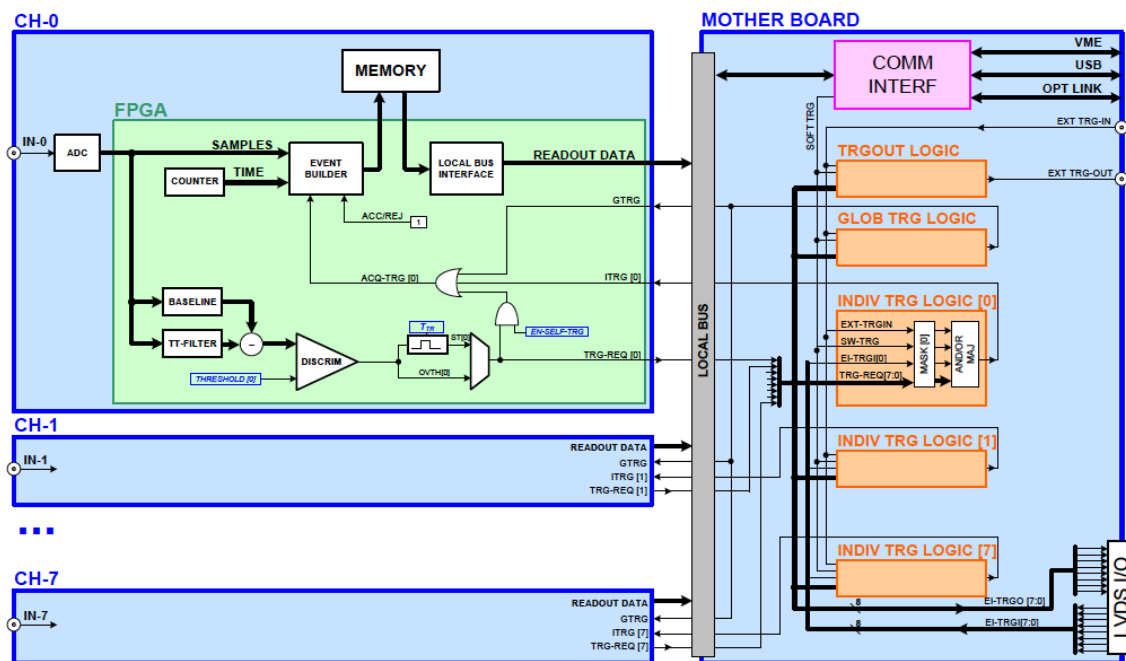


Figure. B.1 DPP firmware functional description in the normal acquisition mode.

B.2 System diagram of ASIC evaluation kit

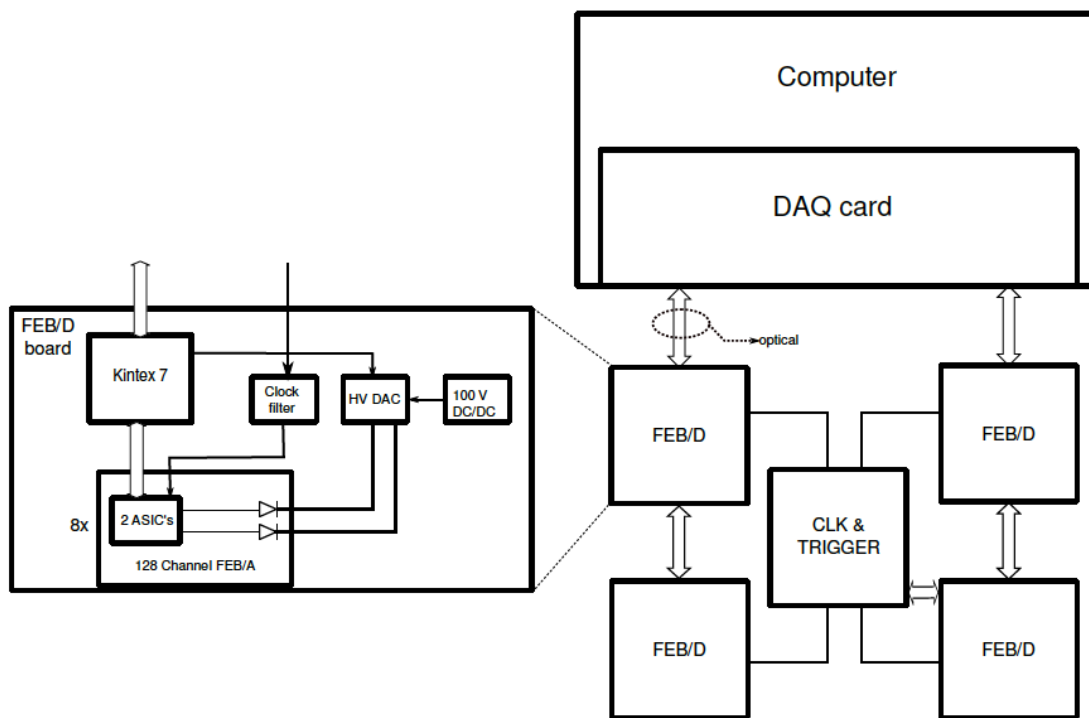


Figure. B.2 System Diagram - SiPM Readout System.

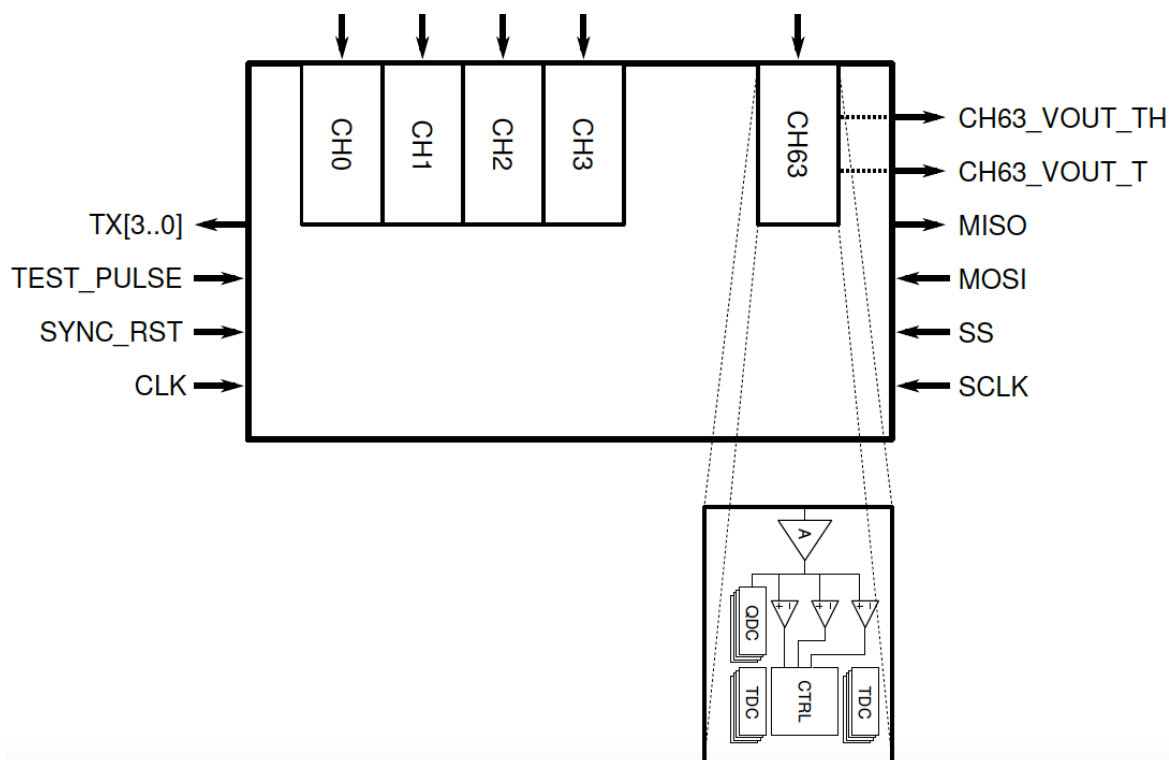


Figure. B.3 Functional block diagram of ASIC and channel.